DOTTORATO DI RICERCA IN

INGEGNERIA BIOMEDICA, ELETTRICA E DEI SISTEMI

Ciclo XXXII

Settore Concorsuale: 09/G2

Settore Scientifico Disciplinare: ING-INF/06

Inertial and magnetic sensors for upper limb kinematics:

modeling, calibration, sensor fusion and clinical applications

Presentata da: Marco Muraccini

Coordinatore Dottorato   **Supervisore**

Prof. Daniele Vigo   Prof. Angelo Cappello

                                                             Supervisore

                                                             Ing. Matteo Mantovani

Esame finale anno 2020

A me, che ce la faccio sempre, nonostante a volte abbia pensato di non farcela

A tratti il cammino è stato lungo e difficile, ma sono felice che sia andata così perché se non avessi sofferto per arrivare in fondo, la lezione non sarebbe stata così chiara

Ted Mosby

Abstract

The primary aim of the research activity presented in this PhD thesis was the development of an innovative hardware and software solution for creating a unique tool for kinematics and electromyographic analysis of the human body in an ecological setting. For this purpose, innovative algorithms have been proposed regarding different aspects of inertial and magnetic data elaboration: magnetometer calibration and magnetic field mapping (Chapter 2), data calibration (Chapter 3) and sensor-fusion algorithm. Topics that may conflict with the confidentiality agreement between University of Bologna and NCS Lab will not be covered in this thesis.

After developing and testing the wireless platform, research activities were focused on its clinical validation. The first clinical study aimed to evaluate the intra and interobserver reproducibility in order to evaluate three-dimensional humero-scapulo-thoracic kinematics in an outpatient setting (Chapter 4). A second study aimed to evaluate the effect of Latissimus Dorsi Tendon Transfer on shoulder kinematics and Latissimus Dorsi activation in humerus intra - extra rotations (Chapter 5). Results from both clinical studies have demonstrated the ability of the developed platform to enter into daily clinical practice, providing useful information for patients' rehabilitation.

Summary:

Introduction:

Human movement is a complex phenomenon and the ability to assess the quality or quantity of movement has the potential to provide an invaluable source of knowledge to clinicians to accurately diagnose and treat a variety of medical conditions [1, 2, 3]. In the large area of motion analysis, an important part is covered by kinematics, intended as the study of motion without regard to causes [3]. Kinematics plays an important role also because it is also the first step to analyses by inverse dynamics that estimate the causes of the motion [1]. The kinematics study in the past was a time-consuming, laborious, and expensive task [1, 2]. In fact, the first attempt in this field was done using cinematography and manual methods were needed to extract the trajectory of body parts from the film [4].

Advances in technology have automated much the process of capturing motion data electronically and then extracting two- or three-dimensional trajectories [5]. Nowadays the stereo photogrammetric system is considered the gold standard for kinematics analysis; the main limitation of this system is that it can be used only in laboratory settings [2].

Laboratory assessment has been the standard setting for quantitative movement analysis for several decades; nowadays it represents a useful tool but not practicable to acquire a large group of subjects since it requires dedicated instrumentation, space, technicians, and the availability of the subjects to go to the laboratory. Assessing the kinematics of individuals in ecological condition is essential for offering the possibility to monitor large groups of population [6, 7].

In recent years, thanks to the progress in Microelectromechanical systems (MEMS) development, the availability of wearable inertial measurement units has allowed to quantitatively and easily assess movements also out of the laboratories [8]. In this scenario, Magnetic and Inertial Measurement Units (MIMU), which integrate multiple sensors (triaxial accelerometer, triaxial gyroscope and triaxial magnetometer), are the most promising sensing units for human kinematics analysis carried out both inside and outside a laboratory setting because they are relatively small and inexpensive, they require low power to operate and they provide useful kinematics quantities [9].

In this scenario, NCS Lab and the University of Bologna have decided to combine transversal skills with the aim of develop an innovative platform for the biomechanical analysis of the human body using wireless sensors: MIMU and surface electromyography (sEMG). The main reason behind this project was to offer a simple and accurate tool for performing kinematic and electromyographic analysis outside of the research laboratories in order to simplify the data acquisition process. Thanks to the knowledge of NCS Lab of the world of medicine and rehabilitation, it emerged that the weak point of the orthopaedic patient care process is objective tracking of the patients during the phases of their rehabilitation process. Nowadays only subjective scales are used in clinical settings for evaluating the kinematics and the pain of the patients; moreover, there is no agreement on which type of scale to use for each type of articulation [10]. As an example, at least 4 different indices exist for shoulder evaluation (Constant Score, Dash Score, Fuglmeyer Score, Brunnstrom Index) and there is no global agreement on which score is the most

suitable. Considering that the same problem exists for other human joints and considering that there is no objective data in the evaluation performed in the presented way, the need to have a tool to objectify kinematics clearly emerges. In this way will be possible to monitor the evolution of a disease in different periods, providing feedback to clinicians on their work and helping the patient in rehabilitative therapy.

Consequently, the aim of the presented work was the research and development of innovative hardware and software solutions for creating a unique tool for kinematics and electromyographic analysis of the human body. The project started in September 2016, in conjunction with the beginning of the present research project. After two years, the innovative wireless sensors and the biomechanics platform were ready to be tested in research laboratories (for precision and accuracy evaluation) and in clinical settings. Today, the platform is CE and FDA marked and is working all around the word acquiring kinematics data related to all the human joints, through the implementation of different biomechanical protocols [11, 12].

The research related to the presented PhD thesis is bound to the project. More specifically, in the first two years innovative hardware and software solutions were developed and implemented. A scalable and robust body sensor network hardware architecture was proposed, together with innovative algorithms for both sensors calibration and sensor-fusion for attitude estimation. These topics were the focus of two years of research, but will not be present in this document; a non-disclosure agreement protects what has been done on behalf of NCS Lab. The development of the above algorithms has taken place thanks to the knowledge gained studying algorithms for calibrating inertial and

magnetic sensors and for mapping magnetic fields, as reported in a published paper [13]. An important phase of the presented work is represented by the development of a procedure for characterizing the 3D magnetic vector in every point of the measurement volume. The work done has allowed us to broaden our knowledge of magnetic fields and how to insert procedures into the sensor fusion algorithm to take into account the distortions caused by them.

In the last year many clinical studies were carried out using the wireless platform developed. Many of the studies are not finished yet; in fact, in the great majority of the protocols written for data acquisition on patients, at least one year of follow-up is required. In the presented thesis, only two clinical studies related to the upper limb analysis were reported. The first one is related to the intra-inter operator agreement of the measures acquired by the developed platform. The second one is related to the analysis of biomechanical effects of Latissimus Dorsi Tendon Transfer on patients with rotator cuff tears.

In the next section a brief outline of the thesis is presented.

Outline of the thesis

The presented thesis is divided in five different chapters; each of them will speak specifically about a topic covered over the 3 years.
In Chapter I, the hardware, software and mathematical basis are presented. This chapter is also essential to understand some of the key points of sensor-fusion algorithms for attitude estimation and why the upper limb analysis represents a great challenge to be monitored.

In Chapter II, a method to characterize the 3D magnetic vector in every point of the measurement volume is presented and tested on both simulated and real data. The presented paper was essential in the project, because allowed to understand how the magnetic field behaved and consequently how to integrate that information in the sensor-fusion algorithm developed.

In Chapter III, a simple and effective algorithm for simultaneous calibration of magnetometer and accelerometer, without external references is presented. This paper represents the starting point from which the calibration algorithm that is currently used in the platform has been developed.

Chapter IV is dedicated to the evaluation of the developed platform for scapular kinematics assessment. Inter and intra-observer reproducibility and normative data for healthy adults were reported.

In Chapter V an evaluation of the Latissimus Dorsi Tendon Transfer is presented, showing how the shoulder kinematic changes after the transfer with respect to healthy subjects.

Finally, in a general conclusion is drawn, and directions for future research are explored.

References:

[1] D. Gordon, E. Robertson, Graham E. Caldwell, Joseph Hamill, Gary Kamen, Saunders N. Whittlesey; Research Methods in Biomechanics. ISBN-10: 0-7360-9340-0 (print)

[2] Picerno, P. 25 years of lower limb joint kinematics by using inertial and magnetic sensors: A review of methodological approaches. Gait Posture 2017, 51, 239–246.

[3] Cappello, A., Stagni, R., Fantozzi, S., & Leardini, A. (2005). Soft tissue artifact compensation in knee kinematics by double anatomical landmark calibration: Performance of a novel method during selected motor tasks. IEEE Transactions on Biomedical Engineering, 52(6), 992–998.

[4] A. Castagna, M. Rabuffetti, A. Montesano, M. Ferrarin, Role of gait analysis in the process of clinical decision making concerning post-stroke patients, Gait Posture. 33 (2011) S20– S21. doi:10.1016/j.gaitpost.2010.10.027

[5] Colyer S.L., Evans M., Cosker D.P., Salo A.I. A review of the evolution of vision-based motion analysis and the integration of advanced computer vision methods towards developing a markerless system. Sports Med.-Open. 2018;4:24.

[6] L. Chiari; A. Cappello, *Microsistemi indossabili per l'Ambient Assisted Living*, in: Sistemi indossabili intelligenti per la salute e la protezione dell'uomo, BOLOGNA, Patron, 2008, pp. 343 – 355

[7] Coni, Alice; Mellone, Sabato; Colpo, Marco; Guralnik, Jack M; Patel, Kushang V; Bandinelli, Stefania; Chiari, Lorenzo, *An Exploratory Factor Analysis of Sensor-Based Physical Capability Assessment*, «SENSORS», 2019, 19, pp. 1 - 24

[8] The MEMS Handbook Second Edition. MEMS Introduction and Fundamentals. Edited by Mohamed Gad-el-Hak. 2006 by Taylor & Francis Group, LLC

[9] Sabatini, A.M. Estimating three-dimensional orientation of human body parts by inertial/magnetic sensing. Sensors 2011, 11, 1489–1525, doi:10.3390/s110201489.

[10] P. Tamburini, D. Mazzoli, R. Stagni, Towards an objective assessment of motor function in sub-acute stroke patients: Relationship between clinical rating scales and instrumental gait stability indexes, Gait Posture. 59 (2018) 58–64. doi:10.1016/j.gaitpost.2017.09.033.

[11] Cutti, A. G., Giovanardi, A., Rocchi, L., Davalli, A., & Sacchetti, R. (2008). Ambulatory measurement of shoulder and elbow kinematics through inertial and magnetic sensors. Medical and Biological Engineering and Computing, 46(2), 169–178. doi:10.1007/s11517-007-0296-5

[12] Cutti, A. G., Ferrari, A., Garofalo, P., Raggi, M., Cappello, A., & Ferrari, A. (2010). "Outwalk": A protocol for clinical gait analysis based on inertial and magnetic sensors. Medical and Biological Engineering and Computing, 48(1), 17–25. doi:10.1007/s11517-009-0545-x

[13] Muraccini, M.; Mangia, A.L.; Lannocca, M.; Cappello, A. Magnetometer Calibration and Field Mapping through Thin Plate Splines. Sensors 2019, 19.

Chapter 1

Hardware and software basis

Introduction

In the presented chapter the hardware, software and mathematical basis useful to understand the background of the thesis are presented.

First, a hardware explanation related to the inertial and magnetic sensors used in this work (accelerometers, magnetometers, gyroscope) is presented. For each of the sensors many aspects will be clarified: what they measure, what are the main principles of functioning, and their usefulness in human motion analysis.

Following, a section related to the clinical interest in shoulder kinematics is reported. This is since in this thesis, the clinical study reported are focused in upper-limb kinematics. Anatomical and functional description of the shoulder are reported, with a large focus on the scapula-humeral rhythm.

An entire section of this chapter is dedicated to a mathematical overview of the different representations of the orientation; more specifically the orientation expressed in terms of quaternions is presented in detail because it is the convention used in the sensor-fusion algorithm developed.

Finally, an overview of the main techniques for orientation estimation starting from inertial and magnetic data is presented.

Accelerometer:

A monoaxial accelerometer is a device which measures the applied acceleration along an axis. It consists of an inertia element whose movement may be transformed into an electric signal [1], using the property of bodies to maintain constant translational and rotational velocity, unless disturbed by forces and torques, respectively. For this reason, it is called inertial sensor (as for the gyroscope).

Typically, a monoaxial accelerometer can be specified as a single-degree-of-freedom device, which has some type of seismic mass (sometimes called proof mass), a spring-like supporting system, and a frame structure with damping properties (Figure 1). Mass M is supported by a spring having stiffness k and the mass movement is damped by a damping element with a coefficient b. Mass may be displaced with respect to the accelerometer housing only in the horizontal direction.
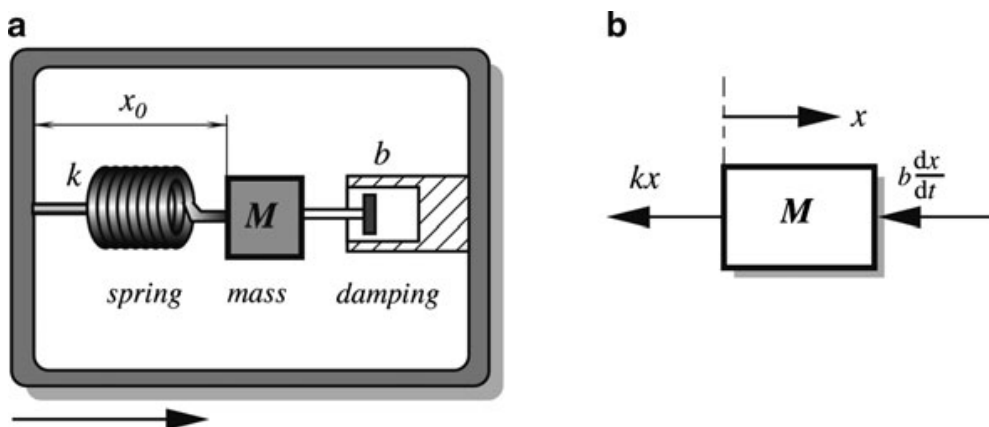
Figure 1. (a) A schematic representation of the mechanical model of an accelerometer is reported. (b) The related free-body diagram of mass.

A detailed mathematical model of a monoaxial accelerometer can be found in [1], together with the resolution of the related differential equation.

The differential equation that links acceleration and displacement of mass M [1] suggests that it is enough to measure displacement to directly derive the body acceleration. Due to this fact, any displacement transducer (capable of measuring microscopic movements under strong vibrations or linear acceleration) can be employed to generate an electrical signal as function of the acceleration. Examples are capacitive, piezoresistive and piezoelectric transducers.

A capacitive displacement conversion is one of the proven and reliable methods. A capacitive acceleration sensor essentially contains at least two components, where the first is a "stationary" plate (i.e., connected to the housing) and the other is a plate attached to the inertial mass, which is free to move inside the housing. These plates form a capacitor whose value is function of a distance between the plates.

A piezoresistive accelerometer incorporates a strain gauge that measures strain in the mass-supporting springs. The strain can be directly correlated with the magnitude and rate of the mass displacement and, subsequently, with an acceleration.

The piezoelectric effect has a natural application in sensing vibration and acceleration. The effect is a direct conversion of mechanical energy into electrical energy in a crystalline material composed of electrical dipoles.

Everything illustrated for the monoaxial accelerometer can be easily generalized to the triaxial accelerometer, which consists in three orthogonal monoaxial accelerometer, providing measurements on each axis.

Using accelerometers provides a practical and low-cost method for monitoring human movements. They are used to measure physical activity levels, for movement identification and classification, and to monitor movements such as gait, sit-to-stand, postural sways and falls.

Gyroscope

The gyroscope is a sensor which converts an angular velocity into an electrical signal by a known relationship.

Before advancement of a GPS (global positioning system), besides a magnetic compass, a gyroscope probably was the most common navigation sensor. Nowadays, applications of gyroscopes are much broader than for navigation. They are used in the stabilization devices, weapons, robotics, tunnel mining, and in many other systems where a stable directional reference is required.

A gyroscope is a "keeper of direction", like a pendulum in a clock is a "keeper of time". A gyro operation is based on the fundamental principle of the conservation of angular momentum: in any system of particles, the total angular momentum of the system relative to any point fixed in space remains constant, provided no external forces act on the system. For this reason, it is considered an inertial sensor.

Two main different categories of gyroscope are available (mechanical and optical), but optical gyroscopes are not suitable for human motion analysis due to their large size and high costs.

A mechanical gyro is comprised of a massive disk free to rotate about a spin axis (Figure 2) and it is based on Coriolis effect, where rotation about an axis

causes a transfer of energy between two vibratory modes that are orthogonal to the axis of rotation and also to each other.

A detailed mathematical model of a monoaxial gyroscope can be found in [2].
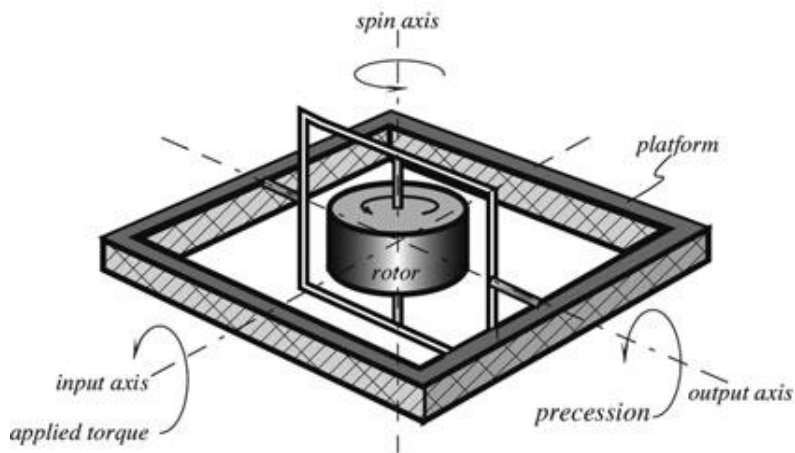
Figure 2: A mechanical gyroscope with a single degree-of-freedom is reported.

Everything illustrated for the monoaxial gyroscope can be easily generalized to the triaxial gyroscope, which consists in three orthogonal monoaxial gyroscope, providing measurements on each axis.

Vibrating mass gyroscopes are small, inexpensive, and have low power requirements, making them ideal for human movement analysis [3].

Magnetometer

A magnetometer is a device which measures the strength and direction of the magnetic field in its system of reference. The first magnetometer capable of measuring the absolute magnetic intensity was invented by Carl Friedrich Gauss in 1833 and notable developments in the 19th century included the Hall effect, which is still widely used.

Magnetometers are widely used for measuring the Earth's magnetic field, and in geophysical surveys, to detect magnetic anomalies of various types. In an aircraft's attitude and heading reference system, they are commonly used as a heading reference.

Probably the most widely used magnetic sensors are the Hall effect sensors. They work on the principle that a voltage can be detected across a thin metallic element, when the element is placed in a strong magnetic field perpendicular to the element's plane (Figure 3). The detected voltage is referred to as the Hall voltage.

$$V_{Hall} - k \, |I \times B|$$
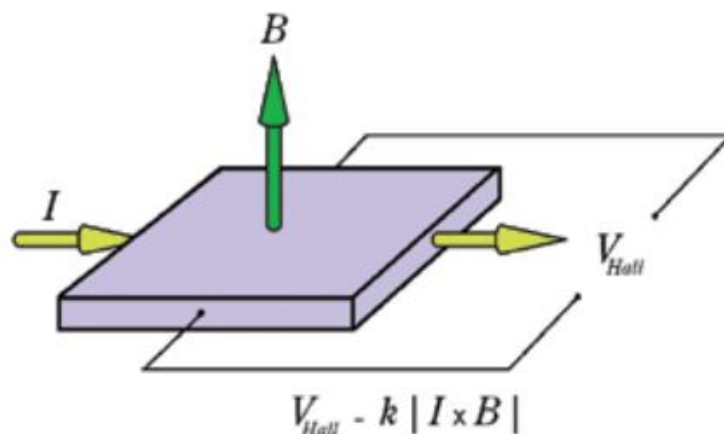
Figure 3. The Hall Effect principle works by detecting a voltage across a metallic surface (the Hall voltage) in response to a magnetic field that's perpendicular to the metallic surface.

Anisotropic magnetoresistance (AMR) is another approach that was introduced a few years ago [4]. This concept makes use of a common material, permalloy, to act as a magnetometer. Permalloy is an alloy containing roughly 80% nickel and 20% iron. The alloy's resistance depends on the angle between the metallization and the direction of current flow. In a magnetic field, magnetization rotates toward the direction of the magnetic field and the rotation angle depends on the external field's magnitude.

Permalloy's resistance decreases as the direction of magnetization rotates away from the direction in which current flows and is lowest when the magnetization is perpendicular to the direction of current flow. The resistance changes roughly as the square of the cosine of the angle between the metallization and the direction of current flow.

The most recent arrival on the low-cost-magnetometer scene is Lorentz force magnetometers — MEMS devices that detect the motion of a miniature bar magnet. The fact that these magnetometers can be manufactured on the same wafer holding MEMS and CMOS circuitry could mean that devices based on this method can be made at low cost, but this remains to be seen. The Lorentz force sensor's magnetic field resolution is limited by electronic noise from the detection electronics, and its structure's relatively high natural frequencies make it less sensitive to acceleration.

One of many advantages of using magnetic field for sensing position, orientation or distance is that any nonmagnetic material can be penetrated by the filed with no loss of accuracy. Stainless steel, aluminum, brass, copper, plastics, masonry, and woods can be penetrated, without loss of accuracy.

The big disadvantage is due to the presence of external magnetic distortion.

Clinical interest in shoulder kinematics

The shoulder is a complex of joints that allows the relative motion of the humerus respect to the thorax [5]; this complex of joints is considered the most mobile of all the joints of the human body. It is characterized by three degrees of freedom that allow the orientation of the humerus in the three plans of movements. These are defined by the three main anatomical axes: the transverse axis, the anterior-posterior axis and the longitudinal axis. Movements performed on the sagittal plane, around the transverse axis, are called flexion-extension, while those performed in the frontal plane (around the anterior-posterior axis) are referred to as adduction-abduction. As for the rotational movements (internal and external) of the arm, these occur around the longitudinal axis of the humerus. The main bones that form the shoulder structure are clavicle, humerus, scapula and thorax (Figure 4).
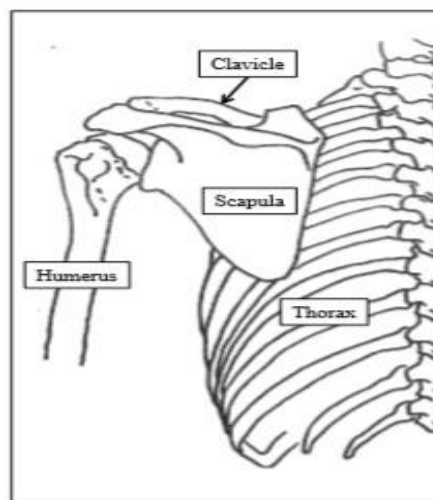
Figure 4: Shoulder bones (clavicle, scapula, humerus and thorax) in a schematic representation.

These bones define five joints called: sternoclavicular (between sternum and clavicle), acromioclavicular (between scapula and clavicle), glenohumeral or scapulohumeral (between the glenoid fossa and the humerus), under-deltoid (between acromion and humerus) and scapulothoracic (between scapula and thorax). The first three joints are in anatomical sense, i.e. they consist of two surfaces covered by cartilage, while the last two consist of two surfaces which slide one with respect to the other without any interposed cartilage (i.e. are in the physiological sense). Among the five joints, the glenohumeral is one of the most complex articulation. This is due to the fact that it is able to cover a wide range of movement which, however, makes the structure vulnerable and prone to injuries. The stability of the joint in ensured by arm's and rotator cuff muscles, coraco-humeral and glenohumeral ligaments and the acromion and the subacromial bursa. All of these elements have the function of preventing from dislocations, keeping the humeral head in contact with the glenoid fossa during movements. Going into more detail, the rotator cuff is made up of a group of four muscles and tendons (supraspinatus, infraspinatus, teres minor and subscapularis), which stabilize the shoulder. Moreover, it is possible to define the coordinated movement between scapula and humerus, when this latter is elevated, as the "scapulo-humeral rhythm" (SHR). Typically, the analysis of the SHR, from a clinical point of view, is conducted during the flexion and abduction movements of the humerus that occur respectively in the sagittal and in the frontal plane. Looking at the movement of the shoulder in these two planes, it emerges that around 2/3 of the movements (that is 120°) is due to the glenohumeral mobility, while the remaining part is due to scapulothoracic mobility (that is 60°). Based on the muscles involved, the

flexion and abduction movements can therefore be divided into three phases. Considering the flexion movement, it will be:

- from 0 to 50 – 60° anterior deltoid, coracobrachialis, greater pectoralis are recruited;

- from 60 to 120° the SHR starts and trapezius and latissimus dorsi are involved;

- from 120 to 180° the scapulo-thoracic and gleno-humeral movements interrupt and spinal muscles are activated.
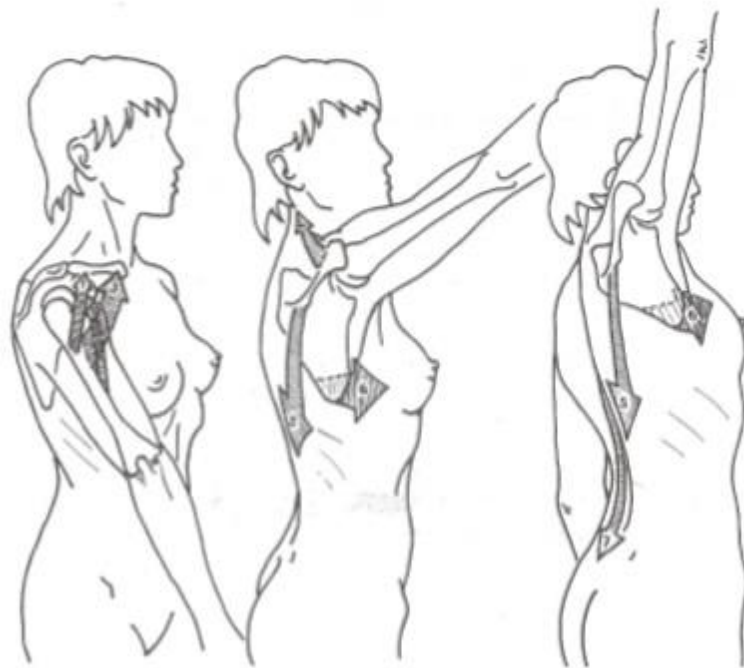
Figure 5: Muscles involved in shoulder flexion at different phases of the movement.

As far as abduction is concerned, it follows that:

- from 0 to 90° deltoid and supraspinatus are recruited;

- from 90 to 150° the scapulo-humeral joint is blocked and the movement requires the involvement of the shoulder girdle (trapezius and latissimus dorsi);
- from 150 to 180° the spinal muscles are activated
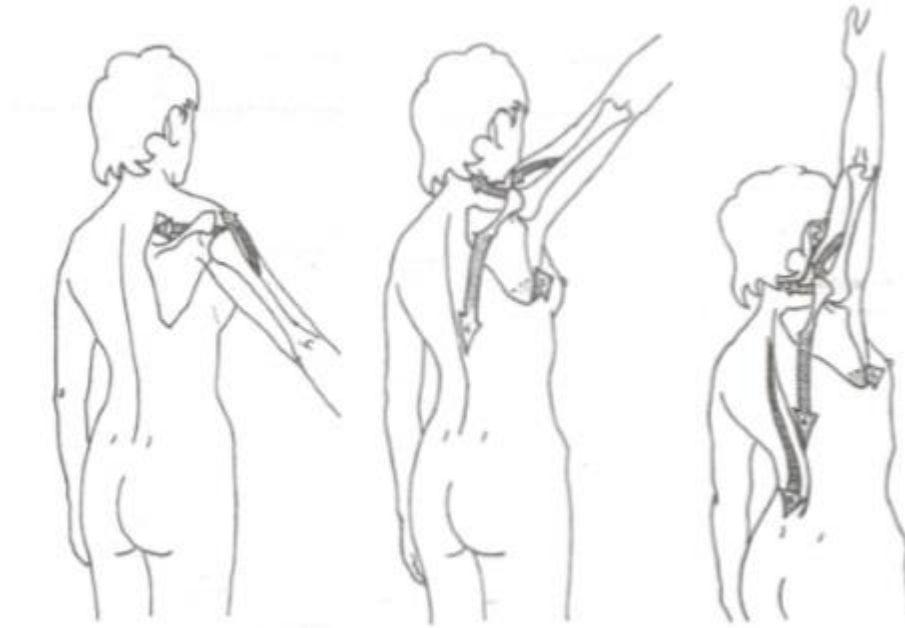
Figure 6: Muscles involved in shoulder abduction at different phases of the movement.

On the other hand, the scapula is described based on three additional rotation axes which define three different movements (Figure 7): medio-lateral rotation respect to the sagittal axis, anterior-posterior tilting around the transverse axis and internal-external rotation (or protraction-retraction) relative to the longitudinal axis. The balance between the structures that make up the shoulder can be altered as a result of traumatic events or degenerative pathologies that can lead to musculoskeletal diseases. Nowadays shoulder pathologies are an increasingly problem among workers and athletes. Some of

the work-related factors associated with shoulder pain, which are shown in literature, are, for example, repetitive movements and forceful manual exertion. Research studies conducted with respect to this topic, report rotator cuff tear as the most common shoulder pathology and the main source of morbidity in working population: these factors contribute to a high clinical interest in the study of shoulder kinematics. Moreover, a dysfunction of the rotator cuff anatomical structures can cause pain, joint weakness, lack of force and alterations in the scapula kinematics.
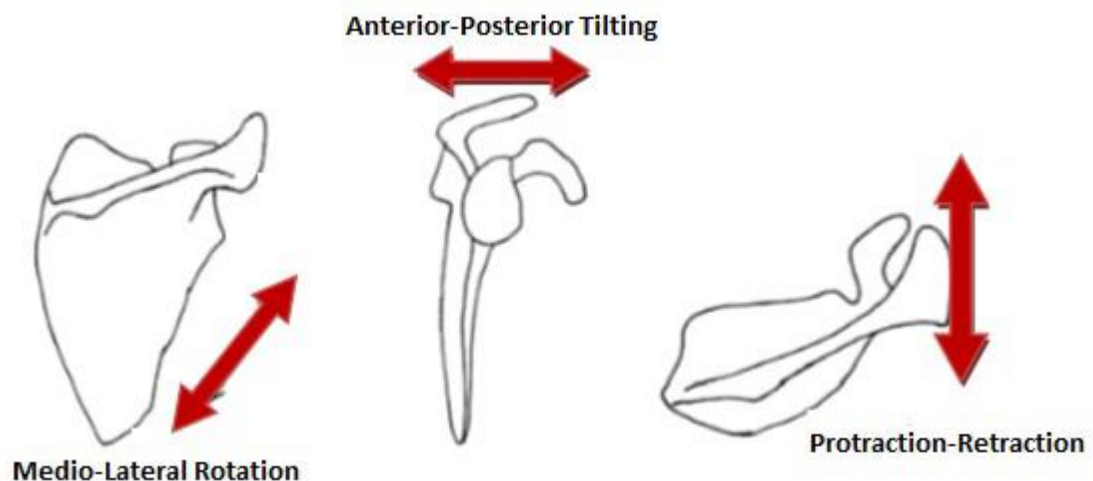
Figure 7: Scapula rotations: medio-lateral rotation (also called up-down rotation), anterior-posterior tilting, and internal-external rotation (also called protraction-retraction).

More specifically, this may result in changes in the scapulo-humeral rhythm. This alteration can be traced back to two main causes, namely protective factors or muscles dysfunctions. In the first case the subject uses adaptive movements to counteract perceived pain which lead to a reorganization in terms of muscle activity and scapula kinematics. With regard to muscles dysfunctions, these

can be caused by a delay in the activation of a muscle or its inhibition and can contribute to the emergence of shoulder diseases. Shoulder pain, combined with upper limb dysfunctions, reduces the mobility of the joint and, therefore, the functional autonomy of the subject. The purpose of rehabilitative treatments is to recover the functionality of the upper limb and reduce pain in order to improve the patient's quality of life. Currently, in outpatient clinical settings, functional tests or clinical scales are used for patient evaluation. The most commonly used are, for example, the DASH questionnaire (Disabilities of the Arm, Shoulder and Hand), the Simple Shoulder Test (SST), the Constant-Murley test and the Visual Analogue Scale (VAS) for pain assessment and joint stiffness. At the expense of ease of execution, these tests and clinical scales do not allow an objective evaluation and are not able to provide enough information to specifically analyse the joint movement. Accurate in-vivo measurements (possibly in real-life conditions) are therefore necessary for a more thorough understanding of scapular kinematics in relation to shoulder pathologies. The quantitative analysis of the SHR and of the cinematic features of the shoulder joint is a basic aspect for a complete evaluation of shoulder performance. It is also fundamental in order to make a diagnosis, to monitor the progress of a pathology, to check the result of a treatment or to plan a rehabilitation process. Unfortunately, these quantitative measures can only be carried out in a few highly advanced medical centres which are provided with motion analysis laboratories and expensive optoelectronic systems. Although these systems allow an accurate and non-invasive analysis of movement, they are very complex, hard to move and bulky to be placed in small clinics. Furthermore, they are sensitive to external lighting sources and constrain

kinematic analysis to a limited volume of space, preventing applicability for sports performance studies, home-care rehabilitation sessions or monitoring of daily activities. For these reasons, one of the aim of the proposed work is the developing of a new technology for motion analysis, based on inertial and magnetic measurements systems (MIMUs).

More detailed information related to shoulder kinematics and the importance of tracking it can be found in [6].

Representation of orientation

The orientation can be generally represented in three principal forms: Direction Cosine Matrix, Euler angles and quaternion. Considering a rigid body, that's moving on or near the earth surface (at speed far below orbital velocity), it is possible to describe its orientation using two coordinate systems: the earth-fixed coordinate system and the body-fixed one. The first is an inertial coordinate system specified by the right-handed orthonormal basis E = {e1 e2 e3}, whose axes are defined in a conventional and fixed way. A possible solution is to consider the 3-axis directed to the local north, east and down directions, as reported in Figure 8 (another very popular convention is the North, West, Up convention). The body-fixed coordinate system is a non-inertial coordinate system specified by the right-handed orthonormal basis B = {e1' e2' e3'}. In the aeronautics jargon, its coordinate axes are named 'out the nose', 'out the right side' and 'out the belly' (Figure 8). An arbitrary vector x can, then, be expressed in the following equivalent forms:

$$x = x_1 e_1 + x_2 e_2 + x_3 e_3 \qquad (1)$$

$$x = x'_1 e'_1 + x'_2 e'_2 + x'_3 e'_3$$
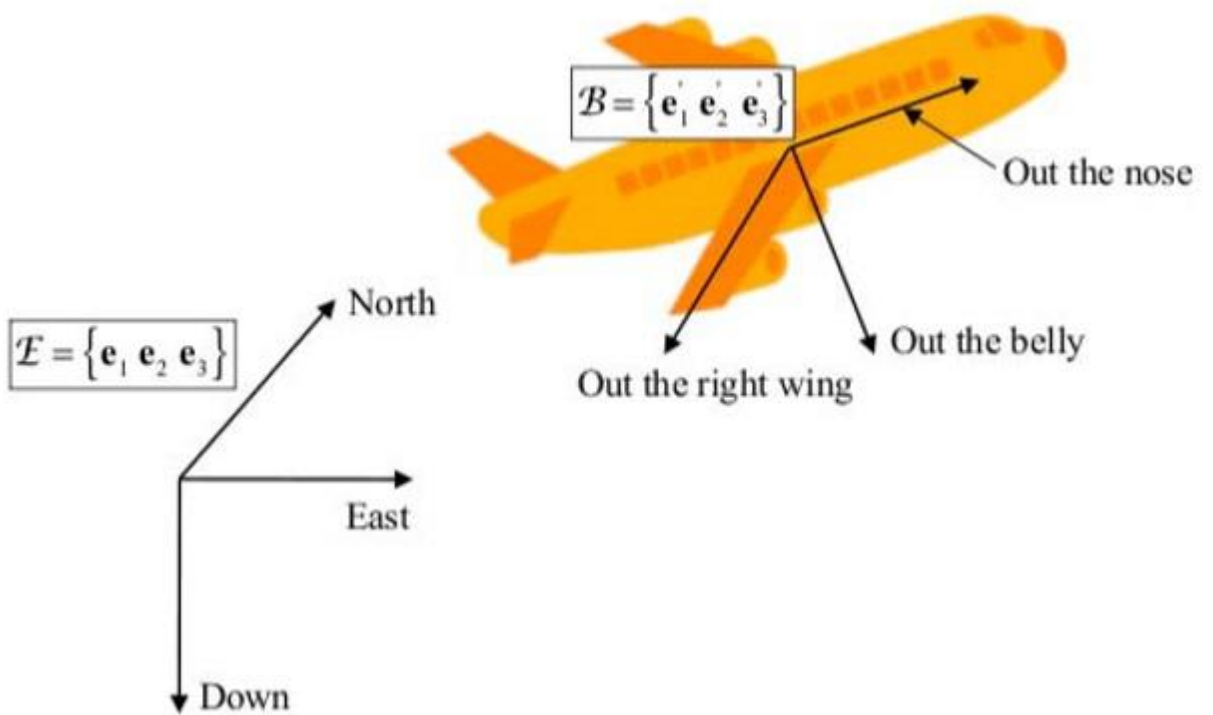
Figure 8: Representation of the two coordinate systems as presented in [7].

It is also possible to represent the vector x considering either basis, according to the relation:

$$x_B = {}^B_E C \, x_E \qquad (2)$$

where the indices B and E indicate which base is used for the vector representation and $^B_E C$ identifies the direction cosine matrix (DCM, also called orientation matrix). The columns of the DCM are the representation of the e_i with respect to B while the rows are the representation of the e'_i with respect to E (in both cases i = 1; 2; 3). This matrix is a 3 X 3 orthogonal matrix with unit determinant and belongs to the SO (3), that is a 3D special orthogonal group of rotation matrices. From the orthogonality requirement it is possible to obtain a lower dimensional parameterization of the matrix, imposing six constraints on its nine elements. It is required that the column (row) vectors have a unit norm and that are mutually orthogonal. Therefore, the rotation matrix through an angle $\boldsymbol{\theta}$ can be written, according to the Euler's formula, in the following two equivalent expressions:

$$\begin{cases} R(n, \boldsymbol{\theta}) = c\boldsymbol{\theta}\, I_3 + (1 - c\boldsymbol{\theta})nn^T - s\boldsymbol{\theta}\, n[X] \\ R(n, \boldsymbol{\theta}) = I_3 - s\boldsymbol{\theta}\, n[x] + (1 - c\boldsymbol{\theta})n[X]^2 \end{cases} \quad (3)$$

Where I3 denotes the 3 X 3 identity matrix, n denotes any unit column vector, c$\boldsymbol{\theta}$ and s$\boldsymbol{\theta}$ are compact notation for cos$\boldsymbol{\theta}$ and sin$\boldsymbol{\theta}$ respectively.

The orientation, in terms of the rotation vector, can also be expressed from the equation:

$$\boldsymbol{\theta} = \theta\boldsymbol{n} \qquad (4)$$

In fact, according to the Euler's theorem, the motion of a rigid body with one point fixed is characterized by a rotation by an angle $\boldsymbol{\theta}$ about some rotation

axis n. It is important to note that the rotation vector space does not contain singularity points.

The Euler angle formulation for the orientation is defined in terms of three consecutive rotation through three body-referenced Euler angles (i.e. ϕ, θ, φ). So, the rotation matrix is conceptually easy to understand, but may reach a singularity state commonly referred to as 'gimbal-lock'.

Finally, starting from Euler's formula it is possible to derive another mathematical representation of the orientation matrix based on the Euler-Rodrigues symmetric parameters, aka quaternion:

$$R(q, q_4) = (q_4 - |q|)^2 I_3 + 2qq^T - 2q_4 q[X] \qquad (5)$$

Where

$$q = \begin{bmatrix} q_1 \\ q_2 \\ q_3 \end{bmatrix} = \sin(\theta/2)\,\boldsymbol{n}\,, q_4 = cos(\theta/2) \qquad (6)$$

Generally, q is called the vector part, while q_4 is the scalar part of the quaternion q = [q$^\text{T}$ q_4]$^\text{T}$. The rules in quaternion operations can be found in [7]. The advantage of using this representation is that it has the lowest dimension compared to any globally non-singular orientation parameterization. In addition, because -q identifies the same rotation of q, the quaternion representation is redundant and a rotation through an angle θ about the n-axis can be expressed as a rotation trough an angle θ about the n axis.

For both the DCM and the quaternion formulation, it is possible to determine the kinematic equations that describe the motion of a rigid body, computing

the temporal derivative of the chosen orientation representation. As for the orientation matrix DCM, the motion is characterized by the Poisson's kinematic equations that represent a system of first-order linear differential equations:

$$\frac{d}{dt}\, C_E^B = \, -[w_B X]C_E^B \qquad\qquad (7)$$

where w_B is the body-referenced angular velocity.

On the other hand, the time evolution of a quaternion, with angular velocity w_B is achieved by resolving the following first-order linear differential equation system:

$$\frac{d}{dt}\, q = \, \Omega\,(w_B)\, q \qquad\qquad (8)$$

Where $\Omega\,(w_B)$ is a 4 X 4 skew symmetric matrix.

The main advantages of using the quaternion parameterizations over the rotation matrix are related to errors associated with numerical integration of the kinematic equations and to the computational speed. In fact, quaternion representation is characterized by fewer numerical integration errors and does not require the computation of trigonometric functions.

More detailed information related to quaternions can be found in [8].

Algorithms for orientation estimation

Data provided by body-fixed inertial/magnetic sensors are affected by noise and time-varying biases. Therefore, sensors-fusion algorithms are necessary to process the data and obtain a smooth and bias-free estimation of the orientation.

There are mainly two different types of algorithms, proposed to solve the so-called Wahba's problem (originally introduced in 1965), that provide an estimate of the orientation: deterministic and stochastic. The first one is a least-squares approach that tries to minimize a least-square loss function. It consists in a constrained least-squared optimization problem whose goal is to find the rotation matrix from vector measurements taken at a single time. This single-frame method relates to the operation of gyro-free aiding sensor systems and it can solve Wahba's problem without the need of an a priori estimate. The deterministic approach is based on the vector matching concept and, to work properly in human motion tracking, requires the measurements of constant reference vector that are gravity and earth magnetic field.

The stochastic approach (or Kalman filtering, first proposed in 1961) is based on the minimum-variance sequential estimates of orientation and of other parameters, such as sensor biases, using information obtained from motion dynamics. In other words, in order to produce the most accurate estimate of the system state, these algorithms use a model for predicting some aspects of a dynamic system and a model of the sensor measurements. The dynamic state is estimated using a Bayesian approach, which is based on propagating the

probability density function (PDF) of the system state in a recursive manner through the application of the Bayes' rule:

$$p(x_k \mid z_{1:k}) \propto p(z_k \mid x_k) \, p(x_k \mid z_{1:k-1}) \quad (9)$$

where $p(x_k \mid z_{1:k})$ is the likelihood function de_ned by the measurement model as follow:

$$z_k = h_k (x_k, v_k) \quad (10)$$

The term xk represents the system state and vk is the measurement noise whose statistics is known. Generally, h is a nonlinear time-variant function that performs a mapping of the state of the system to the measured state zk. Moreover, in (9), $p(x_k \mid z_{1:k-1})$ identifies the prior PDF of the state at time tk. Kalman filtering based techniques model the state as a Gaussian distribution given the system's model.

The knowledge of the $p(x_k \mid z_{1:k})$ (that is the posterior PDF) allows to estimate the state and to obtain measures of the accuracy of these estimates.

It is important to notice that both the presented sensor-fusion algorithms operate in the temporal domain; however, there are other approaches that operate in the frequency domain: complementary filters. These filters put together gyroscope data with acceleration and magnetic field measurements from sensors, in order to obtain an orientation estimation in quaternion form. A complementary filter performs high-pass filtering on the orientation estimated from gyroscope data affected by low-frequency noise. On the other

hand, it performs a low-pass filter on accelerometer data affected by high-frequency noise: the fusion between the two estimations can ideally return an all-pass and noise-free orientation estimation. A schematic representation of a complementary filter for fusing only accelerometer and gyroscope data is reported in Figure 9:
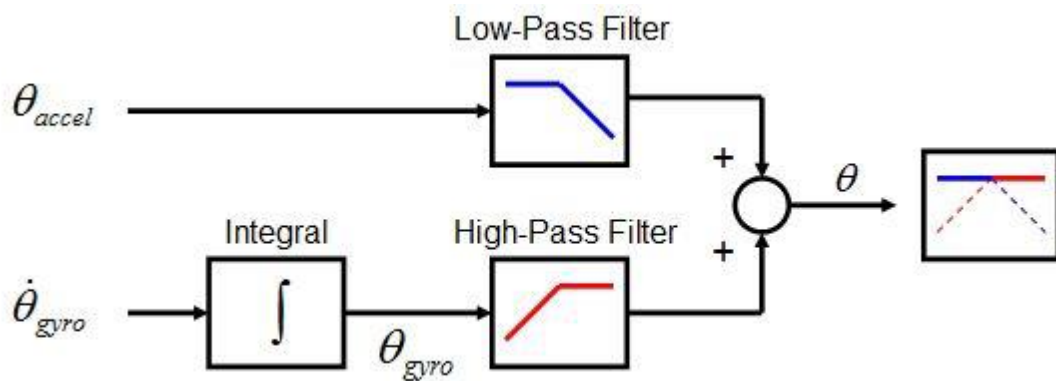
Figure 9: A schematic representation of a complementary filter for fusing accelerometer and gyroscope data is reported.

Without going into the conceptual and implementation details of the different sensor-fusion algorithms, the only thing that can be said is that in literature there is not yet an algorithm that is able to optimally estimate the orientation starting from inertial and magnetic sensors. Each of the algorithms presented in the literature has its strengths and weaknesses. More detailed information related to sensor-fusion algorithms can be found in [7].

In the presented work, an innovative sensor-fusion algorithm was proposed, implemented and tested, offering very promising results. The details of the

algorithm developed can not be reported in this thesis because a non-disclosure agreement protects what has been done on behalf of NCS Lab.

Getting an accurate estimate of orientation is important because the information obtained from the orientation of the body on which the sensor is fixed allows to evaluate the joint kinematics. More specifically, for joint kinematics evaluation, different sensing units will be placed on each body segment of interest and for each of them an anatomical reference system will be defined. Then, the relative orientation between body segments can easily be found. In fact, according to standards set by the International Society of Biomechanics (ISB), joint kinematics can be obtained from knowledge of the relative orientation between two adjacent anatomical reference systems.

References

[1] Handbook Of Modern Sensors. Physics Design And Applications. Jacob Fraden. Springer. ISBN 978-1-4419-6465-6

[2] MEMS Introduction and Fundamentals. Edited by Mohamed Gad-el-Hak. ISBN 0-8493-9137-7

[3] From inverted pendulum to N-link chain: inertial sensors-based assessment of movement kinematics and dynamics for functional evaluation and rehabilitation. Valeria Fuschillo. PhD thesis

[4] Cai, Y., Zhao, Y., Ding, X., & Fennelly, J. (2012). Magnetometer basics for mobile phone applications. Electronic Products (Garden City, New York), 54(2).

[5] Validation and application of a shoulder ambulatory motion analysis protocol. Ilaria Parel. PhD thesis.

[6] Kibler, W. B. (n.d.). Scapular Dyskinesis and Its Relation to Shoulder Injury Abstract, 364–372.

[7] Sabatini, A.M. Estimating three-dimensional orientation of human body parts by inertial/magnetic sensing. Sensors 2011, 11, 1489–1525, doi:10.3390/s110201489.

[8] Valenti, R. G., Dryanovski, I., & Xiao, J. (2015). Keeping a good attitude: A quaternion-based orientation filter for IMUs and MARGs. Sensors (Switzerland), 15(8), 19302–19330. https://doi.org/10.3390/s150819302

Chapter 2

Magnetometer Calibration and Field Mapping through Thin Plate Splines[1]

Abstract:

While the undisturbed Earth's magnetic field represents a fundamental information for orientation purposes, magnetic distortions have been mostly considered as a source of error. However, when distortions are temporally stable and spatially distinctive, they could provide a unique magnetic landscape that can be used in different applications, from indoor localization to sensor fusion algorithms for attitude estimation. The main purpose of this work, therefore, is to present a method to characterize the 3D magnetic vector in every point of the measurement volume. The possibility of describing the 3D magnetic field map through Thin Plate Splines (TPS) interpolation is investigated and demonstrated. An algorithm for the simultaneous estimation of the parameters related to magnetometer calibration and those describing the magnetic map, is proposed and tested on both simulated and real data. Results demonstrate that an accurate description of the local magnetic field using TPS interpolation is possible. The proposed procedure leads to errors in the estimation of the local magnetic direction with a standard deviation lower than 1 degree. Magnetometer calibration and magnetic field mapping could be integrated into different algorithms, for example to improve attitude estimation in highly distorted environments or as an aid to indoor localization.

Keywords: movement analysis, wearable sensors, magnetometer calibration, Earth's magnetic field mapping, thin plate splines

1. Introduction

The Earth's magnetic field has been used by the humans for centuries as a navigation tool. Evidence suggests that the animals use Earth's magnetic field as well [1,2]. Moreover, some animals, such as spiny lobsters, are able not only to detect the direction of Earth's magnetic field, they can even sense their true position relative to their destination [3]. Their ability seems to suggest that the knowledge of magnetic information could lead to the determination of the position.

It is well known that the Earth's magnetic field is not a predefined and time-constant vector [4]. It depends on the latitude and longitude coordinates and suffers from different types of fluctuations due to the diurnal cycle, movement of magnetic poles, and more randomly, to geomagnetic storms caused by solar flares [5]. But, for all practical purposes, especially for the use of magnetic data in sensor fusion algorithms to estimate the local orientation of a Magnetic and Inertial Measurement Unit (MIMU), these fluctuations are negligible when compared to the typical point to point variation of magnetic field inside a building [4,6,7]. The local magnetic distortion depends on the position and is not known a priori. In fact, its intensity and direction strongly depend on the proximity of metallic objects with high relative permeability, such as iron reinforcements in buildings, permanent magnets, motors and electronic devices.

Until a few years ago, these distortions have been mostly considered as a source of error for compasses and magnetometers in indoor localization and in sensor fusion algorithms, as they interfere with compass direction. However,

if the distortions are temporally stable and spatially distinctive [4,5,8], they provide a unique magnetic landscape that can be used for different purposes. With regard to this, Haverinen et al. [3] have shown that the anomalies in indoor magnetic fields can be manually collected to build a map that can be used to localize both robots and humans equipped with wearable sensors.

It should be noted that magnetic distortions are generated not only by external magnetic materials (e.g iron reinforcements in buildings or electronic devices). In fact, there are also self-induced distortions caused by the sensing element itself [9,10]. These types of distortion could be divided into two groups: hard and soft iron [9]. These two types of effects arise, respectively, from permanent magnets and DC currents on the compass platform and from the interaction of the Earth's magnetic field and any high permeability material on the same platform. While hard iron effects will remain constant in the MIMU reference frame for all compass orientations, soft iron effects do not remain constant as they vary with the orientation of the sensor relative to the direction of the Earth's magnetic field. To compensate for these sources of distortion, many algorithms for calibrating the magnetometer data have been proposed [9–11]. All of them require an acquisition where the magnetometer explores all possible orientations.

In the literature different algorithms to interpolate and extrapolate a mapping of the magnetic field in an internal environment have been suggested [3-5,12,13]. Solin et al. [12] proposed a Bayesian non-parametric probabilistic modelling approach for interpolation and extrapolation of the magnetic field. In [4] the map is collected by a robotic platform with minimal sensor equipment. It is demonstrated that a simple magnetometer along with some

odometric information suffices to construct the map via a Simultaneous Localization and Mapping (SLAM) procedure based on the Rao-Blackwellized particle filter to provide recursive Bayesian estimation.

To the best knowledge of the authors, all previous works use pre-calibrated data from the magnetometer to estimate the magnetic field map in the measurement volume. This implies that at least two acquisitions must be performed in order to i) calibrate the magnetometer, and ii) estimate the magnetic field map. In this paper a new technique is proposed, based on a single acquisition, for the simultaneous i) calibration of the magnetometer, and ii) estimation of the Earth's magnetic field map in a fixed system of reference. The approach relies on the use of 3D-TPS, a spline-based technique for data interpolation and smoothing [23].

Reviewing the relevant literature, it appears that most of the work related to the estimation of magnetic map is focused on 2D mapping [3-5,13,14], even if a 3D approach is certainly preferable in applications such as robotics, biomechanics and drone control.

The information obtained could be integrated into sensor-fusion algorithms for the orientation estimate. Several studies have highlighted the lack of accuracy in the orientation data provided by MIMU in the movement analysis laboratory due to the presence of irregularities caused by iron reinforcements in floors, walls and ceilings, or other equipment [7,15,16]. Currently, there is no robust solution in the literature regarding this issue.

Different strategies have been adopted to tackle this problem [6,13]. When distortions have short duration a possible solution is to complete the Kalman

Filter dynamical model with additional equations modelling the magnetic drift using random-walk or first-order Gauss-Markov models [13].

When the magnetometer output is corrupted by the presence of electromagnetic devices over a long period of time this approach does not work properly. The knowledge of the field map could make it possible to overcome these limitations.

Another area where these maps could be used is for indoor localization purposes, thereby offering a promising alternative to traditional methods for achieving GPS-level localization indoors [14]. Traditionally, Simultaneous Localization And Mapping (SLAM) in robotics has been tackled with laser or vision-based approaches [8]. However, other more unconventional sensor approaches for SLAM have recently attracted attention, such as WiFi-based methods [19,20] or depth sensors [17]. The use of magnetometer for SLAM represents a new and low-cost challenge [8].

The aim of this study is to provide and test a single procedure to simultaneously calibrate the triaxial magnetometer and map the 3D magnetic field in the acquisition volume. To this end, a model based on thin plate splines (TPS) interpolation was developed and tested using both simulated and experimental data. The results suggest that it is possible to obtain an accurate and stable 3D description of the magnetic field in the measurement volume.

2. Materials and Methods

2.1. Model of a triaxial magnetometer in the presence of magnetic field distortion

Two right-handed orthogonal reference systems are defined: a Laboratory Reference System (LRS), which is assumed to be fixed to the Earth and a Sensor Reference System (SRS) that is integrated with the magnetometer.

In this work, the axes of LRS are defined by reference to the Nord-West-Up (NWU) convention in which the x, y and z-axes point to magnetic north, magnetic west and upward respectively [6]. The above-mentioned convention makes it possible to build an LRS without any external reference, except for gravity and magnetic field.

The magnetic field at a given point $\mathbf{P}$(x, y, z) is given by the contribution of both the Earth's magnetic field and the local distortion. In a short observation time interval, it can be assumed that the Earth's magnetic field is a constant vector, $\mathbf{B}_0$ [Gauss], in the whole measurement volume. Furthermore, let us assume that the local distortion at point $\mathbf{P}$, $\mathbf{\Delta B}(\mathbf{P})$ is time-constant only in presence of motionless high permeability materials or static magnetic field generators in or near the measurement volume. In the proposed algorithm, and consequently in the following equations, local distortions were assumed temporally stable and spatially distinctive.

An ideal triaxial magnetometer measures the components of the local magnetic field along the three mutually orthogonal axes, x, y, z, of the SRS. The ideal magnetometer output at time k (called also frame) is given by Equation (1):

$$\mathbf{m}_k^I = \mathbf{R}_k^T \left[\mathbf{B}_0 + \mathbf{\Delta B}(\mathbf{P}_k) \right] = \mathbf{R}_k^T \mathbf{B}(\mathbf{P}_k) \qquad (1)$$

where $\mathbf{R}_k$ is the time-varying orientation matrix of the SRS with respect to the LRS, and $\mathbf{P}_k$ is the position vector of the sensor.

Under actual conditions, we must take into account instrumentation errors and magnetic deviation. The instrumentation errors include: i) cross-talk effects due to non-orthogonal measurement axes, ii) non-unitary and generally different gains along the three axes, iii) offset and iv) additive noise, supposed as a Gaussian wideband noise [10] as reported in [25]. The magnetic deviation includes: v) soft iron and vi) hard iron effects. Both instrumentation errors and magnetic deviation can be accounted for by using a simple linearized model [10,22], expressed at frame k:

$$\mathbf{m}_k = \mathbf{W}\mathbf{m}_k^I + \mathbf{O} + \mathbf{v}_k \qquad (2)$$

where $\mathbf{m}_k$ is the actual measured magnetic field, $\mathbf{W}$ a 3x3 matrix depending on i), ii) v), $\mathbf{O}$ a 3x1 bias vector depending on iii) and vi), and $\mathbf{v}_k$ the additive noise.

For magnetometer calibration, $\mathbf{W}$ and $\mathbf{O}$ must be estimated. Several studies have proposed different methods for estimating optimal calibration parameters [9–11].

The first innovative contribution of this work is to model the local magnetic field map by using a 3D Thin Plate Spline (TPS) interpolant [23]. TPS are a spline-based technique for data interpolation and smoothing. Its name refers to a physical analogy with the bending of a thin sheet of metal. Just as the metal has rigidity, so the TPS fit also resists bending, implying a handicap

involving the smoothness of the fitted surface. Because of its elegant algebra expressing the dependence of the physical bending energy of a thin metal plate on point constraints, the TPS represents a valid tool for interpolating surfaces over scattered data.

Since acquiring the true field is infeasible, it is approximated by an estimate based on a finite number of data points. The estimate can be modelled in a multitude of ways; in this work a TPS was selected. All the formulations presented in this work follow the definitions in [23].

Using a 3D-TPS interpolant the local magnetic field can be expressed in the LRS by this equation:

$$\mathbf{B}(\mathbf{P}) = \mathbf{B}_w + \mathbf{KP} + \sum_{i=1}^{nk} \mathbf{V}_i f_i(\mathbf{P}) \qquad \text{where} \qquad f_i = \|\boldsymbol{P} - \boldsymbol{P}_i\| \qquad (3)$$

where $\mathbf{B}_w$ is a 3x1 vector expressing the constant magnetic field in LSR, $\mathbf{K}$ is a 3x3 matrix which expresses a linear relationship between $\mathbf{P}$ and $\mathbf{B}(\mathbf{P})$, nk is the number of kernel points, f_i is a scalar value expressing the distance between a generic point $\mathbf{P}$ and the i-th kernel point $\mathbf{P}_i$ and $\mathbf{V}_i$ is a 3x1 vector. It can be observed that, in absence of magnetic distortion, the term $\mathbf{B}_w$ coincides with the undisturbed Earth magnetic field, expressed in LRS.

In the next sections, regarding to Equation (3), nk, $\mathbf{P}$ and $\mathbf{P}_i$ will be assumed known, while $\mathbf{B}_w$, $\mathbf{K}$, and $\mathbf{V}_i$, i=1,…, nk will be the unknown parameters to be estimated for obtaining the magnetic field map. The number and the position of the kernel points should be chosen by considering the distortion properties. The spatial sampling interval should be reduced where the magnetic field gradient is higher.

Equations (1), (2) and (3) give the final model, in the k-th frame:

$$\mathbf{m}_k = \mathbf{W}\mathbf{R}_k^{\mathrm{T}}[\mathbf{B}_w + \mathbf{K}\mathbf{P}_k + \sum_{i=1}^{nk} \mathbf{V}_i f_i(\mathbf{P}_k)] + \mathbf{O} + \mathbf{v}_k \tag{4}$$

Referring to (4), $\mathbf{m}_k$, $\mathbf{P}_k$ and $\mathbf{R}_k$ will be the input of the proposed algorithm. Specifically, $\mathbf{m}_k$ will be the magnetometer output, while $\mathbf{R}_k$ and $\mathbf{P}_k$, expressing the orientation and the position of the SRS with respect to the LRS, will be provided by an external measuring system. In this work, this is an optical motion capture system.

On the contrary, all the parameters related to the description of the magnetic distortion ($\mathbf{W}$, $\mathbf{B}_w$, $\mathbf{K}$, $\mathbf{V}_i$, $\mathbf{O}$) will be estimated.

2.2. Parameter estimation

The second original contribution of this paper is the simultaneous estimation of the parameters related to the magnetometer calibration ($\mathbf{W}$, $\mathbf{O}$) and to the TPS model ($\mathbf{B}_w$, $\mathbf{K}$, $\mathbf{V}_i$).

Since Equation (4) is still valid if the first element of $\mathbf{W}$ (w_{11}) is multiplied and $\mathbf{B}(\mathbf{P})$ is divided by the same scalar value, w_{11} has been assumed equal to 1. Applying this transformation, the number of parameters to be estimated is $23 + 3\,nk$.

Equation (4) can be re-written as follows:

$$\mathbf{m}_k = \mathbf{W}\mathbf{R}_k^{\mathrm{T}}\mathbf{M}_k\boldsymbol{\theta} + \mathbf{O} + \mathbf{v}_k = \mathbf{A}_k\boldsymbol{\theta} + \mathbf{O} + \mathbf{v}_k \tag{5}$$

where $\boldsymbol{\theta}$ is a (12+3 nk) x 1 vector containing all the parameters related to $\mathbf{B}_w$, $\mathbf{K}$ and $\mathbf{V}_i$. $\boldsymbol{M}_k$ is a 3x(12+3 nk) matrix defined according to Equation (4). In particular, $\mathbf{M}_k$, $\boldsymbol{\theta}$ and $\mathbf{A}_k$ are defined as follows:

$$\mathbf{M}_k = \begin{bmatrix} x_k\ y_k\ z_k\ 0\ 0\ 0\ 0\ 0\ 0\ f_1\ f_2 & f_{nk}\ 0\ 0 & 0\ 0\ 0 & 0 \\ \mathbf{I}_3\ 0\ 0\ 0\ x_k\ y_k\ z_k\ 0\ 0\ 0\ 0\ 0 \cdots & 0\ f_1\ f_2 \cdots f_{nk}\ 0\ 0 \cdots 0 \\ 0\ 0\ 0\ 0\ 0\ 0\ x_k\ y_k\ z_k\ 0\ 0 & 0\ 0\ 0 & 0\ f_1\ f_2 & f_{nk} \end{bmatrix}$$

$$\mathbf{A}_k = \mathbf{W}\mathbf{R}_k^{\mathrm{T}}\mathbf{M}_k \tag{6}$$

$$\boldsymbol{\theta} = \begin{bmatrix} \mathbf{B}_w \\ \mathbf{K}(1,:)^T \\ \mathbf{K}(2,:)^T \\ \mathbf{K}(3,:)^T \\ \mathbf{V}_1 \\ \mathbf{V}_2 \\ . \\ . \\ . \\ \mathbf{V}_{nk} \end{bmatrix}$$

It should be noted that, once $\mathbf{P}_k$ and $\mathbf{P}_i$ are defined, $\mathbf{M}_k$ is fully determined. So, referring to (5), the magnetometer output, once $\mathbf{W}$ defined, is linearly related to the unknown parameters $\boldsymbol{\theta}$ and $\mathbf{O}$. The least squares solution can be easily found by the pseudoinverse method [24].

The parameter estimation problem is solved using an iterative method according to the following steps:

1) Initialization: $\mathbf{P}_w = [\,w_{12}\ w_{13}\ w_{21}\ w_{22}\ w_{23}\ w_{31}\ w_{32}\ w_{33}\,]'$; where w_{ij} represent the elements of the $\mathbf{W}$ matrix and $w_{11} = 1$

2) $\mathbf{A}_k = \mathbf{W}\mathbf{R}_k^{\mathrm{T}}\mathbf{M}_k$

3) Linear least squares estimation of $\boldsymbol{\theta}$ and O through Equation (5)

4) Calculation of the 3nx8 sensitivity matrix S of the output residual vector $\mathbf{V} = [\mathbf{v}_1 \; ; \; \mathbf{v}_2 \; ; \dots . ; \; \mathbf{v}_n]$ with respect to $\mathbf{P}_w$

5) The optimal correction is calculated as $\boldsymbol{\Delta P}_w = -\text{pinv}(\boldsymbol{S}) \, \text{V}$

6) Update $\mathbf{P}_w$ ($\mathbf{P}_w = \mathbf{P}_w + \boldsymbol{\Delta P}_w$)

7) Return to 2) until the cost function $\mathbf{V}^T\mathbf{V}$ is flat or below a given threshold.

2.3. Simulated experiment

The first validation of the proposed model consists in a simulation study. This will demonstrate the validity of the proposed method under controlled data.

Referring to Equation (5), the magnetometer output was simulated, at each frame k, as a function of predefined parameters ($\mathbf{W}$, $\mathbf{O}$, $\mathbf{M}_k$, $\boldsymbol{\theta}$), position ($\mathbf{P}_k$) and orientation ($\mathbf{R}_k$). Specifically, for each test, the following parameters were defined:

- Laboratory Reference System, LRS

- Sensor Reference System, SRS. The SRS defined by the cluster of markers is assumed coincident with the magnetometer SRS

- The constant Earth's magnetic field expressed in LRS;

- Simulated calibration parameters ($\mathbf{W}$, $\mathbf{O}$) to apply to the magnetometer output

- The number and positioning of kernel points

- A set of parameters to identify the magnetic field map ($\mathbf{M}$, $\boldsymbol{\theta}$)

- The trajectory, in term of position and orientation, of the SRS with respect to LRS

The data were simulated with a sample frequency of 100 Hz. For each frame, according to Equation (5) and the defined parameters, the simulated magnetometer output was calculated. In the simulated data **W** and **0** were randomly chosen in a way that their values do not deviate too much from the values found in real acquisition. In particular, in each simulated test, a vector containing 12 elements was generated with a uniformly distributed random sequence in the interval (-0.2, 0.2). In order to create realistic calibration parameters, this vector was added to the ideal calibration parameters, corresponding to the identity matrix for **W** and null vector for **0**.

A gaussian noise, with zero mean and predefined standard deviation was added, for each simulated test, to the magnetometer output. In this way, the effect of the measurement noise on the parameter estimation was evaluated. The range of noise standard deviation varies from 0.0015 G to 0.01 G, according to magnetometer specifications [25]. This range of standard deviations was chosen to simulate noise behavior in real data acquisition. More specifically, 0.0015 Gauss corresponds to the noise standard deviation found on the real magnetometer [25] after filtering the signal with a second order bidirectional low-pass filter with cut-off frequency 5 Hz, while 0.01 Gauss represents the worst condition.

The kernel points used to model the magnetic field were uniformly distributed along the 3 axes of the laboratory reference system (LRS).

Two different classes of tests were conducted.

Class of tests 1

In the first class of tests, random rotations of the SRS with respect to the LRS exploring all possible orientations are simulated in the 3D space while the sensor is moving all around in the acquisition volume. The trajectory of the magnetometer was randomly generated in a measurement volume of 1.5x1.5x1.5 meters.

Class of tests 2

In the second class of tests 'incomplete' data acquisition is simulated. Several studies [9–11] have reported the need to explore every rotation while the magnetometer calibration procedure is performed. Otherwise, this could lead to an inaccurate calibration. Therefore, in these tests, the magnetometer explores different positions in the measurement volume (the same volume of the class of tests 1), but without exploring all the rotations. Specifically, the rotations were generated with a uniformly distributed random sequence in the intervals $(0, \pi/5)$, $(0, \pi/6)$, $(0, \pi/3)$ around x-axis, y-axis, z-axis, respectively, of the local reference system.

2.4. Real data acquisition

To validate the proposed approach using real data, a set of experiments was performed. All the data were collected in the Movement Analysis Laboratory at the University Sports Center "Record" in Bologna. An optical motion capture system (BTS SMART-DX 7000) with 10 cameras was used as a reference to obtain the position and orientation of the SRS with respect to LRS. A force plate integrated in the motion capture system was used to synchronize stereo photogrammetric data with MIMU data. Two wireless MIMUs were used to

collect inertial and magnetic data. The MIMUs were developed by NCS Lab (Carpi, Italy), integrating an accelerometer, a gyroscope and a magnetometer all on a single board. The magnetometer's datasheet can be found in [25].

The entire acquisition lasted from 2 to 3 minutes. In order to create an inhomogeneous magnetic field, the environment was filled with ferromagnetic objects, as shown in the Figure 1:
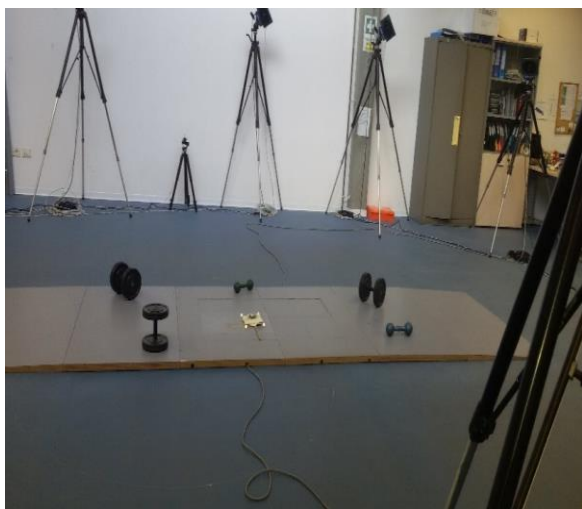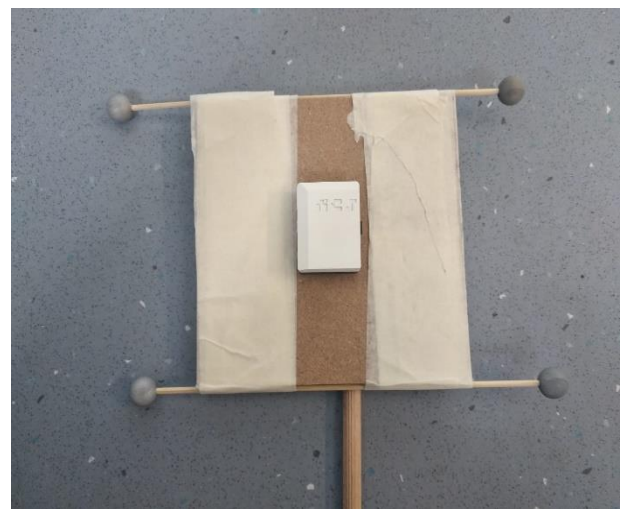
(a) (b)

Figure 1. a) The figure illustrates the acquisition volume. A force plate was positioned in the center of the volume, surrounded by different ferromagnetic objects. The acquisition volume was approximately 3x1.5x1.3 meters; b) cluster of 4 markers used for the acquisition by stereo-photogrammetry. The inertial and magnetic sensor was fixed to the cluster frame and axis alignment was done manually. All residual misalignments were included in the **W** matrix.

MIMU outputs were sampled at 120 Hz, while marker positions were estimated by stereo-photogrammetry at a 250Hz frame rate. The MIMU was fixed on a stick and moved within the measurement volume. Both at the

beginning and at the end of the acquisitions, the force plate was hit with the stick to synchronize the two signals, using peaks revealed on both force plate and accelerometer.

After the synchronization, the stereo-photogrammetric data were down-sampled at 120 Hz. Both magnetometer data and stereo-photogrammetry data were digitally filtered through a second order bidirectional Butterworth low-pass filter with 5 Hz cut-off frequency.

As for the simulated data in class of tests 1, the MIMU in the real acquisition explored the whole measurement volume (3x1.5x1.3 meters) assuming all possible orientations.

Five different acquisitions were performed, with two different MIMUs, with 2 hours interval between the two MIMUs acquisitions. In this way, it was possible to assess algorithm performance using different MIMUs and to test the magnetic distortion temporal stability.

In all the analyses performed for the reconstruction of the magnetic field, kernel points were uniformly distributed along each axis of the laboratory reference system (LRS).

2.5. Output evaluation

The performance of the proposed method was evaluated in different ways, as illustrated below:

2.5.1. *Intra-dataset magnetic field reconstruction errors*

For both simulated and real tests, after the parameter estimation, the reconstructed magnetometer output, corresponding to the right member of Equation (5), and depending on the estimated parameters, was calculated for each frame k. In this way, a comparison of the real magnetometer output ($\mathbf{m}_k$) with the reconstructed magnetometer output is possible along the three axes. Root Mean Square Errors (RMSE) along the three axes were calculated.

In order to quantify the effect of the magnetic distortion, the angle between the x-axis of the LRS (NWU convention) and the magnetic north is also computed. If no distortion is present, this angle is equal to 0 degrees, otherwise the errors in the estimation of this angle will be called 'heading errors', with a clear reference to the so-called heading angle, as defined in [9].

With regards to the simulated data, for each frame, the angle between the vector pointing to the magnetic north and the x-axis of the LRS is known for construction. Because of this, the heading error is simply calculated as the difference between the true and estimated angle. In real data, a gold standard is not available, and the heading error is defined as the difference between the angle computed from real magnetometer measure, and the angle computed from reconstructed magnetometer measure (right member of Equation (5)).

Both for simulated and real data, heading angle error was calculated in terms of RMSE and indicated as RMShE.

2.5.2. *Influence of number of kernel points and training group dimension*

Each dataset was modelled using different kernel configurations; in this way, the influence of the number and position of kernel points was evaluated.

Moreover, a training-testing procedure was implemented with the aim of investigating the number of frames necessary for the parameter estimation. In this procedure, the algorithm was trained on a predefined number of acquisition frames and the parameters estimated in the training session were tested on the remaining part of the data.

The errors mentioned above were evaluated both as a function of the number of kernel points used in the TPS model and as a function of the number of frames used for training the algorithm.

2.5.3. *Magnetic field comparison over different datasets*

Finally, in real data acquisition, a comparison of the magnetic field estimated in different dataset was performed. Let us assume that $\mathbf{B}_1(\mathbf{P})$ and $\mathbf{B}_2(\mathbf{P})$ are the magnetic field expressed in the LRS at point $\mathbf{P}$ estimated in two separate trials. In order to compare these two different results, a dataset of $\mathbf{P}_k$ was artificially created. For each $\mathbf{P}_k$, $\mathbf{B}_1(\mathbf{P}_k)$ and $\mathbf{B}_2(\mathbf{P}_k)$ were calculated. Both $\mathbf{B}_1(\mathbf{P}_k)$ and $\mathbf{B}_2(\mathbf{P}_k)$ are 3x1 vector indicating the magnetic field estimated in trial 1 and 2, respectively, at $\mathbf{P}_k$. In this way, for each frame k, a comparison of $\mathbf{B}_1(\mathbf{P}_k)$ with $\mathbf{B}_2(\mathbf{P}_k)$ is possible. In sensor-fusion algorithms for the attitude estimation using MIMUs, it is essential to know the angle on the horizontal plane between magnetic north and the x-axis of the LRS (declination angle). Because of this, this angle was calculated for each frame k, both for $\mathbf{B}_1(\mathbf{P}_k)$ and $\mathbf{B}_2(\mathbf{P}_k)$. Errors were expressed as RMSE. The results emerging from the comparison of the magnetic field estimated in different dataset have multiple meanings.

First, it allows one to analyze the temporal stability of the magnetic distortion inside the building. In fact, the different dataset used to construct to magnetic map were not acquired at the same time. The finding that the reconstructed magnetic map is very similar in all the trials could be an important point for assessing the temporal stability of magnetic distortion in the measurement volume.

Then, it offers the possibility to analyze the optimal number of kernel points for the description of the field. In fact, a large number of kernel points may not be the best option. Using a very high kernel number may produce very low intra-test errors, but the ability to generalize is lost.

3. Results

3.1. Simulated experiment

In this subsection the results emerging from simulated experiment will be presented, both from class of tests 1 and 2.

3.1.1. Intra-dataset magnetic field reconstruction errors

A comparison between the reconstructed magnetometer output and the simulated magnetometer output is presented graphically and numerically. In all the analyses conducted in this paragraph, 27 uniformly distributed kernel points were used to model the field. Results emerging from class of tests 1 are reported in Figure 2, in terms of both errors in the magnetometer reconstruction and heading errors.

The errors in the estimation of the magnetometer output and the heading angle were reported in Table 1 in terms of RMSE.
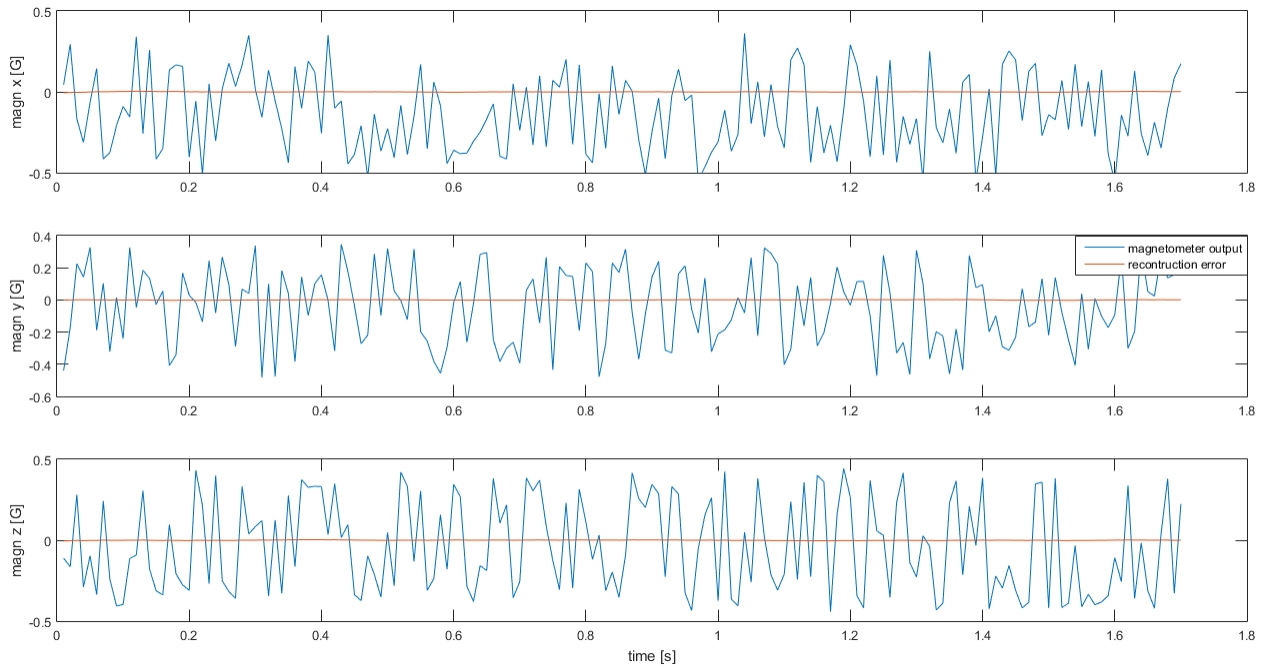
(a)
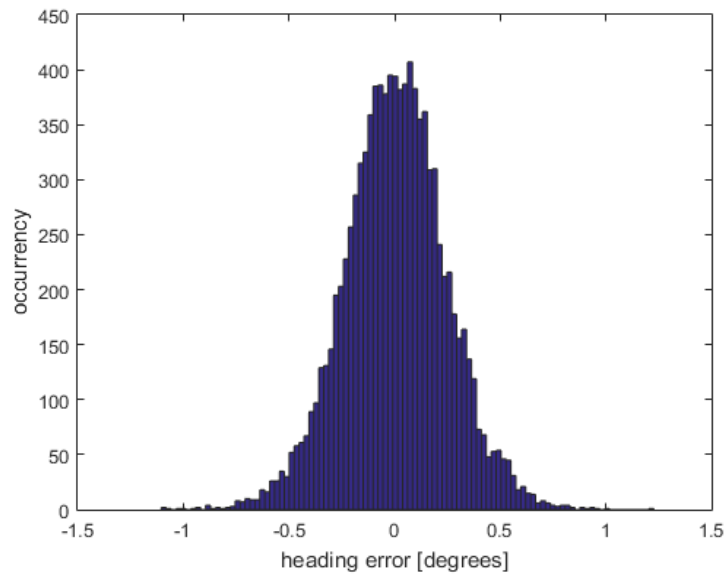
(b)

Figure 2. a) In Figure 2a the simulated magnetometer outputs and the residuals are plotted in blue and red respectively along *x, y, z*-axes. The error has the same mean and standard deviation along all the simulated experiment (120 seconds) and therefore only the first 1.7 seconds are reported here; b) histogram of the heading error.

Table 1. The Tables 1a and 1b summarize the errors along the 3 magnetometer axes and heading errors in class of tests 1 and 2, respectively. The errors were reported in terms of RMSE as a function of the standard deviation of the gaussian noise added to the simulated signals. Noise std indicates the standard deviation added to the simulated magnetometer data. RMShE indicates Root Mean Square heading Error. RMSE magn x, RMSE magn y, RMSE magn z, indicate the Root Mean Square Error along x, y, z axes, respectively, of the SRS.

	Class of tests 1			
	RMShE	RMSE magn x	RMSE magn y	RMSE magn z
Noise std = 0.0013 G	0.243°	0.0015 G	0.0015 G	0.0015 G
Noise std = 0.005 G	0.797°	0.005 G	0.005 G	0.005 G
Noise std = 0.01 G	1.595°	0.01 G	0.01 G	0.01 G
	Class of tests 2			
	RMShE	RMSE magn x	RMSE magn y	RMSE magn z
Noise std = 0.0013 G	0.339°	0.0022 G	0.0021 G	0.0023 G
Noise std = 0.005 G	1.092°	0.0051 G	0.0050 G	0.0053 G
Noise std = 0.01 G	2.178°	0.011 G	0.008 G	0.01 G

For both classes of tests, the mean error in heading estimation is almost zero. In this case, the RMSE is very close to the error standard deviation.

3.1.2. *Influence of number of kernel points and training group dimension*

The heading errors, in terms of RMSE, were evaluated as a function of both the number of kernel points used in the TPS model (Figure 3a) and of the number of frames used for training the algorithm (Figure 3b).
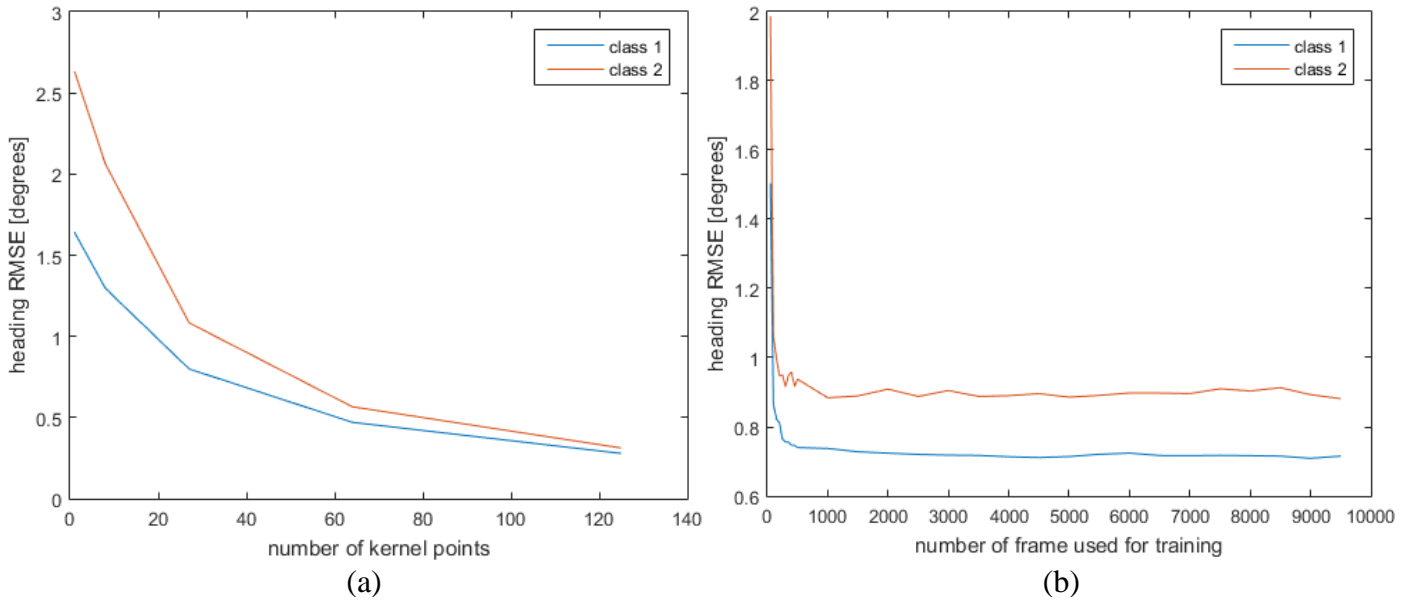
Figure 3. a) Heading RMSE as a function of the number of kernel points used to interpolate the data in the TPS model. The number of frames used for training the algorithm was 7000. B) Heading RMSE as a function of the number of frames used for training the algorithm. The number of kernel points was fixed at 27.

3.2. Real data acquisitions

In this subsection the results emerging from real data acquisitions will be presented.

3.2.1. Intra-dataset magnetic field reconstruction errors

The analysis adopted in simulated data were replicated on real data. In Figure 4a and 4b are reported, respectively, an example of a comparison between

reconstructed magnetometer output with the real magnetometer output and
the related heading error:
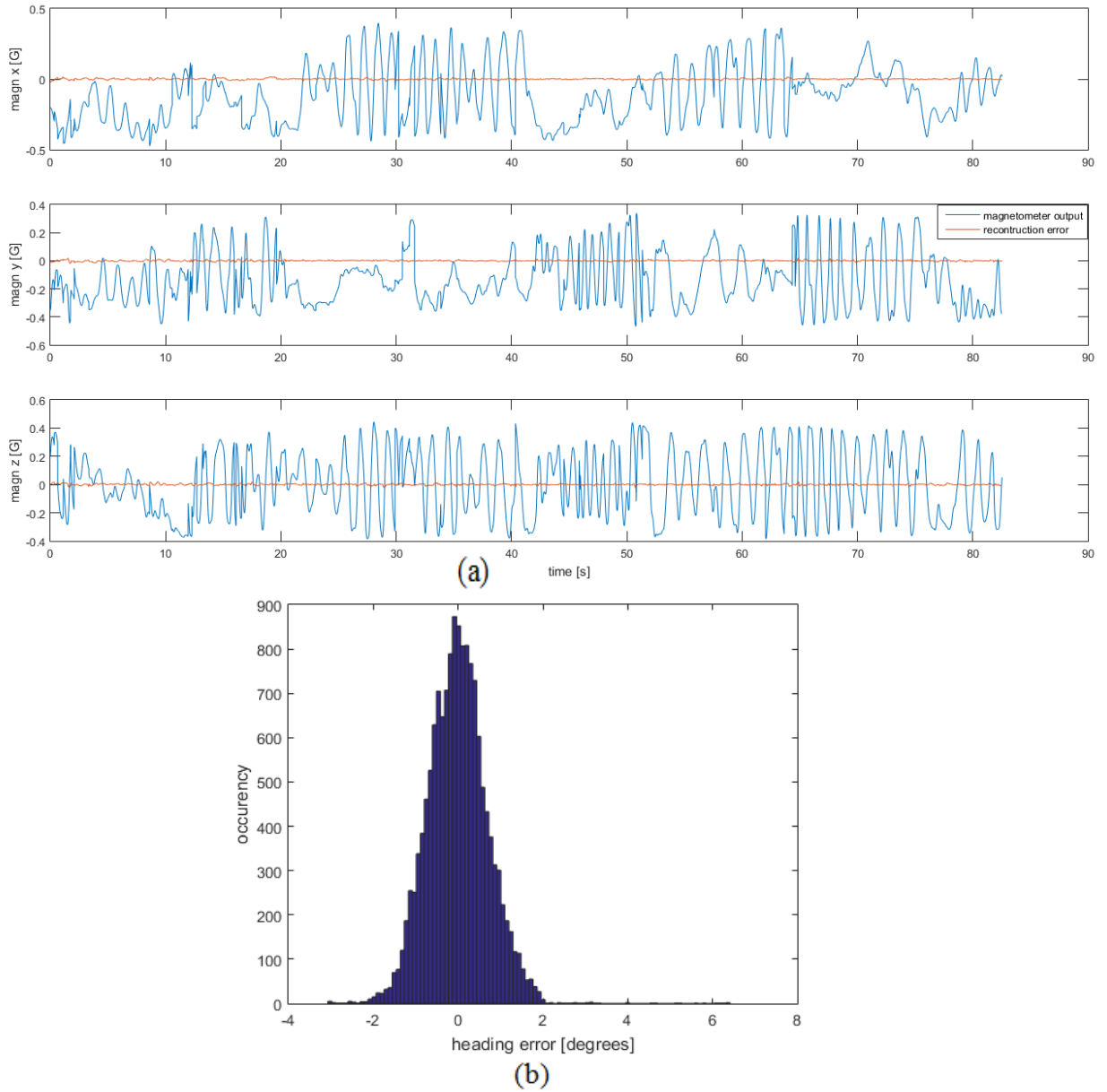
Figure 4. a) example of magnetometer outputs (blue line) and reconstruction
errors (red line) along the three local axes; b) histogram of the heading error.
The number of kernel points was fixed at 27.

The following table summarizes the errors in heading estimation for each data acquisition, as a function of the number of kernel points used to interpolate the magnetic field map:

	$nk =8$	$nk =27$	$nk =64$	$nk =125$
RMSE_MIMU1 test1 [°]	2.1	1.5	1.43	1.34
RMSE_MIMU1 test2 [°]	2.17	1.35	1.21	1.14
RMSE_MIMU1 test3 [°]	3.07	0.78	0.66	0.61
RMSE_MIMU1 test4 [°]	3.54	0.82	0.74	0.67
RMSE_MIMU1 test5 [°]	3.22	0.71	0.69	0.62
RMSE_MIMU2 test1 [°]	3.19	1.34	1.2	1.1
RMSE_MIMU2 test2 [°]	1.36	0.96	0.9	0.8
RMSE_MIMU2 test3 [°]	2.33	0.79	0.7	0.59
RMSE_MIMU2 test4 [°]	2.97	1.17	1.04	0.86
RMSE_MIMU2 test5 [°]	4.19	1.54	1.12	0.87
mean± STD [°]	2.82±0.78	1.10±0.30	0.97±0.26	0.86±0.24

Table 2. The table summarizes the errors in heading estimation for each data acquisition as a function of the number of kernel points used to interpolate the magnetic field map. The errors are expressed in term of Root Mean Square heading Errors. The first row indicates the number of kernel points used for the interpolation. Mean errors ± standard deviation are reported in the final row.

3.2.2. *Influence of number of kernel points and training group dimension*

Heading errors were evaluated as a function of both the kernel number used in the TPS model in a single acquisition and the different percentages of the frames used for model training. The heading RMSE is reported as a

function of kernel number in Figure 5a and as a function of the percentage of frames in Figure 5b.

(a)   (b)
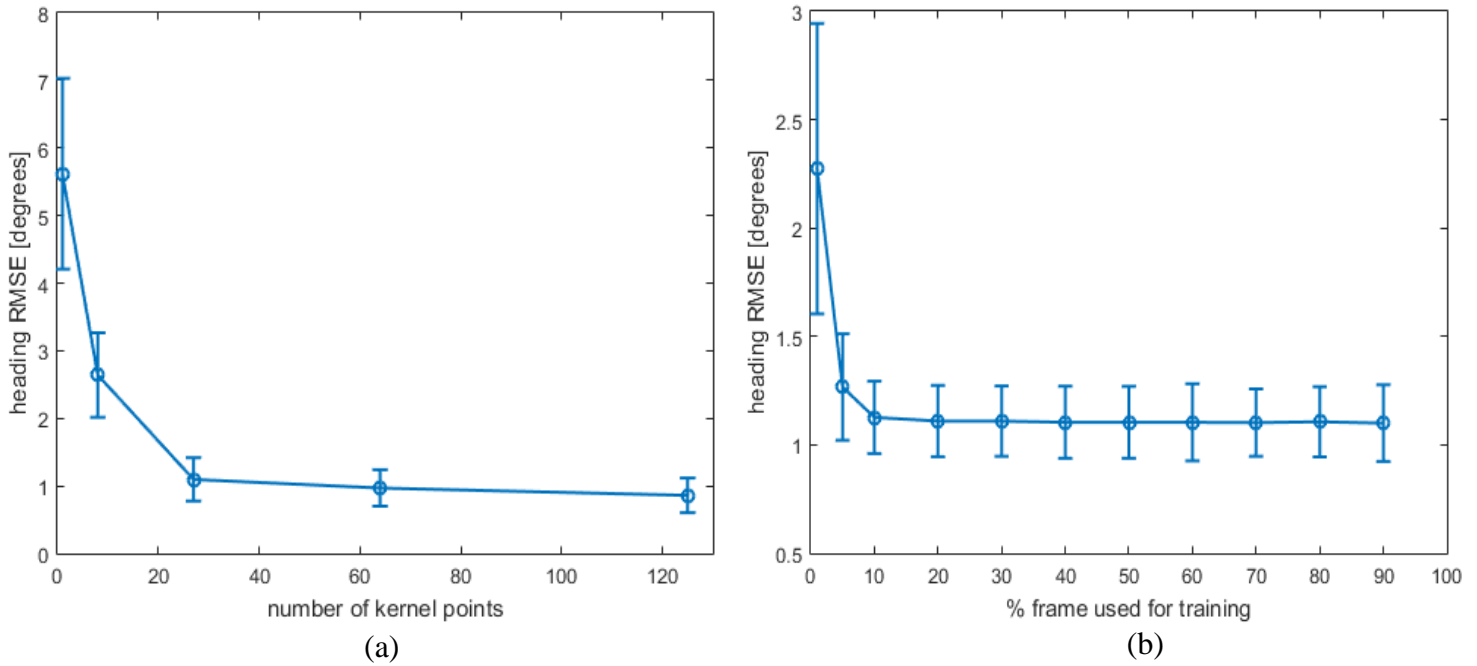
Figure 5. a) heading RMSE as a function of kernel points number. The percentage of the frames used for the model training was 75%; b) heading RMSE as a function of the percentage of frames used for the model training. The number of kernel point was fixed at 27. The observation interval in all experimental sessions varies from a minimum of 14050 to a maximum of 20460 frames, corresponding 120-180 seconds at 120 Hz sampling frequency. In figures 5a and 5b means ± standard deviations over all the real data acquisitions were reported.

3.2.3. *Magnetic field comparison over different datasets*

Finally, a comparison of the LRS magnetic field estimated in different acquisitions was performed. An example is reported in Figure 6, where two different LRS magnetic fields estimated in two different acquisitions, with different MIMUs, are compared:
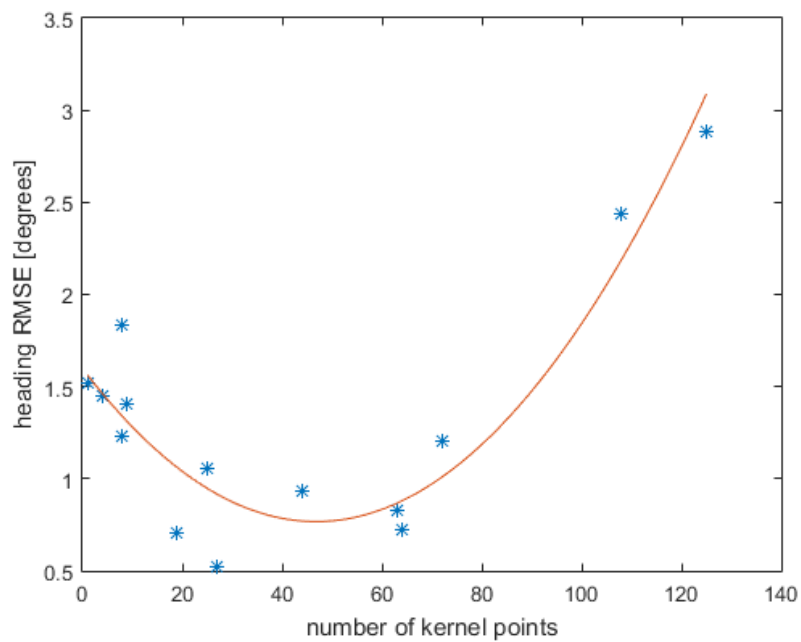
Figure 6. Heading angle RMSE between two different acquisitions as a function of the number of kernel points used in the TPS model. '*' represent the values directly obtained and the curve is a best fit parabola obtained by a least-squares method.

Figure 6 highlights that the use of many kernel points leads to an over-fitting of the field with consequent reduced generalization ability.

4. Discussion

This paper suggests a novel method based on TPS for mapping 3D magnetic distortion in an acquisition volume. Moreover, the algorithm enables the simultaneous estimation of the magnetometer calibration parameters.

Mapping the distortion of the field to obtain its component expressed in an LSR in every point of the acquisition volume could be useful in many applications, like attitude estimation in sensor-fusion algorithms [17] and indoor localization [26].

Several authors [3,5,8,12,14] proposed different methods for the environment magnetic map reconstruction. All these works are based on the use of pre-calibrated magnetometer data. This implies that at least two acquisitions must be done: one for calibrating the magnetometer data and the other for mapping the distortion in the environment. The present work overcomes this limitation by demonstrating that the simultaneous estimation of both magnetometer calibration parameters and 3D magnetic mapping is possible.

The validity of the proposed method was demonstrated using both simulated and real data.

More specifically, using simulated data, it was possible to gain a full knowledge of the noise statistical properties and to test many different parameter configurations related to the magnetometer calibration and magnetic field map. In this way it was possible to test the robustness of the algorithm in the parameters estimation in different environments only by changing the simulated magnetic distortion.

The results emerging from simulated experiments confirm that, under predefined conditions regarding data acquisition, all parameters are uniquely identifiable.

In particular, if the magnetometer explores every possible orientation while it is moving in a random way in the measurement volume, all the parameters related to the calibration (**W**, **O**) are estimated with negligible errors. This implies that the reconstructed magnetometer output is almost identical to the simulated data (Table 1). The error between them is Gaussian with null mean and standard deviation equal to the standard deviation of the noise added to the simulated data (Table 1), for all the configurations tested. Even the heading angle was estimated with excellent results (Table 1), with a standard deviation error of about 1 degree. All these results confirm the possibility to estimate, in a single procedure, all the parameters of the model shown in Equations (4-5).

The importance of exploring all the possible rotations to obtain a good accuracy in the magnetometer calibration parameters has been underlined by several authors [9,10] and it was confirmed by class of tests 2, where 'incomplete' data were simulated. Comparing the results of class of tests 1 with class of tests 2, higher errors emerged in the second tests for both calibration parameters and heading angle estimation (Table 1).

In Figure 3a the heading error is shown as a function of the number of kernel points used to describe the map. In particular, as expected, the Root Mean Square heading Error decreases as the number of kernel points increases.

Therefore, the simulated tests showed that the errors depend on different causes: i) how the acquisitions were made, ii) the noise added to the simulated

signal, iii) the number (and positioning) of kernel points used to describe the map.

In real experiments these findings were confirmed. The parameters estimation of both magnetometer calibration and magnetic field mapping in real data acquisition leads to an excellent and stable reconstruction of indoor magnetic field, with errors in the heading estimate close to 1° (Table 2). This result is comparable with the one reported in [9] where it is shown that the post-calibration residuals result in a system with heading errors in the order of 1 to 2 degrees. Comparing the accuracy reached for mapping the magnetic field with similar papers [27, 12], the results obtained are fully satisfactory. For example, in [27] it was shown that the mean heading error, after magnetic field mapping, was around 2 degrees.

The comparison of the results obtained by real and simulated data is encouraging. In fact, comparing Figure 2 and Figure 4, the magnetic field reconstruction errors show the same qualitative behavior. Errors found in real data are greater than the ones found in simulated data (Figure 2b) and 4 b)). This can be explained by different factors emerging in real data acquisitions, including: *i)* not perfect linearity of the magnetometer output with respect to the calibration parameters (referring to Equation (2)); *ii*) errors in the reconstruction of position and orientation from the data acquired by the stereo-photogrammetric system.

The temporal stability of the magnetic distortion was proved by comparing the results obtained in different acquisitions performed two hours apart (Figure 6). This result is an important confirmation of the stability of magnetic field in buildings [5].

Regarding the error in the estimation of the heading angle as a function of the number of kernels, two different behaviours have been noticed. The first one is clearly demonstrated in Figure 5a, where the RMShE is reported as a function of the kernel points number, within the same acquisition. It is shown that, with the use of a high kernel points number, the errors decrease. The second one is nicely expressed in Figure 6, in which a comparison of the heading angles estimated in two different acquisition is performed. This figure clearly illustrates that there is an optimal kernel configuration to guarantee optimum mapping. More specifically, while Figure 5a illustrates the intra-dataset magnetic field reconstruction errors, Figure 6 shows the ability to generalize the results obtained in a dataset over different datasets.

Heading errors were evaluated also as a function of the different percentages of the frame used for the training model, as reported in Figure 3b for simulated data and in Figure 5b for real data. A training-testing procedure was implemented to understand the predictive capabilities of the model. To this end, the model was trained on a predefined number of frames, and the parameter estimated were tested on the remaining frames. Results indicate that is not necessary to use every available frame in the analysis, because, as it can be seen in Figure 5, the error remains constant for percentages greater than 10%. This percentage depends both on the distortion properties and on the way in which the data are collected.

One limitation of this study may be the acquisition volume size. All the real data were acquired in a volume of 3x1.5x1.3 meters. Further studies may include a bigger acquisition volume. In that case, the number of kernel points should probably be increased to achieve the same degree of accuracy found in

this work. Another point to underline is that the proposed algorithm is based on the assumption of a time-invariant magnetic field (3) during data acquisition. If the hypothesis is not verified, Equations (3) and (4) should include terms that vary with time in a known way.

Future developments of the present work will address the study of the number and positioning of kernel points, in relation to the magnetic distortions present in the acquisition volume. When the field is almost constant, no kernel points are required to model it, Likewise, in presence of high magnetic distortion, a greater number of kernel points will be needed. Furthermore, within the the measurement volume, some regions could be heterogeneous and others could be homogeneous. In this case it would be appropriate to choose not only the number of kernels, but also their position. In fact, the number and position of the kernel points should be chosen by taking into account the distortion properties. The spatial sampling interval should be reduced where the magnetic field gradient is higher. Automated algorithm to find the optimal number and positioning of kernel points might be the subject of a future study.

References

1. Mora, C.V.; Davison, M.; Wild, J.M.; Walker, M.M. Magnetoreception and its trigeminal mediation in the homing pigeon. Nature 2004, 432, 508–511, doi:10.1038/nature03077.

2. Kisliuk, M.; Ishay, J. Influence of an additional magnetic field on hornet nest architecture. Experientia 1977, 33, 885–887, doi:10.1007/BF01951261.

3. Haverinen, J.; Kemppainen, A. Global indoor self-localization based on the ambient magnetic field. Robot. Auton. Syst. 2009, 57, 1028–1035, doi:10.1016/j.robot.2009.07.018.

4. Vallivaara, I.; Haverinen, J.; Kemppainen, A.; Röning, J. Magnetic field-based SLAM method for solving the localization problem in mobile robot floor-cleaning task. In 2011 15th International Conference on Advanced Robotics (ICAR); 2011; pp. 198–203.

5. Frassl, M.; Angermann, M.; Lichtenstern, M.; Robertson, P.; Julian, B.J.; Doniec, M. Magnetic maps of indoor environments for precise localization of legged and non-legged locomotion. In 2013 IEEE/RSJ International Conference on Intelligent Robots and Systems; 2013; pp. 913–920.

6. Sabatini, A.M. Estimating three-dimensional orientation of human body parts by inertial/magnetic sensing. Sensors 2011, 11, 1489–1525, doi:10.3390/s110201489.

7. de Vries, W.H.K.; Veeger, H.E.J.; Baten, C.T.M.; van der Helm, F.C.T. Magnetic distortion in motion labs, implications for validating inertial magnetic sensors. Gait Posture 2009, 29, 535–541, doi:10.1016/j.gaitpost.2008.12.004.

8. Vallivaara, I.; Haverinen, J.; Kemppainen, A.; Röning, J. Simultaneous localization and mapping using ambient magnetic field. In 2010 IEEE Conference on Multisensor Fusion and Integration; 2010; pp. 14–19.

9. Gebre-Egziabher, D.; Elkaim, G.H.; Powell, J.D.; Parkinson, B.W. Calibration of Strapdown Magnetometers in the Magnetic Field Domain. In; 2004.

10.   Renaudin, V.; Afzal, M.H.; Lachapelle, G. Complete Triaxis Magnetometer Calibration in the Magnetic Domain. J Sens. 2010, 2010, 967245–967245, doi:10.1155/2010/967245.

11.   Secer, G.; Barshan, B. Improvements in deterministic error modeling and calibration of inertial sensors and magnetometers. Sens. Actuators Phys. 2016, 247, 522–538, doi:10.1016/j.sna.2016.06.024.

12.   Solin, A.; Kok, M.; Wahlström, N.; Schön, T.B.; Särkkä, S. Modeling and interpolation of the ambient magnetic field by Gaussian processes. ArXiv150904634 Cs Stat 2015.

13.   Storms, W.; Shockley, J.; Raquet, J. Magnetic field navigation in an indoor environment. In 2010 Ubiquitous Positioning Indoor Navigation and Location Based Service; 2010; pp. 1–10.

14.   Grand, E.L.; Thrun, S. 3-Axis magnetic field mapping and fusion for indoor localization. 2012 IEEE Int. Conf. Multisens. Fusion Integr. Intell. Syst. MFI 2012, 358–364, doi:10.1109/MFI.2012.6343024.

15.   Mangia, A.L.; Cortesi, M.; Fantozzi, S.; Giovanardi, A.; Borra, D.; Gatta, G. The Use of IMMUs in a Water Environment: Instrument Validation and Application of 3D Multi-Body Kinematic Analysis in Medicine and Sport. Sensors 2017, 17, doi:10.3390/s17040927.

16.   Palermo, E.; Rossi, S.; Marini, F.; Patanè, F.; Cappa, P. Experimental evaluation of accuracy and repeatability of a novel body-to-sensor calibration procedure for inertial sensor-based gait analysis. Measurement 2014, 52, 145–155, doi:10.1016/j.measurement.2014.03.004.

17.   Roetenberg, D.; Luinge, H.J.; Baten, C.; Veltink, P.H. Compensation of magnetic disturbances improves inertial and magnetic sensing of human body segment orientation. IEEE Trans. Neural Syst. Rehabil. Eng. 2005, 13, 395–405.

18.   Torres-Sospedra, J.; Montoliu, R.; Mendoza-Silva, G.M.; Belmonte, O.; Rambla, D.; Huerta, J. Providing Databases for Different Indoor Positioning Technologies:

Pros and Cons of Magnetic Field and Wi-Fi Based Positioning. Mob. Inf. Syst. 2016, 2016, 6092618–6092618, doi:10.1155/2016/6092618.

19.   Ferris, B.; Fox, D.; Lawrence, N.D. WiFi-SLAM Using Gaussian Process Latent Variable Models. In IJCAI; 2007.

20.   Shu, Y.; Bo, C.; Shen, G.; Zhao, C.; Li, L.; Zhao, F. Magicol: Indoor Localization Using Pervasive Magnetic Field and Opportunistic WiFi Sensing. IEEE J. Sel. Areas Commun. 2015, 33, 1443–1457, doi:10.1109/JSAC.2015.2430274.

21.   Barkby, S.; Williams, S.B.; Pizarro, O.; Jakuba, M.V. A featureless approach to efficient bathymetric SLAM using distributed particle mapping. J Field Robot. 2011, 28, 19–39, doi:10.1002/rob.20382.

22.   Madgwick, S.O.H. Automated calibration of an accelerometers, magnetometers and gyroscopes-A feasibility study. In; 2011.

23.   Bookstein F. Principal Warps: Thin Plate Splines and the decomposition of deformations. IEEE Transactions on pattern analysis and machine intelligence; 1989, Vol. 11, No. 6

24.   Draper, N.R.; Smith, H. Fitting a Straight Line by Least Squares. In Applied Regression Analysis; John Wiley & Sons, Ltd, 2014; pp. 15–46 ISBN 978-1-118-62559-0.

25.   MEMSIC, Inc - Magnetic Sensor Components | MMC3416xPJ Available online: http://www.memsic.com/magnetic-sensors/MMC3416xPJ (accessed on Nov 12, 2018).

26.   Cadena, C.; Carlone, L.; Carrillo, H.; Latif, Y.; Scaramuzza, D.; Neira, J.; Reid, I.; Leonard, J.J. Past, Present, and Future of Simultaneous Localization And Mapping: Towards the Robust-Perception Age. IEEE Trans. Robot. 2016, 32, 1309–1332, doi:10.1109/TRO.2016.2624754.

27. Kim, H.-S.; Seo, W.; Baek, K.-R. Indoor Positioning System Using Magnetic Field Map Navigation and an   Encoder System. Sensors 2017, 17, 651.

Chapter 3

Simultaneous calibration of triaxial accelerometer and magnetometer without external references[1]

Abstract:

A non-optimal sensor calibration of inertial and magnetic sensors leads to inaccurate values of both raw data and attitude estimation downstream of the sensor fusion algorithms. It is therefore essential to develop a simple and effective procedure for data calibration that can be easily performed from the end user without the need of external equipment. Many algorithms for calibrating independently the inertial and magnetic sensors without the need of external equipment were proposed, but most of these are focused on the estimate on the calibration parameters of the single sensor, and do not consider the misalignments between the local system of references.

Due to this fact, the aim of this work is to provide a simple and effective algorithm for simultaneous calibration of triaxial magnetometer and accelerometer, without external references, and considering the misalignments of the local system of references. The proposed method allows to estimate also the direction of the local magnetic field, which may be unknown and is essential for attitude estimation using magnetometers.

The algorithm was tested on both simulated and real data. The simulated experiments demonstrated the validity of the proposed method under controlled data and allowed comparison between the estimates and the ground truth. The real data acquisition showed good results in calibration procedure that lead to low errors in 3D attitude estimation, compared to the stereo photogrammetry, assumed as gold standard.

1. Introduction

Magnetic and Inertial Measurement Units (MIMU) are an emerging technology that can be used to obtain 3D orientation of the body on which they are fixed. The problem of an accurate tracking of the orientation of rigid objects is important in several domains, including: aerospace [1], robotics [2], navigation [3] and human motion analysis [4], which may include a range of interesting applications, from monitoring of activities of daily living to virtual/augmented reality.

A MIMU usually includes an accelerometer, a gyroscope and a magnetometer [5]. In order to measure in three dimensions, tri-axis sensors consisting of 3 mutually orthogonal sensitive axes are required. Accelerometers and gyroscopes measure linear acceleration and angular velocity along and about a so-called "sensitive axis", respectively. Magnetometer measures the components of the local magnetic field along the three mutually orthogonal axes of its Sensor Reference System (SRS).

The data from accelerometer and gyroscope can provide useful kinematic quantities that are generally computed as the time-derivative of the measured linear and angular displacement (usually acquired with stereo photogrammetry) [6]. The combination of these data with the magnetometer allows to obtain 3D orientation using dedicated sensor-fusion algorithms [7–9].

One of the most important points that favors their use is that they can be used anywhere, without the restrictions imposed by the placement of cameras or external sources in a dedicated laboratory.

However, the measuring accuracies of MIMU in the 3D attitude estimate are still largely inferior to other sensing approaches that need the availability of external sources, e.g., cameras for optical trackers, ultrasonic/electromagnetic transmitters for acoustic/electromagnetic trackers [7].

If we exclude hardware developments, two main factors can be worked on to improve the accuracy of MIMUs: sensor-fusion algorithm and sensors' calibration.

The most commonly used sensor fusion algorithms used for estimating 3D orientation starting from MIMU data are Extended Kalman filter (EKF) and complementary filter [10]. In recent years a lot of different algorithms were developed [4,7,9,11] showing encouraging results if the data are correctly calibrated.

An incorrect sensor calibration leads to inaccurate values of both raw data and attitude estimation downstream of the sensor fusion algorithms.

Accelerometer and magnetometer are usually calibrated using Earth's gravitational or magnetic field as reference [12–14]. Most research into calibration of these devices focuses on magnetometer calibration, which can also be used to calibrate accelerometers in stationary settings [15].

More specifically, a common approach to calibration is to assume that the magnetic field's norm (or gravitational field's norm) is known or unitary, and then adjust the gain and bias so that the readings match this value [12–14]. Starting from that assumption different validated algorithm were developed, showing excellent results for magnetometer calibration [12–14]. This whole

category of algorithms is often used because it does not require external mechanisms, simplifying the data acquisition procedure.

Other calibration methods use actuated mechanical systems to position the MIMU in known orientations and rotate at known and/or constant rotation rates [16,17]. These methods offer a robust and accurate solution but are difficult to use on a large scale due to the need for the presence of machinery dedicated to calibration which is often very expensive.

Although both classes of methods can be used to calibrate accelerometers as well as magnetometers, the calibration must be performed independently, so the magnetometer and accelerometer are calibrated in different frames, and the rotation between them is unknown.

Furthermore, neither method is able to estimate the direction of the magnetic field, which may be unknown and is essential for attitude estimation using magnetometers [7,12].

In [18] the authors tried to solve both problems by simultaneously calibrating the magnetometer and accelerometer, allowing the magnetic field, the attitude, and all the sensors' parameters to be estimated. This eliminates the need for a reference so that the calibration can be performed from sensor readings alone, that is, no external apparatus or knowledge besides the sensor readings is required. However, the problem is replete with low- quality local minima, which sometimes significantly degrade the calibration performance, and the solution has a very high computational cost, making the algorithm impractically slow.

The aim of this work is to provide a simple and effective algorithm for simultaneous calibration of magnetometer and accelerometer, without external references.

To our knowledge, the algorithms described in the present work and in [18] are the only accelerometer and magnetometer calibration algorithms that can perform the complete calibration from collected data alone.

The algorithm was tested on both simulated and real data. The simulated experiments demonstrated the validity of the proposed method under controlled data and allowed comparison between the estimates and the ground truth. The real data acquisition showed good results in calibration procedure that lead to low errors in 3D attitude estimation, compared to the stereo photogrammetry, assumed as gold standard.

2. Materials and Methods

2.1 Model of triaxial magnetometer and accelerometer

Three right-handed orthogonal reference systems are defined: a Laboratory Reference System (LRS), supposed fixed with the Earth, an Accelerometer Reference System (ARS), solidal with the accelerometer included in the MIMU and a Magnetometer Reference System (MRS), solidal with the magnetometer. Without loss of generality, in this paper the system of reference of the MIMU is supposed coincident with ARS.

The LRS is defined with the Nord-West-Up (NWU) convention, in which the x, y and z axes point, respectively, to the magnetic north, magnetic west

and upward [7]. The mentioned convention offers the possibility to build a LRS without any external reference, except for the gravity and magnetic field; for this reason, it is the most used one.

If we suppose that there are no magnetic distortions, the magnetic field in a generic point P (x, y, z) correspond to the Earth's magnetic field. Moreover, in absence of linear acceleration, the accelerometer measure only the projection of gravitational field on its axes. For these reasons an ideal triaxial magnetometer and an ideal triaxial accelerometer measure the components along their three mutually orthogonal axes of, respectively, the Earth's magnetic field and the gravitational field (named $\mathbf{B}_0$ and $\mathbf{G}$, respectively).

The ideal sensors-measured magnetic and gravitational field at the instant of time (called also frame) k are given by:

$$\mathbf{m}_k^{\mathrm{I}} = \mathbf{R}_{m,k}^{\mathrm{T}} \, \mathbf{B}_0 = \mathbf{R}_{m,k}^{\mathrm{T}} \begin{bmatrix} bx \\ 0 \\ bz \end{bmatrix} \tag{1}$$

$$\mathbf{a}_k^{\mathrm{I}} = \mathbf{R}_{a,k}^{\mathrm{T}} \, \mathbf{G} = \mathbf{R}_{a,k}^{\mathrm{T}} \begin{bmatrix} 0 \\ 0 \\ g \end{bmatrix}$$

where $\mathbf{R}_{m,k}^{\mathrm{T}}$ and $\mathbf{R}_{a,k}^{\mathrm{T}}$ are the time-varying orientation matrix of the ARS and MRS with respect to the LRS, respectively and $\mathbf{m}_k^{\mathrm{I}}$ and $\mathbf{a}_k^{\mathrm{I}}$ are the magnetometer and accelerometer ideal output. $\mathbf{B}_0$ and $\mathbf{G}$ are expressed in LRS and their components along the LRS axis are called bx, bz and g, where g represents the gravitational acceleration. Note that the second component of $\mathbf{B}_0$ is assumed null due to the definition of LRS with the Nord-West-Up (NWU) convention.

Under actual conditions we must consider two source of errors: instrumentation errors and magnetic deviation [19,20]. The first one includes:

i) cross-talk effects due to non-orthogonal measurement axes, ii) non-unitary and generally different gains along the three axes, iii) offset and iv) additive noise. The latter includes v) soft iron and vi) hard iron effects. These can be accounted by using a simple linearized model [13], expressed at frame k:

$$\mathbf{m}_k^I = \mathbf{W}_m \mathbf{m}_k + \mathbf{O}_m + \mathbf{v}_{m,k} \qquad (2)$$
$$\mathbf{a}_k^I = \mathbf{W}_a \mathbf{a}_k + \mathbf{O}_a + \mathbf{v}_{a,k}$$

where $\mathbf{m}_k$ is the actual measured magnetic field, $\mathbf{a}_k$ is the accelerometer output, $\mathbf{W}_m$ and $\mathbf{W}_a$ are 3x3 matrix depending on i), ii) v), $\mathbf{O}_m$ and $\mathbf{O}_a$ a 3x1 bias vector depending on iii) and vi), and $\mathbf{v}_{m,k}$ and $\mathbf{v}_{a,k}$ the additive noise, for magnetometer and accelerometer respectively.

For magnetometer and accelerometer calibration, $\mathbf{W}_m$, $\mathbf{W}_a$, $\mathbf{O}_m$ and $\mathbf{O}_a$ must be estimated. Several studies have proposed different methods to estimate the optimal calibration parameters [12,13,19,21], but without considering the rotation between ARS and MRS. In the presented method this limitation is overcome using a simple mathematical consideration and the right polar decomposition.

In [22] the right polar decomposition was demonstrated and defined as follow: 'The right polar decomposition of a matrix A ∈ ℂ m x n (m≥ n) has the form A = UP where U ∈ ℂ m x n is a matrix with orthonormal columns and P ∈ ℂ m x n is positive semi-definite'.

Following the previous definition, and keeping in mind that $\mathbf{R}_{a,k}^T$ can be expressed as the generic product of two rotations matrix, $\mathbf{R}_{a,k}^T$, $\mathbf{W}_a$, and $\mathbf{O}_a$ can be expressed as reported in equation (3):

$$\mathbf{W}_a = \mathbf{\Delta R}\ \mathbf{W}_a^1 \qquad (3)$$

$$\mathbf{O}_a = \mathbf{\Delta R}\ \mathbf{O}_a^1$$

$$\mathbf{R}_{a,k}^T = \mathbf{\Delta R}\ \mathbf{R}_{a,k}^{1,T}$$

Where $\mathbf{\Delta R}$ is a rotation matrix and $\mathbf{W}_a^1$ is a symmetric positive semi-definite matrix.

Combining equations (1), (2) and (3), we obtain:

$$\mathbf{\Delta R}\ \mathbf{W}_a^1\ \mathbf{a}_k + \mathbf{\Delta R}\ \mathbf{O}_a^1 = \mathbf{\Delta R}\ \mathbf{R}_{a,k}^{1,T}\ \mathbf{G} \qquad (4)$$

And subsequently:

$$\mathbf{W}_a^1\ \mathbf{a}_k + \mathbf{O}_a^1 = \mathbf{R}_{a,k}^{1,T}\ \mathbf{G} \qquad (5)$$

Regarding equation (5), the parameters to be estimated for the accelerometer calibration are 6 for matrix $\mathbf{W}_a^1$ and 3 for vector $\mathbf{O}_a^1$. Note that the assumption that the system of reference of the MIMU coincides with ARS has allowed us to save the estimate of 3 parameters of the $\mathbf{W}_a$ matrix.

No assumption was done regarding the orientation of MRS. Due to this fact, all the parameters of the $\mathbf{W}_m$ matrix must be estimated; these parameters include also the residual misalignments between MRS and ARS. As reported in [20], without loss of generality, the first element of $\mathbf{W}_m$ was fixed to 1.

The final equations that describe the model used in this paper for describing the accelerometer and magnetometer output is reported:

$$\mathbf{W}_a^1\, \mathbf{a}_k + \mathbf{O}_a^1 = \mathbf{R}_k^{\mathrm{T}}\, \mathbf{G} \qquad\qquad (6)$$

$$\mathbf{W}_m\, \mathbf{m}_k + \mathbf{O}_m = \mathbf{R}_k^{\mathrm{T}}\, \mathbf{B}_0$$

Where $\mathbf{R}_k^{\mathrm{T}}$ coincides with $\mathbf{R}_{a,k}^{1,\mathrm{T}}$. In equation (6), $\mathbf{a}_k$ and $\mathbf{m}_k$ represents the sensors outputs for each frame, which are known in the process of calibration, like the Earth gravitational field expressed in LRS ($\mathbf{G}$). The remaining parameters need to be estimated by the calibration algorithm, including the Earth magnetic field expressed in LRS ($\mathbf{B}_0$).

In the proposed work, 22 parameters are estimated for simultaneous calibration of accelerometer and magnetometer. More specifically, $\mathbf{W}_a^1$ is composed by 6 independent parameters, $\mathbf{O}_a^1$ by 3, $\mathbf{W}_m$ by 8, $\mathbf{O}_m$ by 3, and $\mathbf{B}_0$ by 2. In this way it is possible to estimate not only the classical calibration parameters for accelerometer and magnetometer, but also the residual misalignments between ARS and MRS and the Earth magnetic field expressed in LRS.

2.2. Parameter Estimation

An original contribution of this paper is the simultaneous estimation of the parameters related to the magnetometer calibration ($\mathbf{W}_m$, $\mathbf{O}_m$), the accelerometer calibration ($\mathbf{W}_a^1$, $\mathbf{O}_a^1$) and the components of the Earth magnetic field expressed in LRS ($\mathbf{B}_0$). Moreover, the matrix $\mathbf{W}_m$ contains the misalignments of MRS to ARS, allowing to rotate the magnetometer output in the ARS.

For solving the problem of calibration parameters estimation, it is necessary to solve the so-called Wahba's problem [23], which is a constrained least-squares optimization problem for finding the rotation matrix from vector measurements taken at a single time (single-frame method). In this case, the Wahba's problem can be formulated as follow: starting from Equation (1), which is the best estimate of $\mathbf{R}_k^T$, assuming known $\mathbf{m}_k^l$, $\boldsymbol{a}_k^l$, $\mathbf{B}_0$ and $\mathbf{G}$ and assuming ARS coincident with MRS?

The algorithm proposed in [24] was used for solving the proposed problem. It is based on computing the singular value decomposition (SVD) of a matrix [25] and was included in the proposed algorithm for the optimal estimate of $\mathbf{R}_k^T$.

The parameter estimation problem is solved using an iterative method according to the following steps:

 1) Initialization of the parameters to be estimated:

$\theta =$

$[w_{m,12}\ \ w_{m.13}\ w_{m21}\ w_{m,22}\ w_{m,23}\ w_{m,31}\ w_{m,32}\ w_{m,33}\ \ o_{m,1}\ o_{m,2}\ o_{m,3}\ b_x\ b_z\ w_{a,11}\ \ ...$

$w_{a,12}\ w_{a,13}\ w_{a,22}\ w_{a,23}\ w_{a,33}\ o_{a,1}\ o_{a,2}\ o_{a,3}$]'; where $w_{m,ij}$ represent the elements of the $\mathbf{W_m}$ matrix, $o_{m,1}\ o_{m,2}\ o_{m,3}$ represent the elements of $\mathbf{O_m}$, $w_{a,ij}$ represent the elements of the $\mathbf{W_a^1}$ matrix, $o_{a,1}\ o_{a,2}\ o_{a,3}$ represent the elements of $\mathbf{O_a^1}$ and $b_x\ b_z$ represent the elements of $\mathbf{B_0}$

2)   Estimation of $\mathbf{R}_k^\mathrm{T}$ from Equation (6) using the algorithm proposed in [24]

3)   Calculation of the 22 × 6n sensitivity matrix S of the output residual vector with respect to θ

4)   The optimal correction to θ is calculated as reported in [26]

5)   Return to 2) until the cost function is flat or below a given threshold.

2.3. Simulated Experiment

The simulated experiments aimed to demonstrate the validity of the proposed method under controlled data. Moreover, the use of simulated data allows a direct comparison between the estimates and the ground truth.

Referring to Equation (6), both magnetometer and accelerometer data were simulated at each frame k, as a function of predefined parameters ($\mathbf{W_m}$, $\mathbf{O_m W_a^1}$, $\mathbf{O_a^1}$, $\mathbf{B_0}$) and orientation ($\mathbf{R}_k$). Specifically, for each test, the following parameters were defined:

1) Laboratory Reference System, LRS

2) Accelerometer and Magnetometer Reference Systems, ARS and MRS.

3) The constant Earth's magnetic field expressed in LRS, $\mathbf{B_0}$

4) Simulated calibration parameters ($\mathbf{W_m}$, $\mathbf{O_m W_a^1}$, $\mathbf{O_a^1}$) to apply to the magnetometer and accelerometer output

5) The orientation of ARS and MRS with respect to LRS

The data were simulated with a sample frequency of 100 Hz. For each frame, according to Equation (6) and the defined parameters, the simulated output were calculated. In the simulated data $\mathbf{W}_m$, $\mathbf{O}_m\mathbf{W}_a^1$, $\mathbf{O}_a^1$ were randomly chosen in a way that their values do not deviate too much from the values found in real acquisition. With this aim, a random vector (generated with a uniformly distributed random sequence in the interval (−0.2, 0.2)) was added to the ideal calibration parameters, corresponding to the identity matrix for $\mathbf{W}$ and null vector for $\mathbf{O}$.

A gaussian noise, with zero mean and predefined standard deviation was added, for each simulated test, to the magnetometer and accelerometer output. In this way, the effect of the measurement noise on the parameter estimation was evaluated. The range of magnetometer noise standard deviation varies from 0.2 mG to 20 mG, according to magnetometer specifications [27]. The range of accelerometer noise standard deviation varies from 0.1 mg to 10 mg, according to accelerometer specifications [28].

This range of standard deviations was chosen to simulate noise behavior in real data acquisition.

Random rotations of the ARS and MRS with respect to the LRS exploring all possible orientations are simulated in the 3D space [20].

The performance of the proposed method on simulated data was evaluated comparing the calibration parameters estimated with the real calibration parameters. This comparison is possible only when using simulated data. The errors are reported as the difference between the calibration parameters estimated and the real calibration parameters.

2.4. Real Data Acquisition

To validate the proposed approach using real data, a set of experiments was performed. All the data were collected in the Movement Analysis Laboratory at the University Sports Center "Record" in Bologna. An optical motion capture system (BTS SMART-DX 7000) with 10 cameras was used as a reference to obtain the position and orientation of the ARS with respect to LRS. A force plate integrated in the motion capture system was used to synchronize stereo photogrammetric data with MIMU data. Two wireless MIMUs (NCS Lab, Carpi, Italy) were used to collect inertial and magnetic data. The MIMUs were developed by NCS Lab (Carpi, Italy), integrating an accelerometer [28], a gyroscope [29] and a magnetometer [27] all on a single board. Each acquisition lasted from 2 to 3 min.

MIMU outputs were sampled at 100 Hz, while marker positions were estimated by stereo-photogrammetry at a 250 Hz frame rate. The MIMU was fixed on a stick, as illustrated in Figure 1, and moved within the measurement volume.
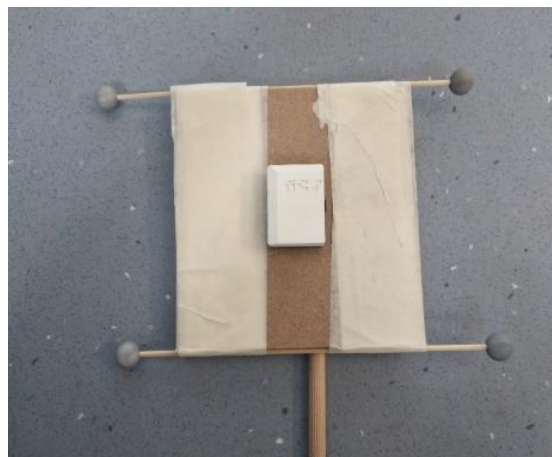
Figure 1. Cluster of four markers used for the acquisition by stereo-photogrammetry. The inertial and magnetic sensor was fixed to the cluster frame and axis alignment was done manually.

Both at the beginning and at the end of the acquisitions, the force plate was hit with the stick to synchronize the two signals, using peaks revealed on both force plate and accelerometer. After the synchronization, the stereo-photogrammetric data were down-sampled at 100 Hz. Both MIMU data and stereo-photogrammetry data were digitally filtered through a second order bidirectional Butterworth low-pass filter with 5 Hz cut-off frequency.

The MIMU explored all possible orientations, trying not to change the position of the sensor's center of gravity. Ten different acquisitions were performed, with two different MIMUs. In this way, it was possible to assess algorithm performance using different MIMUs.

The performance of the proposed method on real data can not be evaluated in a direct way as for the simulated data, because the real calibration parameters are unknown. The first indirect way for assessing the quality of the parameter estimated is to evaluate if the norm of the calibrated magnetometer during the acquisition is constant around the Earth magnetic field.

The second way is to compare the rotation matrix $\mathbf{R}_k$ (Equation 6) obtained from MIMU with the same matrix obtained with stereo-photogrammetry, that can be considered the gold standard. Starting from calibrated MIMU data, $\mathbf{R}_k$ was calculated for each frame with the algorithm proposed in [9]. The more $\mathbf{R}_k$ estimated from MIMU data is similar to $\mathbf{R}_k$ estimated from stereo-photogrammetry, the more the calibration took place correctly. For evaluating

the similarity between the two matrices, the orientation matrix $\mathbf{R}_{err,k}$ was defined for each frame as follow:

$$\mathbf{R}_{err,k} = \mathbf{R}_{cluster,k} * \mathbf{R}_{MIMU,k}^{\mathrm{T}} \qquad (7)$$

Where $\mathbf{R}_{cluster,k}$ represents the orientation matrix $\mathbf{R}_k$ estimated from stereo-photogrammetry, and $\mathbf{R}_{MIMU,k}^{\mathrm{T}}$ represents the orientation matrix $\mathbf{R}_k$ estimated from MIMU.

$\mathbf{R}_{err,k}$ was decomposed using the ZYX Euler convention and the errors in yaw, pitch and roll were estimated for each frame. Root Mean Square Errors of yaw, pitch and roll (RMSE) were calculated along each real acquisition.

3. Results

In the following subsections the results emerging from both simulated and real experiments will be presented.

3.1. Simulated Experiment

As a first representation of the changing in the calibrated accelerometer and magnetometer output, raw and calibrated data are plotted in Figure 2 as a 3D graph:
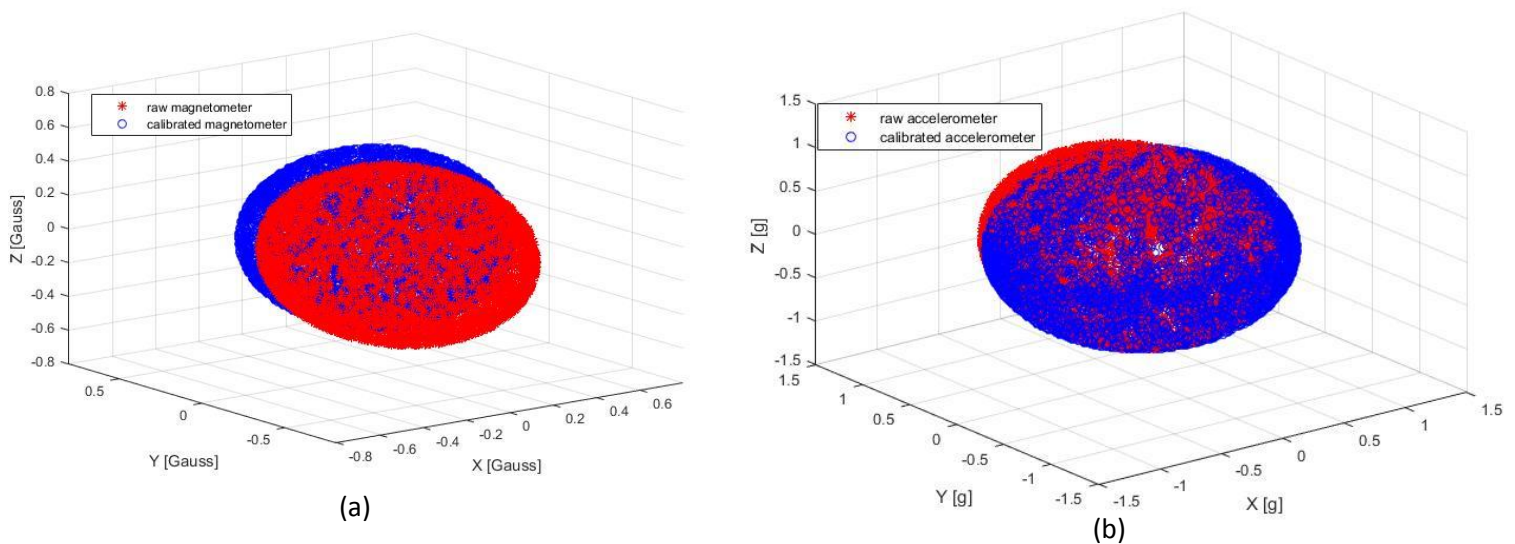
Figure 2. (**a**) Raw and calibrated magnetic field measurements are plotted in a 3D graphs in red and blue, respectively. (b) Raw and calibrated accelerometer measurements are plotted in a 3D graphs in red and blue, respectively.

For assessing the quality of the parameter estimated, the norm of the calibrated data was calculated for each frame. The norm of the magnetometer and accelerometer output are presented in Figure 3:
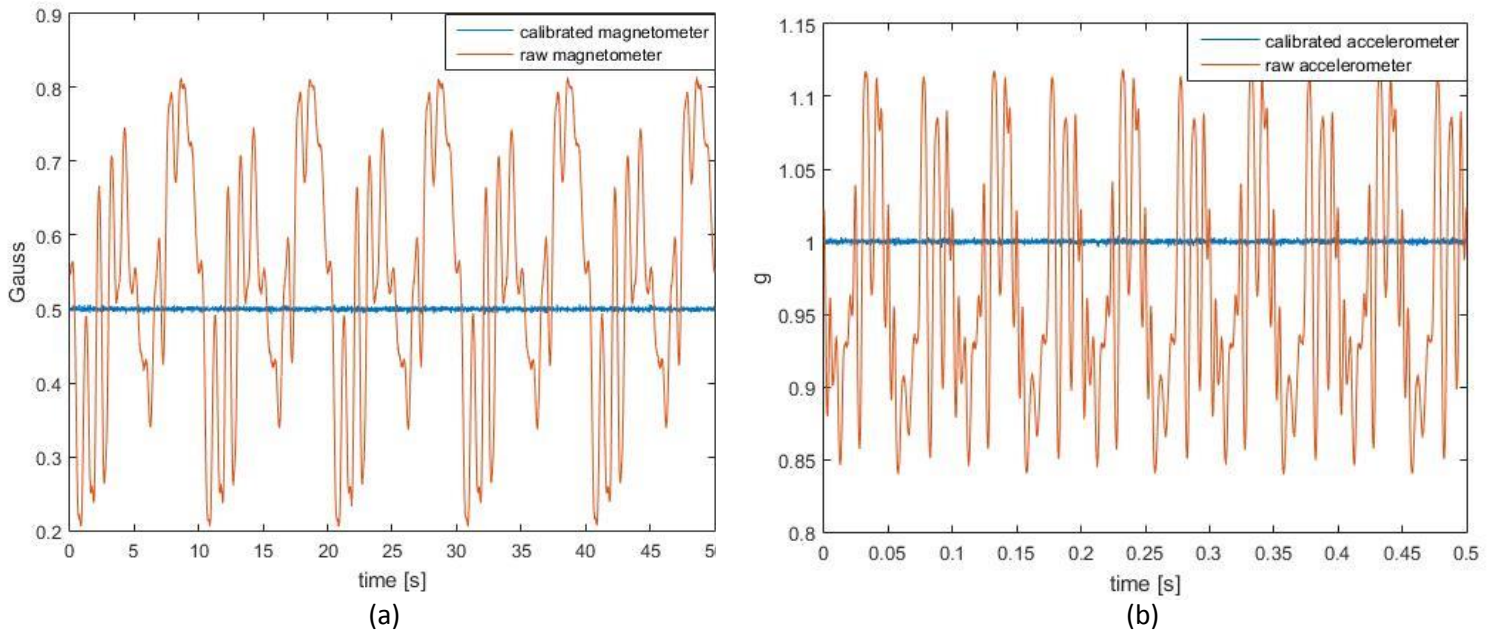
Figure 3. (a) The norm of raw and calibrated magnetometer output is presented over time in red and blue, respectively. The standard deviation of the noise added to the signal was 2 mG. (b) The norm of raw and calibrated accelerometer output is presented over time in red and blue, respectively. The standard deviation of the noise added to the signal was 1 mg.

The errors between the calibration parameters estimated and the real calibration parameters resulted

in all the cases examined at least 4 orders of magnitude lower than the parameters to be estimated, if the noise standard deviations added to the input measurements were selected equal or inferior of 2 mG for magnetometer and equal or inferior of 1 mg for accelerometer. It must be underlined that 2 mG for

magnetometer and 1 mg for accelerometer are the noise standard deviations declared in datasheets [27,28]. This means that in real conditions, the errors committed in calibrations parameters estimation are negligible with respect to the parameter's values.

Due to this fact, in Table 1 are reported the errors obtained with the higher noise standard deviations tested. The errors reported in Table 1 are calculated as the difference between the calibration parameters estimated and the real calibration parameters and multiplied for 1000.

$e\mathbf{W}_m$			$e\mathbf{O}_m$	$\mathbf{eW}_a^1$			$\mathbf{eO}_a^1$	$\mathbf{eB}_0$
0.00	-2.74	-0.02	-0.83	-0.38	-0.02	-0.15	0.02	1.38
-0.17	1.22	0.94	1.13	-0.02	0.05	-0.29	-0.21	0.00
0.37	-1.43	1.00	0.06	-0.15	-0.29	0.88	0.15	-3.80

Table 1. All the errors reported in table 1 are multiplied for 1000 for a better data representation. $\mathbf{\textit{e}W}_m$, $\mathbf{\textit{e}O}_m$, $\mathbf{eW}_a^1$, $\mathbf{eO}_a^1$, $\mathbf{eB}_0$ represents the errors in $\mathbf{W}_m$, $\mathbf{O}_m$, $\mathbf{W}_a^1$, $\mathbf{O}_a^1$, $\mathbf{B}_0$ estimation, respectively.

3.2. Real Data Acquisitions

In this subsection the results emerging from real data acquisitions will be presented. As a first representation of the changing in the calibrated

accelerometer and magnetometer output in real data, raw and calibrated data are plotted in Figure 4 as a 3D graph:
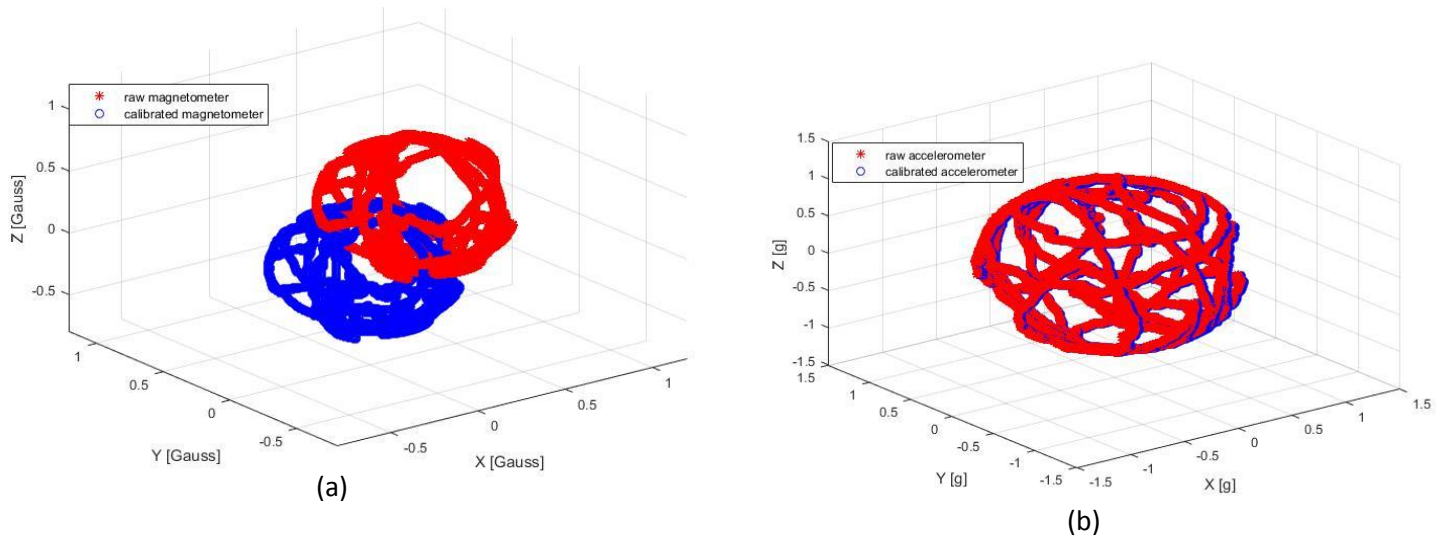
Figure 4. (a) Raw and calibrated magnetic field measurements are plotted in a 3D graphs in red and blue, respectively. (b) Raw and calibrated accelerometer measurements are plotted in a 3D graphs in red and blue, respectively.

The norm of the magnetometer and accelerometer output emerging from a single acquisition are presented in Figure 5:
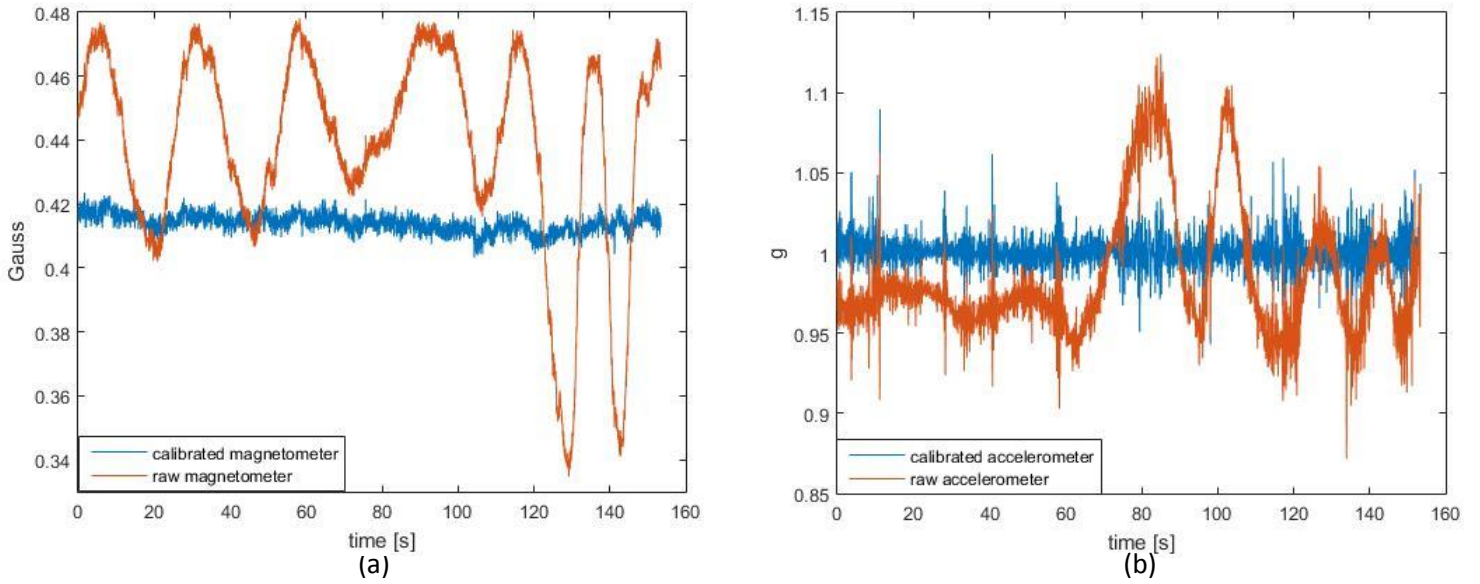
Figure 5. (a) The norm of raw and calibrated magnetometer output is presented over time in red and blue, respectively. (b) The norm of raw and calibrated accelerometer output is presented over time in red and blue, respectively.

The comparison of the rotation matrix $\mathbf{R}_k$ (Equation 6) obtained from MIMU with the same matrix obtained with stereo-photogrammetry, is reported in Figure 6 for a single data acquisition. The presented comparison is an indirect index of the quality of the calibration process.
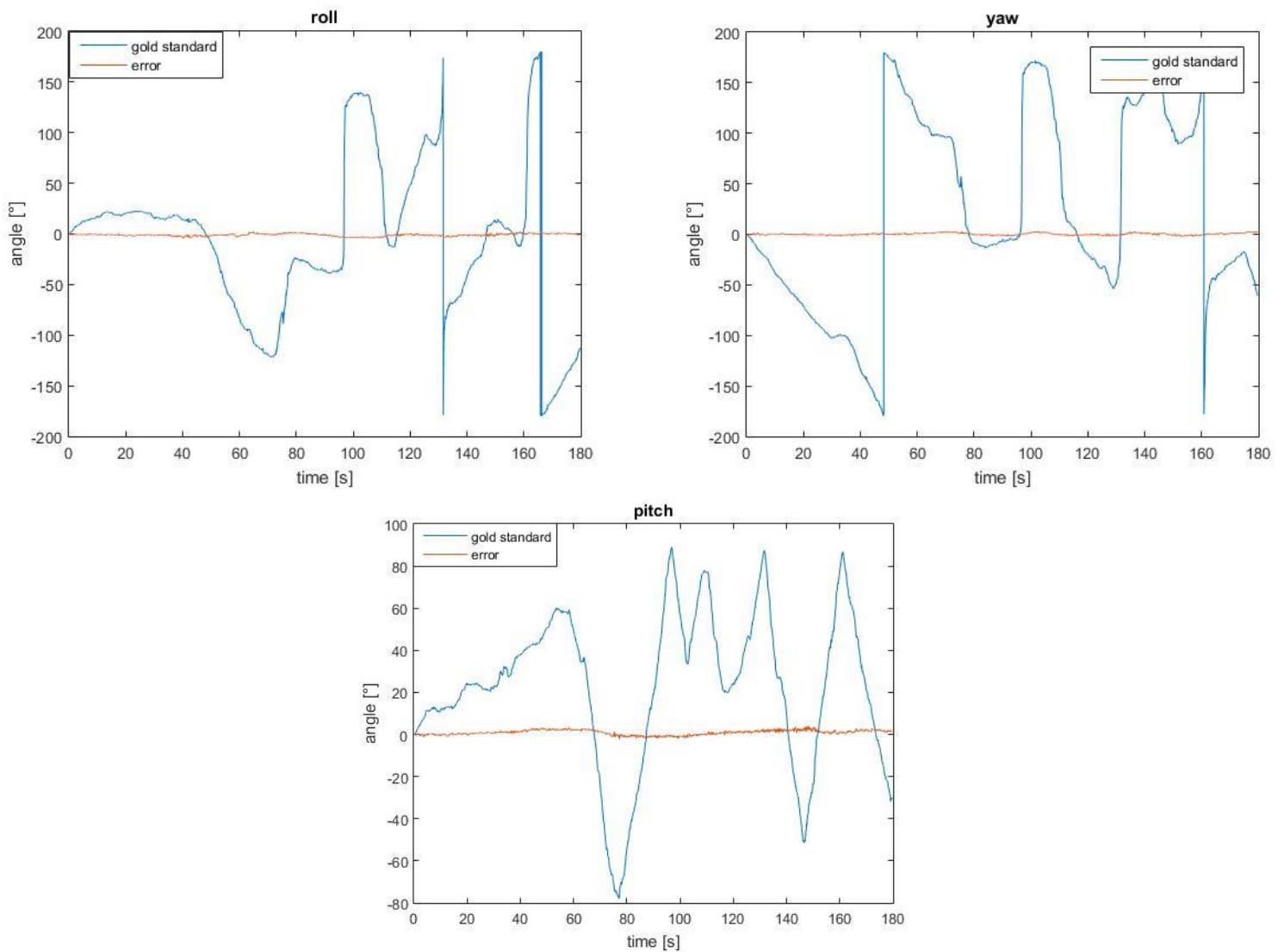
Figure 6. A comparison, in terms of roll, pitch and yaw, is reported in figure for a single data acquisition. Blu lines represent the gold standard calculated from stereophotogrammetry; red lines represent the error between stereophotogrammetry and MIMU

Finally, a numerical comparison in all the data acquired is reported in Table 2:

	Roll	Pitch	Yaw
RMSE_MIMU1_test1 [°]	1.47	1.66	2.54
RMSE_MIMU1_test2 [°]	1.1	1.51	2.3
RMSE_MIMU1_test3 [°]	1.73	2.84	2.16
RMSE_MIMU1_test4 [°]	2.71	1.72	3.16
RMSE_MIMU1_test5 [°]	2.07	0.7	3.39
RMSE_MIMU1_test6 [°]	1.49	1.05	3.3
RMSE_MIMU2_test1 [°]	1.63	1.49	0.99
RMSE_MIMU2_test2 [°]	1.59	1.85	1.39
RMSE_MIMU2_test3 [°]	1.93	0.98	2.61
RMSE_MIMU2_test4 [°]	1.82	1.86	2.51
Mean ± STD [°]	1.76 +- 0.43	1.57 +- 0.59	2.44 +- 0.78

Table 2. The errors in $\mathbf{R}_k$ estimate between MIMU and stereo photogrammetry are reported for all the acquisitions in terms of roll, pitch and yaw. The columns represent the angular error in roll, pitch and yaw estimate, expressed as RMSE. In each row a different acquisition is reported. Last row indicates the mean and the standard deviations of the RMSE in all the acquisitions.

4. Discussion

The presented paper suggests a novel method for the simultaneous calibration of triaxial accelerometer and triaxial magnetometer without external references, offering a simple and effective tool for MIMU calibration without the use of external systems.

Many existing algorithms for MIMU calibration use actuated mechanical systems to position the MIMU in known orientations and rotate at known and/or constant rotation rates [16 17]. These methods offer a robust and accurate solution but are difficult to use on a large scale due to the need for the presence of machinery dedicated to calibration which is often very expensive.

In recent years, some algorithms for accelerometer or magnetometer calibration without external references were proposed [12–15]. The weak point of these algorithms is that the calibration must be performed independently, so the magnetometer and accelerometer are calibrated in different frames, and the rotation between them is unknown.

Furthermore, to the knowledge of the authors, no existing method can estimate the direction of the magnetic field simultaneously to the calibration parameter of both accelerometer and magnetometer. The norm and the direction of the magnetic field may be usually unknow, even if they can be very important for their use in sensor-fusion algorithms for attitude estimation using data from MIMU [7].

To overcome the limitations of the existing methods, a new method was proposed and tested on both simulated and real data.

The simulated experiments aimed to demonstrate the validity of the proposed method under controlled data and allowed comparison between the estimates and the ground truth. As reported in Figure 1, the calibrated data can differ from raw data in a significative way, depending on the calibration parameters. More specifically, the offset parameters $(\mathbf{O}_m, \mathbf{O}_a^1)$ are directly related to the distance from the centre of the sphere representing the calibrated data and the ellipsoid representing the raw data; the parameters related to $\mathbf{W}_m, \mathbf{W}_a^1$ are related to the length and orientation of semi-axes of the ellipsoid. After data calibration, the 3D measurement along the local axes are very similar to a sphere, indicating a good calibration procedure. This can be more evident in Figure 2, where the differences between the norm of the raw and calibrated data is shown for both accelerometer and magnetometer. Figure 2 illustrates that the norm of the calibrated data is constant over time, independently from the MIMU orientation. The most important part of the simulated data results is related to the errors between the calibration parameters estimated and the real calibration parameters. In all the cases examined in which the noise standard deviations added to the input measurements were selected equal or inferior of 2 mG for magnetometer and equal or inferior of 1 mg for accelerometer, the errors in parameters estimate were at least 4 orders of magnitude lower than the parameters to be estimated. This means that in real conditions [27,28], the errors committed in calibrations parameters estimation are negligible with respect to the parameter's values.

Table 1 shows the errors (multiplied for 1000) in parameters estimation. It must be noted that the maximum error found is 0.0038; this error resulted 3

orders of magnitude lower than the parameter to be estimated, indicating an excellent calibration.

In real experiments these findings were confirmed. The same behavior of the simulated data was found comparing Figure 1 with Figure 4. The only difference between them is due to a greater magnetometer offset in real data; this is surely due to a not negligible hard iron effect on the MIMU. It must be underlined that the norm of $\mathbf{O}_m$ resulted of the same order of magnitude with respect to the Earth magnetic field; this consideration points out the importance of magnetometer calibration. As for the simulated data, the norm of the calibrated data from real acquisition is constant over time, as reported in Figure 5.

The effect of the real data calibration was evaluated in an indirect way comparing the rotation matrix $\mathbf{R}_k$ (Equation 6) obtained from MIMU with the same matrix obtained with stereo-photogrammetry, that can be considered the gold standard. In fact, the more $\mathbf{R}_k$ estimated from MIMU data (using algorithm proposed in [9]) is similar to $\mathbf{R}_k$ estimated from stereo-photogrammetry, the more the calibration took place correctly.

The accuracy in orientation estimate was evaluated in ten different acquisitions, and the results was reported in Figure 6 and Table 2. In Figure 6 the errors in roll, pitch, yaw estimate were reported for a single acquisition lasting three minutes, showing excellent results. Table 2 summarize the errors in all the acquisitions. The results obtained for roll and pitch angles are comparable with the ones obtained in [9], although the gyroscope was also calibrated in [9]. As reported in Table 2, errors in yaw angle estimation are

smaller than the ones obtained in [9], indicating an excellent magnetometer calibration.

One limitation of the proposed study may be the lack of gyroscope calibration. This is due to the fact that gyroscope can not be calibrated without external references. Further studies may include the gyroscope calibration using an external reference, as proposed in [14].

Future developments of the presented work will address a unique procedure for accelerometer, magnetometer and gyroscope calibration, considering the related misalignments between the local SoR. More specifically, as proposed in this paper, the gyroscope SoR could be aligned with the ARS.

References

1. Hong, S.K. Fuzzy logic based closed-loop strapdown attitude system for unmanned aerial vehicle (UAV). Sens. Actuators Phys. 2003, 107, 109–118.

2. Barshan, B.; Durrant-Whyte, H.F. Inertial navigation systems for mobile robots. IEEE Trans. Robot. Autom. 1995, 11, 328–342.

3. Titterton, D.; Weston, J.L.; Weston, J. Strapdown Inertial Navigation Technology; IET, 2004; ISBN 978-0-86341-358-2.

4. Luinge, H.J.; Veltink, P.H. Inclination measurement of human movement using a 3-D accelerometer with autocalibration. IEEE Trans. Neural Syst. Rehabil. Eng. Publ. IEEE Eng. Med. Biol. Soc. 2004, 12, 112–121.

5. Picerno, P. 25 years of lower limb joint kinematics by using inertial and magnetic sensors: A review of methodological approaches. Gait Posture 2017, 51, 239–246.

6. Woltring, H.J. On optimal smoothing and derivative estimation from noisy displacement data in biomechanics. Hum. Mov. Sci. 1985, 4, 229–245.

7. Sabatini, A.M. Estimating three-dimensional orientation of human body parts by inertial/magnetic sensing. Sensors 2011, 11, 1489–1525.

8. Madgwick, S.O.H. Automated calibration of an accelerometers , magnetometers and gyroscopes-A feasibility study.; 2011.

9. Valenti, R.G.; Dryanovski, I.; Xiao, J. Keeping a Good Attitude: A Quaternion-Based Orientation Filter for IMUs and MARGs. Sensors 2015, 15, 19302–19330.

10. Crassidis, J.L.; Markley, F.L.; Cheng, Y. Survey of Nonlinear Attitude Estimation Methods. J. Guid. Control Dyn. 2007, 30, 12–28.

11. Madgwick, S.O.H. An efficient orientation filter for inertial and inertial / magnetic sensor arrays.; 2010.

12. Gebre-Egziabher, D.; Elkaim, G.H.; Powell, J.D.; Parkinson, B.W. Calibration of Strapdown Magnetometers in the Magnetic Field Domain.; 2004.

13. Renaudin, V.; Afzal, M.H.; Lachapelle, G. Complete Triaxis Magnetometer Calibration in the Magnetic Domain. J Sens. 2010, 2010, 967245–967245.

14. Sarkka, O.; Nieminen, T.; Suuriniemi, S.; Kettunen, L. A Multi-Position Calibration Method for Consumer-Grade Accelerometers, Gyroscopes, and Magnetometers to Field Conditions. IEEE Sensors Journal 2017, 17(11), 3470–3481.

15. Metge, J.; Giremus, A.; Mégret, R.; Berthoumieu, Y.; Décamps, T. Calibration of an inertial-magnetic measurement unit without external equipment, in the presence of dynamic magnetic disturbances. Meas. Sci. Technol. 2014, 25.

16. Hanse, J. Method for calibrating an inertial measurement unit 2004.

17.   Development of an Automatic IMU Calibration System - PDF Available online: https://docplayer.net/35832470-Development-of-an-automatic-imu-calibration-system.html (accessed on Oct 3, 2019).

18.   Conrado Silva Miranda; Janito Vaqueiro Ferreira Efficient Simultaneous Calibration of a Magnetometer and an Accelerometer; arXiv.org, 2015;

19.   Gietzelt, M.; Wolf, K.-H.; Marschollek, M.; Haux, R. Performance comparison of accelerometer calibration algorithms based on 3D-ellipsoid fitting methods. Comput. Methods Programs Biomed. 2013, 111, 62–71.

20.   Muraccini, M.; Mangia, A.L.; Lannocca, M.; Cappello, A. Magnetometer Calibration and Field Mapping through Thin Plate Splines. Sensors 2019, 19.

21.   Secer, G.; Barshan, B. Improvements in deterministic error modeling and calibration of inertial sensors and magnetometers. Sens. Actuators Phys. 2016, 247, 522–538.

22.   Buffington, G. Polar Decomposition of a Matrix. Apuntes 2014, 1–11.

23.   Wahba, G. A least-square estimate of spacecraft attitude. SIAM Rev. 1965, 7, 409

24.   Arun, K.S.; Huang, T.S.; Blostein, S.D. Least-Squares Fitting of Two 3-D Point Sets. IEEE Trans. Pattern Anal. Mach. Intell. 1987, PAMI-9, 698–700.

25.   Eggert, D.W.; Lorusso, A.; Fisher, R.B. Estimating 3-D rigid body transformations: a comparison of four major algorithms. Mach. Vis. Appl. 1997, 9, 272–290.

26.   Fletcher, R.; Powell, M.J.D. A Rapidly Convergent Descent Method for Minimization. Comput. J. 1963, 6, 163–168.

27.   MEMSIC, Inc - Magnetic Sensor Components | MMC3416xPJ Available online: http://www.memsic.com/magnetic-sensors/MMC3416xPJ (accessed on Nov 12, 2018).

28. LIS344ALH - 3-axis analog accelerometer, ±2 g / ±6 g user selectable full-scale, ultra compact, low power - STMicroelectronics Available online: https://www.st.com/en/mems-and-sensors/lis344alh.html (accessed on Oct 3, 2019).

29. FXAS21002 | 3-Axis Digital Gyroscope | NXP Available online: https://www.nxp.com/products/no-longer-manufactured/3-axis-digital-gyroscope:FXAS21002C (accessed on Oct 3, 2019).

Chapter 4

Evaluation of a novel portable three-dimensional scapular kinematics assessment system. Inter and intra-observer reproducibility and normative data for healthy adults[1]

Abstract

Purpose: To evaluate the intra and interobserver reproducibility of a new system for evaluating three-dimensional humero-scapulo-thoracic kinematics using wearable technology in an outpatient setting.

Methods: The SHoW Motion 3D kinematic tracking system is a motion analysis system that uses wireless wearable non-invasive inertial-magnetic sensors to assess the three-dimensional kinematics of the shoulder girdle. The sensors placed over the skin in the sternum, scapular spine and arm to precisely define angular motions of the humerus and the scapula with three Degrees Of Freedom (DOF) for each segment.

The system was used to measure the scapular angular motions in three planes (upward/downward rotation, internal/external rotation and anterior/posterior tilt) during two shoulder full-range movements (flexion/extension and abduction/abduction) in both shoulders of 25 healthy volunteers. One examiner made two consecutive evaluations in the first visit and another one week after, and a second examiner made another evaluation during the first visit.

A mean curve was computed from the normalized data for each measurement to obtain normative data for scapular angular kinematics. Intra and inter-observer reproducibility was evaluated using Root Mean Square Error Estimation (RMSE) and Coefficients for Multiple Correlations (CMC).

Results: 25 healthy volunteers (13 males and 12 females, mean age: 37 [standard deviation 11.1] years) were evaluated four times. A total of 200 analysis were pooled to get normative values for relations between humeral

elevation angles and the three angular movements of the scapula. In the CMC analysis the system showed at least very good (CMC>0.90) intra and inter-observer reproducibility for scapular tilt and upward-downward rotations both in flexion and abduction. For scapular internal-external rotation the results were acceptable (CMC>0.75) but not as good, especially in the abduction movement. RMSE calculations showed consistently good reproducibility with RSME<4º for all three angles evaluated in flexion and abduction.

Conclusion: The SHoW Motion 3D kinematic tracking system is an easy to use, reproducible system for quick and detailed assessment of scapular angular kinematics in healthy adults. The data obtained is similar to that obtained with other validated methods.

Level of evidence: Clinical relevance: the presented system is portable, easy to use and fast. It also has good intra and inter-observer reproducibility, making it an excellent tool to assess objectively scapular dyskinesis in the clinical setting.

1. Introduction

The role that scapular dyskinesis (defined as "the alteration of normal scapular kinematics"[12]) has in shoulder pathology has often been overlooked. There is increased awareness in that the scapula and its dynamic behaviour play a key role in shoulder problems[22]. In all the spectrum of shoulder pathologies, from instability[18] to cuff[13] or acromioclavicular joint[19] injuries, there are alterations in the humero-scapulo-thoracic rhythm that play a key role in the genesis of the problem, its development or affect the outcomes of treatment.

Probably the main obstacle to correctly identify and manage scapular dyskinesis in subjects with shoulder problems is the difficulty to asses it in a standardized, objective manner. Imaging studies are static and fail to identify the dynamic alterations. Physical exam has also limitations, and there is consensus[13] that little can be properly evaluated apart from identifying altered scapular movement patterns (that resist classification) and a couple of clinical test.

A more precise scapular kinematic assessment can be obtained in experimental settings using motion tracking systems that either use cumbersome equipment[1, 2] or require invasive sensors[15]. Recently, advances in miniaturization and computing power have allowed the development of electromagnetic motion tracking systems that allow for easier, non-invasive scapular kinematics assessment[4, 9, 21] but a simple, standardized, reproducible system that can be used seamlessly in clinic during the standard assessment of most patients has not been developed yet.

The objective of this study was to evaluate a new scapular motion tracking system, the SHoW Motion 3D kinematic tracking system, that is specifically designed to be easy to use in a busy clinical practice. Evaluation was performed assessing the intra and interobserver reproducibility and acquiring normative data for a healthy population.

2. Materials and Methods

Instrumentation:

The SHoW Motion 3D kinematic tracking system (NCS Lab, Carpi, Italy) is a system that combines motion tracking and superficial electromyography to monitor the motion pattern of the shoulder. To the purpose of this study, the electromyographic analysis was not included in data acquisition. The system includes five wireless miniature magnetic and inertial measurement units (MIMU, NCS Lab, Italy), as illustrated in Figure 1:
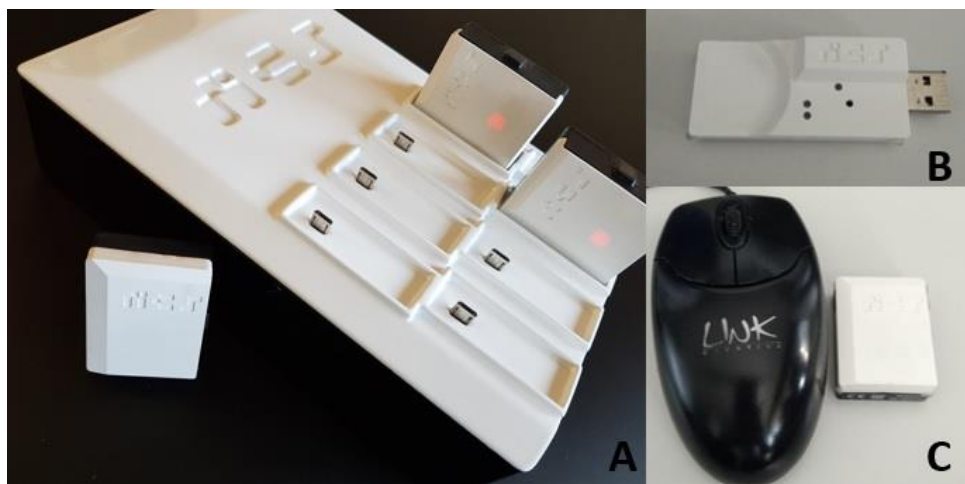
Figure 1. The SHoW Motion 3D kinematic tracking system is composed of a set of five sensors (here shown over a charger, A), a USB receiver (B) that plugs to any laptop and a specific software that must be installed in the laptop. The sensors have approximately the size of a matchbox (C). The sensors, charger straps and receiver weight less than a kilogram and fit easily in any small suitcase.

Each MIMU provides both raw data (accelerometer, magnetometer, gyroscope) and the orientation matrix, representing the orientation of the

local System of Reference (SoR) with respect to a fixed SoR. Data from each MIMU are sampled at 60 Hz, transferred wirelessly to a laptop that has a proprietary software that processes the data according to a biomechanical model. The real time visualization provided by the software is shown in the following figure:
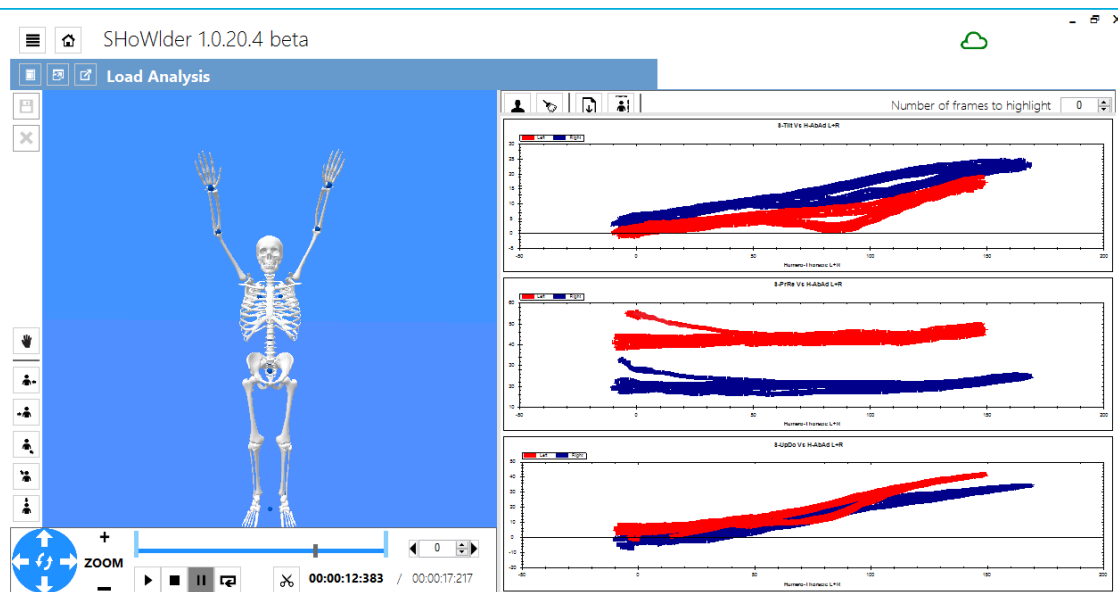
Figure 1.1: The SHoW Motion graphical interface is reported in figure as it appears in real-time. On the left part an avatar represents the movements of the subject and can be used as a biofeedback. On the right part the graphs related to the scapula-humeral rhythm are displayed, for both right (blue lines) and left side (red lines).

To begin measurements the sensors are placed on the standing subject (one at the manubrium sterni, two on each suprascapular fossae and two over the lateral aspect of both arms) according to an standardized protocol, the INAIL Shoulder and Elbow Outpatient protocol (ISEO)[20]. Then the anatomical coordinate systems are created acquiring a static reference trial with the subject standing upright, the humerus positioned alongside the body

and the elbow flexed at 90°. During each session, the subject, standing and starting from a resting position with the arms alongside the body, and the thumbs up, is asked to flex (or adduct) the shoulder until maximum elevation without pain is reached and then to return to the resting position. Each movement is repeated 7 times in a row, but only the central 5 are considered for subsequent calculations.

The scapular angular kinematics (SAK) are dynamically visualized by means of 3 angle–angle plots for each plane of humerus elevation (sagittal or frontal), in which the three scapulothoracic angular motions (upward/downward rotation around a horizontal axis perpendicular to the plane of the scapula; internal/external rotation around a vertical axis through the plane of the scapula; and anterior/posterior tilt around a horizontal axis in the plane of the scapula) are plotted against humero-thoracic elevation or abduction, as shown in Figure 2:
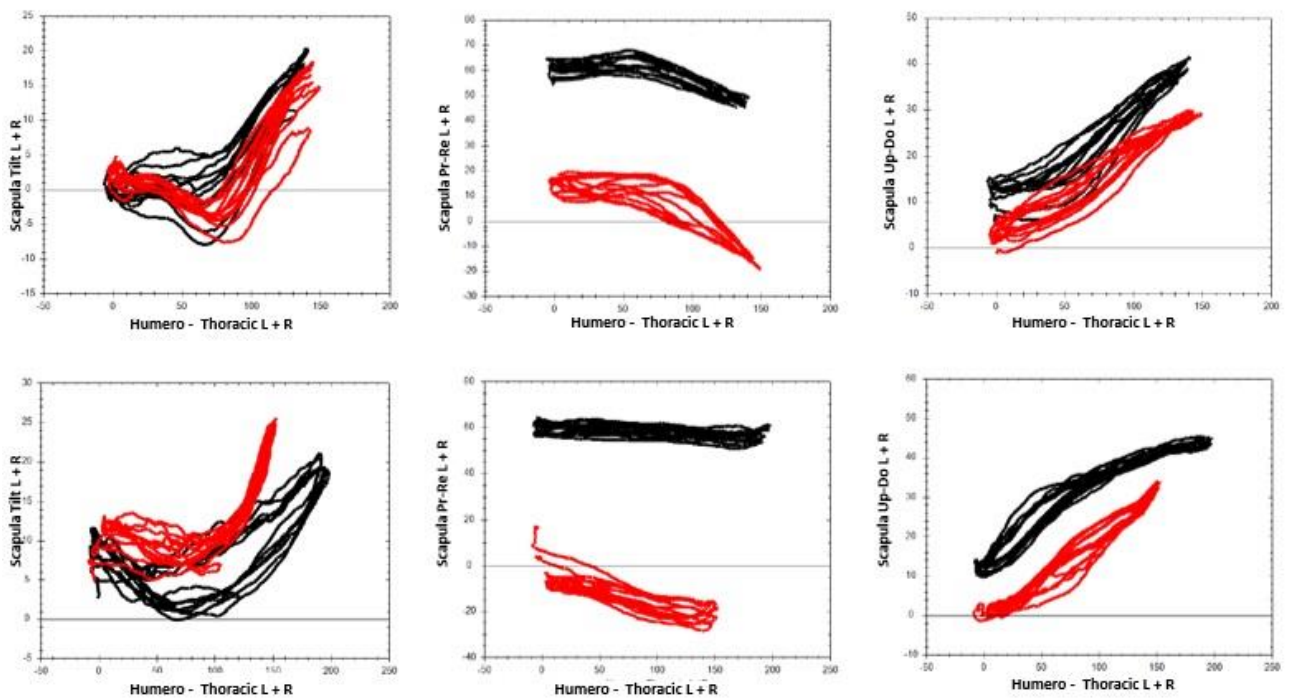
Figure 2: the typical output from the system. A set of six graphs that pit the variations of the three scapular angles studied (upward/downward rotation [S-UpDo], internal/external rotation[S-PrRe] and anterior/posterior tilt[S-Tilt]) against the variations in total shoulder abduction (H-AbAd) or flexion (H-FlEx). The zigzaging lines in the graphs represent the different repetitions for each movement. There are two lines in each graph representing both arms (red lines for left side, black lines for right side). In a normal evaluation the examiner is able to see these six graphs live as they develop.

A standard measurement session, that includes independent assessment of humero-scapulo-thoracic kinematics in the three planes during FL-EX and AB–AD movements can be performed in less than 10 minutes (including time for sensor placement, calibration, measurement and sensor removal).

Sample size calculation:

Based on the recommendations of Eliasziw et al.[6] for goniometric measurements a minimum sample size of 20 individuals (40 shoulders) was considered adequate for reproducibility analysis. A total number of 25 was estimated to control for a possible 20% loss of subjects during Coefficients of Multiple Correlation analysis due to high personal variability[8].

Subjects:

Twenty-five healthy subjects with no history of shoulder pathology (12 females and 13 males, mean age: 37 [standard deviation 11.1] years) agreed to participate in this research study. The kinematic analysis of both shoulders was performed in all subjects. Since agreement between measurements does not depend on the side in which measurements are made, right and left

shoulder of the subjects were considered independently for a total of 50 shoulders.

Written informed consent to participate in the study was obtained for each subject. The study was approved by the Local Institutional Review Board (IRB approval number: 207/18)

Data collection:

Two examiners took part in data collection, both had extensive experience using the system. Four measurement sessions were completed for each subject: three by examiner A (named sessions A1, A2 and A3) and one by examiner B (named session B), following the A1–B –A2 -A3 sequence. The actual examiner assigned to the role of A and B was randomized for each patient. Sessions A1 and A2 were planned in the same day to investigate the "same day" intra-observer reproducibility. Sessions A3 were acquired a week later to investigate the "different day" intra-observer reproducibility, comparing A3 with both A1 and A2. Sessions B were acquired by a different examiner to investigate inter-observer reproducibility after session A1, comparing B with A1, A2 and A3.

Between sessions, the sensors were removed by the examiner and re-applied by the other examiner, who also repeated the static calibration, i.e. repositioned the subject in the calibration posture. Each examiner made sure that no specific marks of the sensor placement remained on the skin of the subjects.

Data processing:

For the measurement of SAK, each movement (i.e., flexion or abduction) was split into an upward and a downward phase from 0° to 120°. Because the use of skin-fixed sensors on the scapular spine may lead to data dispersion at higher humeral elevations, we analysed the SAK for shoulder flexion and abduction only from 0° to 120°, as was previously reported[21]. Each curve was resampled to 241 equally spaced points from 0° to 120° degrees. Only the forward movement was analysed for reproducibility study and prediction band calculation[21].

Prediction band for healthy subjects:

A mean curve was computed from the normalized data for each subject and for each angle–angle plot. The mean curve was offset by the scapula rotation at resting position. Six angle-angle plots were obtained for each subject (three for flexion and three for abduction). The curves were averaged, providing the prediction bands for the group analysed including the mean curve ± 2 standard deviations.

Assessment of the protocol agreement

MATLAB software (MathWorks, Natick, MA, USA) was used to perform statistical analysis of data. The intra and inter-observer agreement of the data

were assessed using Coefficients of Multiple Correlation (CMC) and Root-Mean-Square Error (RMSE).

For each subject, the CMC analysis was conducted in two steps. First, a preliminary calculation of the CMC for intra-session consistency was performed with the data obtained in each single session, so as to exclude those subjects with high personal motion variability[10]. Second, only in subjects in which this preliminary CMC was over 0.90 (meaning they had excellent consistency in their movements), the intra- and inter-observer agreement was assessed for "same day" intra-observer agreement; "different-day" intra-observer agreement and inter-observer agreement [8]. For each SAK plot, the CMC results were interpreted as follows:<0.65, poor; 0.65-0.75 moderate; 0.75-0.85 good; 0.85-0.95, very good; 0.95-1, excellent[10, 11, 25].

The RMSE was estimated for each subject, for each side and for each angle-angle plot, comparing the results obtained in different sessions. The RMSE was used to assess the differences between the average patterns of each side of each subject along the different sessions. In brief, for each angle-angle plot, the error is evaluated as the difference between the scapula patterns of the same side of the subject acquired in two different sessions. RMSE is calculated as the square root of the average over humerus angles of squared errors as defined by Parel et al.[21].

RMSE estimates the similarity of patterns, with low values for similar patterns and high values for different patterns. RMSE ≤ 4° are considered to represent good similarity between patterns[3, 21, 23].

3. Results

The prediction bands representing, for each angle–angle plot, the mean curve
(± 2 standard deviation) acquired over all the subjects analysed, are reported
in Figure 3:
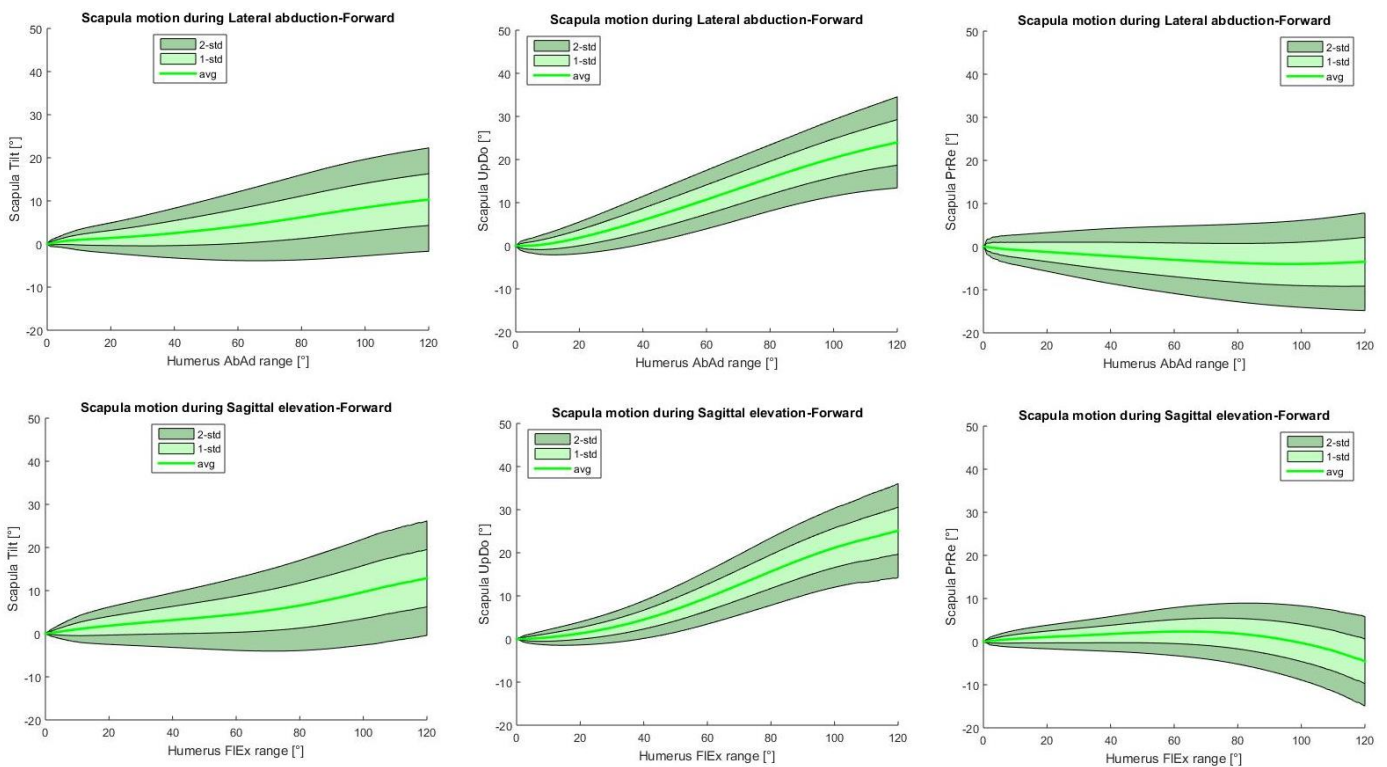
Figure 3: the normative data for all six graphs comparing the variations of the three scapular angles studied (upward/downward rotation [Scapula UpDo], internal/external rotation[Scapula PrRe] and anterior/posterior tilt[Scapula Tilt]) against the variations in total shoulder abduction (Humerus AbAd range) or flexion (Humerus FlEx range). The green shade areas are the prediction bands for 1 SD and 2 SD.

Full shoulder ROM was 170.29 ± 13.44 in abduction and 137.57 ± 9.22 in flexion. The scapular angular inclination values in the three planes for the healthy population at 30, 60, 90, 120 degrees of flexion or abduction are presented in Table 1:

	Scapular internal/external rotation	Scapular upward/downward rotation	Scapular anterior/posterior tilt
30° flexion	1.41±1.69	2.65±1.75	2.52±2.67
60° flexion	2.32±2.78	9.60±3.08	4.52±4.20
90° flexion	0.99±3.92	18.6±4.26	8.00±5.71
120° flexion	-4.57±5.20	25.2±5.44	12.9±6.65
30° abduction	-1.71±2.74	3.75±2.35	1.89±2.32
60° abduction	-3.06±3.91	10.7±3.40	4.12±3.98
90° abduction	-3.98±4.78	18.1±4.10	7.35±5.32
120° abduction	-3.53±5.66	24.0±5.29	10.3±6.01

Table 1: Representative values of the three scapular angles during flexion and abduction at 4 specific angulations (30º-60º-90º and 120º). The data is presented as mean ± standard deviation.

The intra-subject variability using the preliminary CMC calculation was higher than 0.90 in 81% cases for abduction and in 77% cases for flexion. Cases with lower values were excluded from the computation of the inter and intra-operator CMC. The values for all three CMC and for each scapula rotation are presented in Table 2 and 3. The system showed excellent or very good reproducibility for most measurements, except for scapular internal/external rotation in abduction.

FLEXION	Scapular internal/external rotation	Scapular upward/downward rotation	Scapular anterior/posterior tilt
"Same day" intraobserver	0.74±0.18	0.95±0.05	0.92±0.10
"Different day" intraobserver	0.74±0.21	0.94±0.06	0.91±0.09
Interobserver	0.68±0.25	0.90±0.09	0.89±0.14

Table 2: CMC values for reproducibility of the scapular angles during shoulder flexion. The data is presented as mean±standard deviation. Most measurement presented very good reproducibility (CMC>0.75) with moderate reproducibility (CMC between 0.65 and 0.75) for interobserver agreement in scapular internal-external rotation.

ABDUCTION	Scapular internal/external rotation	Scapular upward/downward rotation	Scapular anterior/posterior tilt
"Same day" intraobserver	0.75±0.19	0.95±0.05	0.89±0.13
"Different day" intraobserver	0.73±0.24	0.95±0.05	0.91±0.09
Interobserver	0.67±0.29	0.90±0.10	0.89±0.15

Table 3: CMC values for reproducibility of the scapular angles during shoulder abduction. The data is presented as mean±standard deviation. Most measurement presented very good reproducibility (CMC>0.75) with acceptable results for intra-observer agreement in scapular tilf and upward/downward rotation and poor results for inter-observer agreement in scapular internal-external rotation.

For both flexion and abduction tasks, the RMSE, expressed in degrees, is reported in Figure 4 for each scapula rotation and for each comparison. The system showed good intra and inter-observer reproducibility with all measurements below 4º.
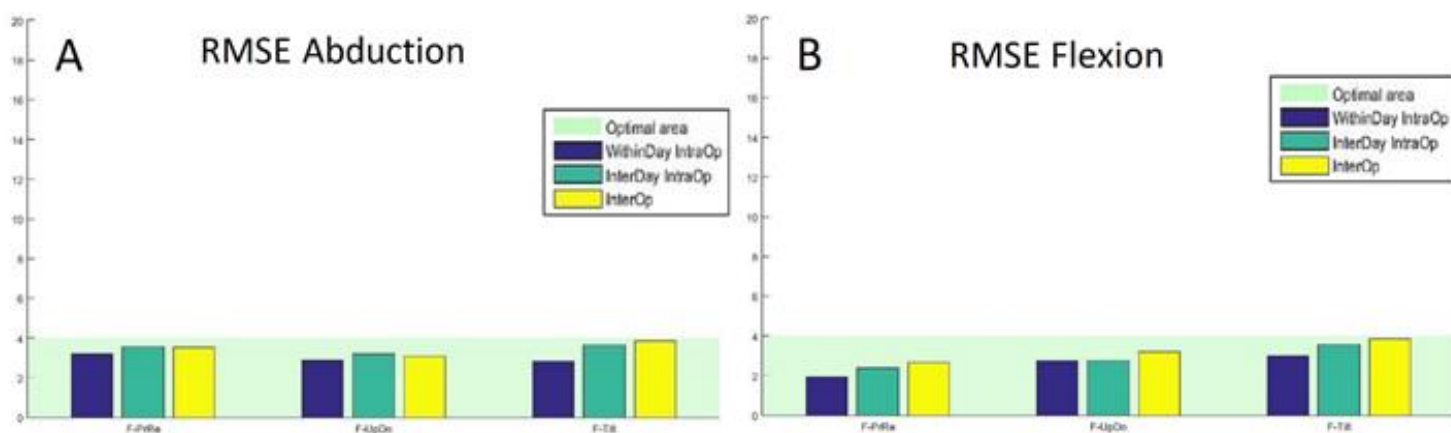
Figure 4: The calculated RMSE for the three reproducibility analysis ("same day" intra-observer reproducibility [WithinDay IntraOP], "different day" intra-observer reproducibility [InterDay IntraOp], and inter-observer reproducibility[InterOp]). The data is presented for all three scapular angles evaluated (upward/downward rotation [S-UpDo], internal/external rotation[S-PrRe] and anterior/posterior tilt[S-Tilt]) during flexion (A) and during abduction (B).

4. Discussion

The most important finding of this study is that the SHoW Motion 3D kinematic tracking system is a reproducible method to assess scapular angular kinematics during flexion and adduction shoulder movements in healthy adults. Normative data from 50 shoulders regarding angular kinematics in three planes was also obtained.

The fact that scapular dyskinesia has as significant role in many shoulder problems is something that is being increasingly understood in the last decade[13, 22]. But there is a significant lack of proper tools to assess scapular kinematics; the only well recognized means to evaluate these in a clinical setting are visual inspection of the movement of the scapula (and comparison to the healthy contralateral side) and the scapular assistance test and scapula retraction test. Although the combination of these test has been suggested to be a good strategy to assess scapular kinematics[14], the truth is that these have a clear lack of face validity[5].

The new system presented here has some clear advantages for the clinician: it is simple to use, requires only one examiner, uses limited equipment that is highly portable, and can be used in a busy clinical setting without a significant loss of time. The outputs it presents are relatively easy to interpret

and comparisons to the contralateral side or previous exams can be done seamlessly. But to have a real clinical relevance it needs to be consistent and useful in identifying and characterizing specific shoulder problems. It also needs to have normative data of values from healthy populations. This study attempts to provide some healthy population data and confirm that the system can be used consistently by different investigators and that, in healthy individuals the results seem to be consistent in time.

A lot of analysis (200 shoulder studies) were performed to present the scapular angular kinematics of a healthy population. The data presented in figure 2 is similar to the results obtained by other studies that have used optoelectronic[8, 17] or inertial-magnetic[4] systems. The variations during the flexion and abduction are obtained with our novel methods were consistent in range and direction with those previously reported. One limitation of this study is that there is not a direct comparison with any previously validated system.

Two tools were used to evaluate the reproducibility of the data obtained with the new system: CMC and RMSE. CMC are being increasingly considered the best alternative for reproducibility assessment of angle-angle plots such as those obtained here, as these explore the general similarities of the SAK curves, assessing the ROM, shape, offset and slope of the curves[7], indeed these are being systematically used to test the reproducibility of systems that assess scapular kinematics[2, 19, 21, 23]. RMSE is one of the most frequently used measures of the goodness of fit of generalized regression models and is a well-validated method to assess reproducibility of systems that output data

in a waveform, specifically it has been used extensively in evaluating reproducibility in shoulder biomechanics [3, 21].

The reproducibility of the system presented here is in par with that of other more complex, expensive and cumbersome measurement systems. Garofalo et al. [8] assessed the reproducibility of an opto-electronic system with skin markers designed to evaluate the scapular angular kinematics and found CMC values consistently around 0.95, results very similar than those obtained by our much simpler system. Parel et al.[20] evaluated the reproducibility of a cumbersome system that used non-wireless inertial-magnetic sensors to evaluate scapular kinematics and found very good intratester CMC values (over 0.90) for tilt and upward-downward rotation during abduction and flexion but the intertester reproducibility, especially for internal-external scapular rotation was unacceptable. The same group[21] also analysed the reproducibility with RMSE and obtained values consistently below 4º. Mattson et al. [17] were not able to reproducibly track scapular motion with a surface mapping system, obtaining RMSE values>5º even when they only tested subjects with prominent scapulas.

In our study the only scapular movement that had limited interobserver reproducibility was scapular internal/external rotation during abduction. This might be due to the fact that the internal/external rotation of the scapula measurement is more susceptible to the initial positioning of the sensors on the scapula spine with respect the other rotations. Despite of this, the results (CMC for intraoberver around 0.75 and for interobserver around 0.60) are similar to those of Parel et al. using an inertial-magnetic system and compare favourably with those of Assi et al[2] and Warner et al.[24] who, using

optoelectronic systems, had difficulties in properly evaluating scapular external-internal rotations.

Another limitation of this study is sample size, specifically regarding the obtention of normative data for healthy individuals. Although a sample size calculation for the reproducibility analysis was indeed performed (something most studies don´t even dare to perform, rarely including more than 10 subjects[16]) the results obtained are limited in scope by the relatively young population recruited for the study.

5. Conclusions:

The SHoW Motion 3D kinematic tracking system is an easy to use, reproducible system for quick and detailed assessment of scapular angular kinematics in healthy adults. The data obtained is similar to that obtained with other validated methods.

References

1. Anglin C, Wyss UP (2000) Review of arm motion analyses. Proc Inst Mech Eng H 214:541-555

2. Assi A, Bakouny Z, Karam M, Massaad A, Skalli W, Ghanem I (2016) Three-dimensional kinematics of upper limb anatomical movements in asymptomatic adults: Dominant vs. non-dominant. Hum Mov Sci 50:10-18

3. Charbonnier C, Chague S, Kolo FC, Chow JC, Ladermann A (2014) A patient-specific measurement technique to model shoulder joint kinematics. Orthop Traumatol Surg Res 100:715-719

4. Cutti AG, Parel I, Raggi M, Petracci E, Pellegrini A, Accardo AP, et al. (2014) Prediction bands and intervals for the scapulo-humeral coordination based on the Bootstrap and two Gaussian methods. J Biomech 47:1035-1044

5. D'Hondt N E, Kiers H, Pool JJM, Hacquebord ST, Terwee CB, Veeger D (2017) Reliability of Performance-Based Clinical Measurements to Assess Shoulder Girdle Kinematics and Positioning: Systematic Review. Phys Ther 97:124-144

6. Eliasziw M, Young SL, Woodbury MG, Fryday-Field K (1994) Statistical methodology for the concurrent assessment of interrater and intrarater reliability: using goniometric measurements as an example. Phys Ther 74:777-788

7. Ferrari A, Cutti AG, Cappello A (2010) A new formulation of the coefficient of multiple correlation to assess the similarity of waveforms measured synchronously by different motion analysis protocols. Gait Posture 31:540-542

8. Garofalo P, Cutti AG, Filippi MV, Cavazza S, Ferrari A, Cappello A, et al. (2009) Inter-operator reliability and prediction bands of a novel protocol to measure the coordinated movements of shoulder-girdle and humerus in clinical settings. Med Biol Eng Comput 47:475-486

9. Hung YJ, Darling WG (2014) Scapular orientation during planar and three-dimensional upper limb movements in individuals with anterior glenohumeral joint instability. Physiother Res Int 19:34-43

10. Kadaba MP, Ramakrishnan HK, Wootten ME, Gainey J, Gorton G, Cochran GV (1989) Repeatability of kinematic, kinetic, and electromyographic data in normal adult gait. J Orthop Res 7:849-860

11. Kavanagh JJ, Morrison S, James DA, Barrett R (2006) Reliability of segmental accelerations measured using a new wireless gait analysis system. J Biomech 39:2863-2872

12. Kibler WB, Ludewig PM, McClure P, Uhl TL, Sciascia A (2009) Scapular Summit 2009: introduction. July 16, 2009, Lexington, Kentucky. J Orthop Sports Phys Ther 39:A1-A13

13. Kibler WB, Ludewig PM, McClure PW, Michener LA, Bak K, Sciascia AD (2013) Clinical implications of scapular dyskinesis in shoulder injury: the 2013 consensus statement from the 'scapular summit'. Br J Sports Med 47:877-885

14. Kibler WB, Sciascia A, Wilkes T (2012) Scapular dyskinesis and its relation to shoulder injury. J Am Acad Orthop Surg 20:364-372

15. Lawrence RL, Braman JP, Laprade RF, Ludewig PM (2014) Comparison of 3-dimensional shoulder complex kinematics in individuals with and without shoulder pain, part 1: sternoclavicular, acromioclavicular, and scapulothoracic joints. J Orthop Sports Phys Ther 44:636-645, A631-638

16. Lempereur M, Brochard S, Leboeuf F, Remy-Neris O (2014) Validity and reliability of 3D marker based scapular motion analysis: a systematic review. J Biomech 47:2219-2230

17. Mattson JM, Russo SA, Rose WC, Rowley KM, Richards JG (2012) Identification of scapular kinematics using surface mapping: a validation study. J Biomech 45:2176-2179

18. Merolla G, Cerciello S, Chillemi C, Paladini P, De Santis E, Porcellini G (2015) Multidirectional instability of the shoulder: biomechanics, clinical presentation, and treatment strategies. Eur J Orthop Surg Traumatol 25:975-985

19. Murena L, Canton G, Vulcano E, Cherubino P (2013) Scapular dyskinesis and SICK scapula syndrome following surgical treatment of type III acute acromioclavicular dislocations. Knee Surg Sports Traumatol Arthrosc 21:1146-1150

20. Parel I, Cutti AG, Fiumana G, Porcellini G, Verni G, Accardo AP (2012) Ambulatory measurement of the scapulohumeral rhythm: intra- and inter-operator agreement of a protocol based on inertial and magnetic sensors. Gait Posture 35:636-640

21. Parel I, Cutti AG, Kraszewski A, Verni G, Hillstrom H, Kontaxis A (2014) Intra-protocol repeatability and inter-protocol agreement for the analysis of scapulo-humeral coordination. Med Biol Eng Comput 52:271-282

22. Roche SJ, Funk L, Sciascia A, Kibler WB (2015) Scapular dyskinesis: the surgeon's perspective. Shoulder Elbow 7:289-297

23. Thigpen CA, Gross MT, Karas SG, Garrett WE, Yu B (2005) The repeatability of scapular rotations across three planes of humeral elevation. Res Sports Med 13:181-198

24. Warner MB, Chappell PH, Stokes MJ (2012) Measuring scapular kinematics during arm lowering using the acromion marker cluster. Hum Mov Sci 31:386-396

25. Yavuzer G, Oken O, Elhan A, Stam HJ (2008) Repeatability of lower limb three-dimensional kinematics in patients with stroke. Gait Posture 27:31-35

Chapter 5

Shoulder kinematics and muscle activity after arthroscopic-assisted latissimus dorsi tendon transfer for irreparable rotator cuff tears[1]

Abstract

Latissimus dorsi tendon transfer (LDTT) is a surgical option for the treatment of an irreparable rotator cuff tear (RCT). Whether a favorable clinical outcome is due to the latissimus dorsi (LD) muscle contraction rather than the passive tenodesis effect remains to be confirmed. The purpose of the current case-control study was to evaluate the shoulder kinematics and LD activation after arthroscopic-assisted LDTT. Eighteen patients suffering from RCT and 18 healthy individuals were included in this study. The patients were examined postoperatively using a 3D kinematic tracking system and superficial electromyography (EMG). No significant shoulder ROM differences were noted between the LDTT side, the contralateral side and the healthy individuals. Significantly higher scapular ROM values were found between the LDTT side and the shoulders of healthy individuals for the flexion-extension and abduction-adduction movements. While performing external rotation with 0° shoulder abduction and 90° elbow flexion (ER1), a greater percentage of the EMG peak value (p=0.047) and a higher LD internal/external rotation ratio (p=0.004) were noted for the transferred LD in comparison to the contralateral shoulder. After LDTT, patients with irreparable massive RCT had a ROM comparable both to the contralateral shoulder and to the shoulders of healthy individuals. The transferred muscle acts as a true external rotator only in ER1, and higher scapular contribution to overall humeral movement can be expected after LDTT compared to the nonsurgical side or to healthy individuals.

Keywords

1. Introduction

Gerber originally defined a massive irreparable posterosuperior rotator cuff tear (MRCT) as the inability to achieve fixation in ≤ 60° of abduction despite adequate releases [1]. MRCT includes at least stage 3 fatty infiltration of the supraspinatus and infraspinatus, an acromiohumeral distance < 7 mm on imaging or static migration of the humeral head [2]. MRCTs can represent up to 20% of all rotator cuff tears [3], and it was estimated that rotator cuff ruptures are irreparable in 9-30% of patients in specialized shoulder centers [4,5]. MRCTs can cause significant shoulder pain and loss of strength and range of motion (ROM), impairing daily living [6]. A variety of treatment options have been proposed ranging from nonoperative treatment to simple debridement with or without biceps tenotomy, partial cuff repair with or without graft augmentation, tendon transfer and reverse total shoulder arthroplasty. Generally, a reverse shoulder arthroplasty is used in an irreparable cuff lesion with osteoarthritis; in the case of a massive cuff lesion with an intact joint in a symptomatic patient, a tendon transposition is preferred [7]. Latissimus dorsi tendon transfer (LDTT) is a surgical option for the treatment of irreparable posterosuperior RCT without degenerative changes to the joint [3]. It was initially proposed in 1988 by Gerber et al. to decrease pain, improve outcomes, and increase ROM to restore active elevation and external rotation of the shoulder in patients with irreparable MRCT [1]. After an open LDTT, the deltoid cannot regain its previous strength [7]; thus, an arthroscopic-assisted modification of this surgical procedure has been developed to spare the deltoid muscle [8]. Moreover, arthroscopy appears crucial for an optimal reinsertion

of the latissimus dorsi (LD) in the greater tuberosity [9]. The biomechanical rationale for tendon transfer is the restoration of force couples of the glenohumeral joint and normal kinematics of the shoulder. LDTT is used to replicate the posterior force couple of the infraspinatus and the teres minor muscle. The insertion of the latissimus dorsi on the floor of the intertubercal groove is transferred to the greater tuberosity of the humerus, which converts this internal rotator of the shoulder to an external rotator [10]. The transferred LD also acts as a depressor with a centering effect on the humeral head, allowing the deltoid to lift and abduct the arm, thus contributing to shoulder motion more effectively. The exact mechanism by which the LDTT restores shoulder function remains a subject of controversy. It has yet to be elucidated whether favorable clinical outcome after LDTT is due to the active muscle contraction rather than the passive tenodesis effect. To the best of our knowledge, ten studies are available on electromyographic (EMG) activity of transferred LD [1,9,11-18]. These studies suggest that in some cases the transfer is truly active, whereas in others the patient cannot actively synchronize the transferred LD with supra- and infraspinatus activity. Only two of these studies evaluated the activity of LD after arthroscopic-assisted procedures [9,11].

Scapulohumeral rhythm (SHR) is a clinical parameter widely used for the functional evaluation of shoulder kinematics. It represents the coordinated movement between the scapula and the humerus when the latter is elevated in the sagittal or frontal plane. For each plane of elevation, the SHR is described by three scapulothoracic rotations (i.e., protraction-retraction, medio-lateral rotation and posterior-anterior tilting) as a function of humeral anteflexion or

humeral abduction. The quantitative evaluation of SHR is often limited by the costs of motion analysis laboratories equipped with optoelectronic systems [19].

Magnetic and inertial measurement units (MIMUs) represent a new generation of motion analysis systems that are commercially available, portable and fully wearable and do not require postprocessing analysis to obtain accurate clinical data [20,21]. To our best knowledge, no study has simultaneously evaluated the muscular activation of the LD and the scapulohumeral kinematics using MIMUs. The purpose of the current study was to compare (1) the shoulder kinematics after arthroscopic-assisted LDTT to the nonsurgical side and to the shoulder of a healthy population and (2) the LD activation after arthroscopic-assisted LDTT to the contralateral muscle.

2. Materials and Methods

Study population

A case-control study (level of evidence III) was performed from May 2015 to May 2016. Thirty-three patients underwent an arthroscopic-assisted LDTT by one surgeon (RC). Among them, 18 patients agreed to participate in this research study; 18 healthy individuals served as a control group. All of the patients gave written informed consent. Inclusion criteria for LDTT were (1) irreparable supraspinatus and infraspinatus tendons [4], and (2) failure of conservative management for at least 6 months, including one course of physical therapy for at least 4 weeks and one course of nonsteroidal anti-inflammatory drugs or analgesic administration. Exclusion criteria were (1)

concomitant subscapularis repair, (2) neurologic deficit, (3) glenohumeral or acromioclavicular osteoarthritis, (4) previous shoulder fracture, (5) glenohumeral instability, (6) frozen shoulder syndrome (<90° of passive abduction and <70° of external rotation), and (7) deltoid insufficiency. The decision for the surgical procedure was based on (1) preoperative magnetic resonance imaging (MRI) to evaluate the tendon healing potential (Fuchs stage I–II, good healing potential; Fuchs stage III, poor healing potential) and (2) intraoperative findings (reparable/irreparable) according to the possibility of reducing the tendon to its footprint after intraoperative mobilization and release [22]. The surgical technique for the LDTT was performed as previously described [23]. The protocol was approved by our Institutional Review Board.

Kinematic and superficial EMG recordings

Patients were examined postoperatively using the SHoW Motion 3D kinematic tracking system (NCS Lab, Carpi, Italy), which combines motion tracking and superficial EMG (sEMG) analysis to monitor the motion pattern and the related muscle activity using wireless sensors. The signals measured by sEMG (Wave Plus Wireless EMG, Cometa, Milan, Italy) and MIMUs (WISE, NCS Lab, Carpi, Italy) were synchronized to obtain a real-time measurement of movements. Indeed, the simultaneous acquisition of sEMG and MIMUs allowed us to synchronize and analyze which muscles were involved in each specific movement. According to the INAIL Shoulder & Elbow Outpatient (ISEO) protocol for the functional evaluation of upper limb kinematics [24], the anatomical coordinate systems were created acquiring a static reference trial with the subject standing upright, the humerus positioned alongside the body

and the elbow flexed at 90°. Repeatability studies showed the consistency of data provided by this protocol [25-27].

Before the measurements began, the participants had a practice session to familiarize themselves with the experimental procedure. Recordings were performed in a quiet room with normal indoor temperature and lighting. The exercises performed by the patients included dynamic movements and isometric contractions. The dynamic movements consisted of active maximal flexion–extension and maximal abduction–adduction of the humerus to allow us to evaluate the ROM and SHR. Each task was repeated seven times [25-26]. ROM was defined as the difference between the maximum and the minimum degree of the principal angle of movement for each patient, both for flexion and for abduction. The ROM values for each group are expressed as the mean and standard deviations. Since throughout the flexion and extension of the humerus, the subject tends to compensate an incomplete shoulder elevation with an extension of the trunk, a specific protocol [24] was used to differentiate the contributions of the humerothoracic and scapulothoracic joints to the humerus elevation. Five wireless MIMUs were placed on thorax, right and left scapula, and right and left humerus [24]. Each MIMU provided both raw data (accelerometer, magnetometer, gyroscope) and the orientation matrix, representing the orientation of the local system of reference (SoR) with respect to a fixed SoR. Data from each MIMU were sampled at 60 Hz, acquired by the system and processed by the biomechanical model. For flexion and abduction tasks, the SHR can be visualized by means of 3 angle–angle plots [25,28,29], whereby the scapulothoracic protraction–retraction, the medio-lateral rotation, and the posterior–anterior tilting are plotted against the humerothoracic

elevation. For the measurement of SHR, each movement (i.e., flexion or abduction) was split into an upward and a downward phase from 0° to 120°. Because the use of skin-fixed sensors on the scapular spine may lead to data dispersion at higher humeral elevations, we analyzed the SHR for shoulder flexion and abduction only from 0° to 120°, as was previously reported.[25] Each curve was resampled to 241 equally spaced points from 0° to 120° degrees. A mean curve was computed from the normalized data for each subject. The mean curve was offset by the scapula rotation at resting position. Twelve angle-angle plots were obtained for each patient (healthy and pathological shoulder) and control. The collected data were processed as previously reported [25], and the curves related to different patients were compared, providing the prediction bands for all the groups analyzed [26].

The LD isometric contractions of the operated and contralateral shoulder of the patients were evaluated by the sEMG during specific tasks. A properly conceived tripod with one degree of freedom of internal and external rotation was used to measure the isometric contraction of LD. Patients were asked to place the forearm on the horizontal support to prevent abduction-adduction movement and to perform maximum voluntary isometric contraction (MVIC) in the following static postures: (P1) shoulder abducted at 0°, elbow flexed at 90°, forearm in the sagittal plane; (P2) shoulder abducted at 0°, elbow flexed at 90°, forearm internal rotated of 45°; and (P3) shoulder abducted at 90°, elbow flexed at 90°, forearm in the sagittal plane. In each of these positions, for both sides, the patients externally and internally rotated the shoulder against a constant resistance 3 times for at least 4 seconds. Between the exercises, the patients rested for 2 minutes. Electromyographic evaluation of the LD muscle

was also performed during the dynamic movements of maximal abduction-adduction and maximal flexion-extension.

According to Konrad et al. [30], for the analysis of sEMG, the maximum voluntary contraction (MVC) was required to normalize the data; therefore, the patients were required to perform MVC during shoulder abduction against a constant resistance. The sEMG signals were sampled at 2000 Hz with 16 bits of resolution, and sEMG sensors were used to acquire the electrical activity of the LD on the left and right sides of the patients. Two 24 mm surface electrodes Ag/AgCl (Kendall/Tyco ARBO; Warren, MI, USA) were placed 2 cm apart, on the center of the LD muscle belly, in the direction of the muscle fibers, according to the European Recommendations for Surface Electromyography [31]. The sEMG data were elaborated as previously described [30]. Every sEMG signal acquired was subtracted from its average value, digitally filtered with a high-pass fifth-order Butterworth filter (10 Hz cut-off frequency), full-wave rectified, and filtered with a low-pass fifth-order Butterworth filter (5 Hz cut-off frequency). A proper skin preparation and the digital signal elaboration procedures allowed us to reduce most of the artifacts from the LD muscle [32]. The output of these elaborations represented the linear envelopes. An algorithm for the automatic identification of muscle activity was developed. The envelopes were normalized and expressed as a percentage of the sEMG peak value, calculated in the MVC task [30]. For each task, the maximum value of the normalized envelop in a 0.5 seconds window was calculated. These values were used to compare the activation of LD in different postures. For internal and external rotation of the humerus, the LD internal/external rotation ratio (LD-IR/ER ratio) [11] was calculated using the following formula, in

which *ER* and *IR* represent, respectively, the values of the normalized envelope during internal and external humeral rotations:

$$\frac{IR}{ER}ratio = \frac{ER - IR}{\max{(ER, IR)}} * 100$$

Statistical analysis

MATLAB software (MathWorks, Natick, MA, USA) was used to perform statistical analysis of data. The normal distribution of the data was checked, and one-way repeated ANOVA or the nonparametric Friedman test was used to evaluate the effect of LDTT. A multiple-comparison test was used for pairwise post hoc analyses. A two-tailed p value < 0.05 was considered significant.

3. Results

Twelve men and 6 women, averaging 59.5 ± 6.5 (47-71) years at surgery, were evaluated 17.8 ± 3.9 (10-24) months after arthroscopic-assisted LDTT. The dominant shoulder was involved in 16 out of 18 patients, and the BMI was 27.6 ± 2.8 (20.9-31.8). An arthroscopic-assisted LDTT was performed in 6 patients (4 males and 2 females) after a failed arthroscopic rotator cuff repair. Eighteen healthy individuals, 10 men and 8 women, averaging 37 ± 8 (27-48) years, served as the control group.

Kinematic evaluation

As shown in Figure 1a, the ROM measured in the dynamic movements of abduction-adduction of the shoulder after LDTT was 148° ± 26°; in the contralateral side and in healthy individuals, 164° ± 13° and 162° ± 12° were measured, respectively. The flexion measured after LDTT was 135 °± 20°. The flexion of the contralateral shoulder and of the shoulders of healthy individuals measured 131° ± 19° and 132° ± 9°, respectively (Figure 1b). No significant ROM differences were noted between the groups. When the movement of the trunk throughout the flexion of the humerus was included in the analysis, 150° ± 21°, 147° ± 18° and 152° ± 20° of flexion were noted for the LDTT side, the contralateral side and the healthy subjects, respectively.
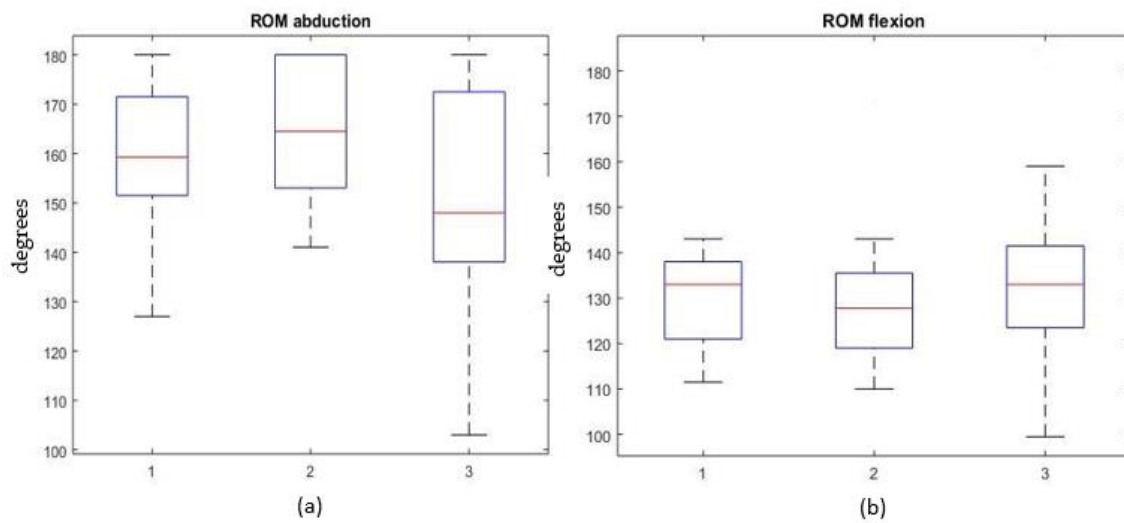
Figure 1. Active range of motion for abduction (a) and flexion (b). Red lines indicate mean, blue squares indicate standard deviation, and dotted lines indicate range values.

The SHR was calculated both for abduction and for flexion movements of the shoulder, and mean curves and standard deviation were extracted for the healthy individuals, the LDTT side and the contralateral side of the patients. As shown in Figure 2, when the SHR curves for the flexion and abduction of the shoulder of LDTT and contralateral side were compared, greater scapular movements were noted after LDTT.
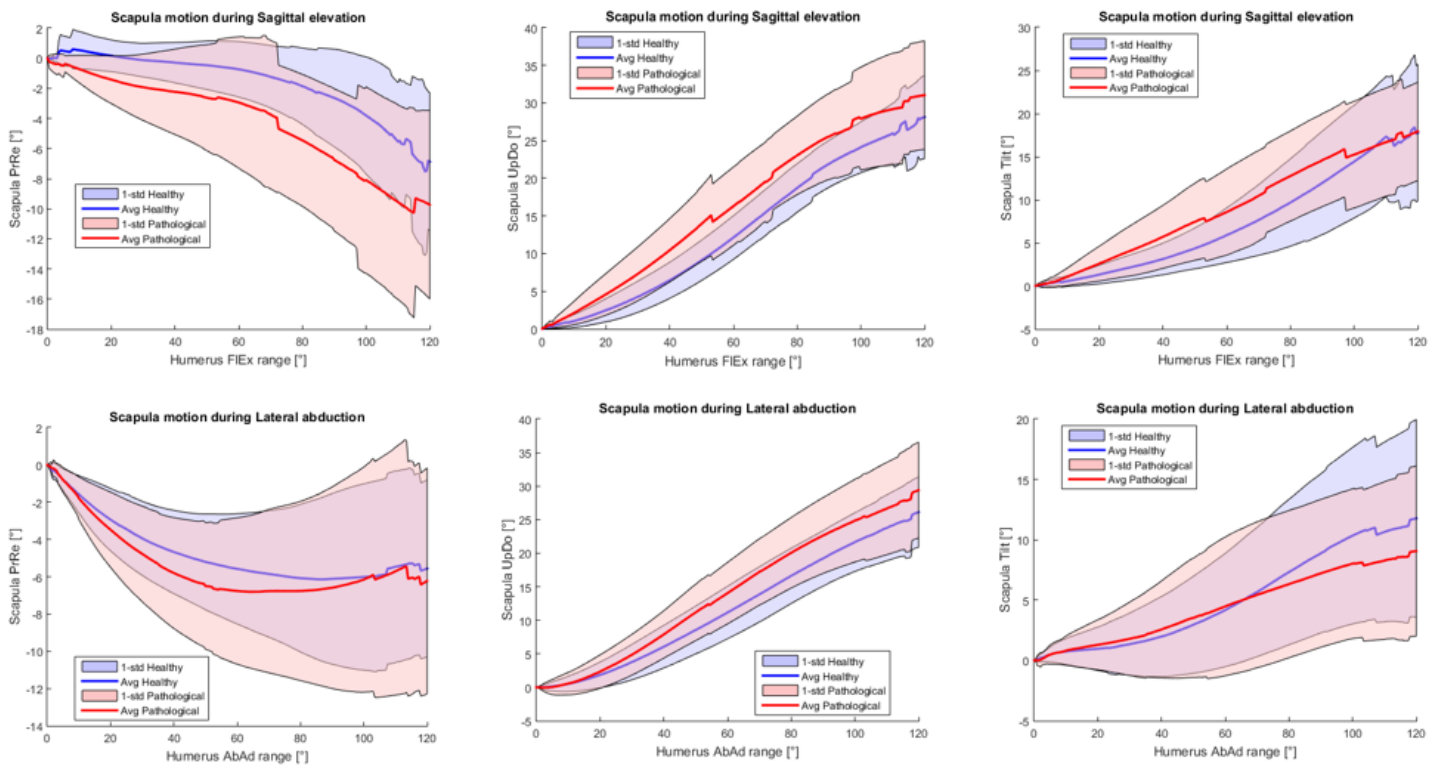
Figure 2. Angle-angle plot of SHR. Mean values with standard deviations of the LDTT side (red curves) and the healthy side (blue curves) are presented for protraction, lateral rotation and posterior tilt throughout sagittal elevation and lateral abduction.

Scapular rotations values were analyzed for each group at predetermined humerus angles (30°, 60°, 90°, 120°) as reported in Table 1:

LDTT side - flexion					
	PrRe FW	UpDo FW	Tilt FW	PrRe BW	UpDo BW	Tilt BW
30°	-0.7 ± 1.7	6.7 ± 3.6	2.9 ± 3.3	-0.6 ± 5.0	2.9 ± 5.7	0.6 ± 4.1
60°	-2.1 ± 4.3	18.0 ± 5.4	7.8 ± 6.5	-2.0 ± 6.2	13.4 ± 7.4	4.4 ± 6.7
90°	-6.3 ± 6.6	27.0 ± 5.8	13.4 ± 7.8	-6.5 ± 6.0	23.6 ± 7.3	11.2 ± 7.4
120°	-9.6 ± 6.4	31.1 ± 7.2	16.4 ± 8.2	-10.8 ± 5.7	29.6 ± 8.7	15.9 ± 7.6

LDTT side - abduction					
	PrRe FW	UpDo FW	Tilt FW	PrRe BW	UpDo BW	Tilt BW
30°	-5.2 ± 2.5	5.6 ± 3.3	2.2 ± 3.2	-5.2 ± 2.5	3.6 ± 2.9	1.5 ± 2.9
60°	-7.6 ± 3.7	14.6 ± 4.8	5.5 ± 6.3	-8.5 ± 2.7	11.0 ± 3.7	4.4 ± 5.8
90°	-7.3 ± 5.2	23.0 ± 5.8	8.9 ± 6.3	-9.1 ± 4.1	21.2 ± 5.3	9.4 ± 6.9
120°	-6.9 ± 6.1	30.2 ± 7.4	11.1 ± 6.5	-8.3 ± 5.6	29.4 ± 7.2	12.2 ± 6.6

Contralateral side - flexion					
	PrRe FW	UpDo FW	Tilt FW	PrRe BW	UpDo BW	Tilt BW
30°	-0.1 ± 1.4	3.7 ± 2.0	2.1 ± 1.8	0.8 ± 3.4	2.8 ± 4.3	1.9 ± 4.0
60°	-0.4 ± 2.4	12.1 ± 3.5	4.8 ± 4.4	-1.0 ± 5.2	12.0 ± 4.7	5.6 ± 5.9
90°	-2.4 ± 4.4	22.3 ± 4.1	10.2 ± 7.4	-4.7 ± 6.1	21.7 ± 4.5	12.3 ± 8.4
120°	-7.6 ± 4.7	28.6 ± 5.8	17.9 ± 10.7	-9.0 ± 4.4	27.6 ± 5.9	18.7 ± 10.2

Contralateral side - abduction					
	PrRe FW	UpDo FW	Tilt FW	PrRe BW	UpDo BW	Tilt BW
30°	-4.0 ± 1.8	3.7 ± 2.7	2.1 ± 2.5	-4.3 ± 3.8	2.7 ± 2.9	1.8 ± 3.3
60°	-5.5 ± 2.8	10.7 ± 3.8	5.0 ± 4.5	-6.1 ± 3.8	9.5 ± 3.4	4.4 ± 4.8
90°	-5.9 ± 4.3	18.5 ± 3.8	9.3 ± 5.7	-6.6 ± 4.2	18.5 ± 3.5	9.9 ± 6.2
120°	-5.0 ± 5.0	25.0 ± 5.2	12.5 ± 7.7	-5.4 ± 4.7	24.7 ± 4.8	13.4 ± 8.1

Healthy individuals - flexion					
	PrRe FW	UpDo FW	Tilt FW	PrRe BW	UpDo BW	Tilt BW
30°	1.4 ± 1.5	2.4 ± 1.3	2.0 ± 2.2	2.6 ± 1.6	1.9 ± 3.3	1.5 ± 2.7
60°	2.5 ± 2.2	9.2 ± 2.0	3.4 ± 3.2	2.2 ± 3.0	9.6 ± 4.8	3.0 ± 4.0
90°	1.2 ± 2.9	18.2 ± 2.6	6.9 ± 4.4	-0.7 ± 3.7	19.5 ± 3.80	7.6 ± 4.2
120°	-5.0 ± 4.2	24.8 ± 2.8	12.5 ± 4.9	-5.7 ± 5.1	24.2 ± 3.6	11.8 ± 4.9

Healthy individuals - abduction					
	PrRe FW	UpDo FW	Tilt FW	PrRe BW	UpDo BW	Tilt BW
30°	-1.5 ± 2.0	3.6 ± 2.0	1.3 ± 1.5	-2.3 ± 2.0	2.9 ± 2.8	0.2 ± 1.7
60°	-2.9 ± 3.1	10.5 ± 3.0	2.9 ± 3.2	-4.2 ± 2.9	10.6 ± 5.1	2.6 ± 3.3
90°	-4.0 ± 3.4	18.1 ± 3.1	5.7 ± 4.1	-5.1 ± 3.4	19.3 ± 5.1	7.6 ± 4.2
120°	-4.1 ± 3.8	24.1 ± 4.3	8.8 ± 4.5	-4.1 ± 4.0	24.5 ± 5.2	10.7 ± 4.2

Table 1. Scapular movements in flexion and abduction for the LDTT side, the contralateral side and healthy individuals. PrRe FW means scapulothoracic protraction in forward humeral movement; PrRe BW, scapulothoracic protraction in backward humeral movement; UpDo FW, scapulothoracic lateral rotation in forward humeral movement; UpDo BW, scapulothoracic lateral rotation in backward humeral movement; Tilt FW, scapulothoracic posterior tilt in forward humeral movement; Tilt BW, scapulothoracic posterior tilt in backward humeral movement.

Statistically significant differences in SHR were found between the LDTT side and the shoulders of healthy individuals for the flexion-extension (Table 2) and abduction-adduction movements (Table 3). Most of these differences were found for the scapulothoracic protraction–retraction and the medio-lateral scapular rotation in flexion and for the medio-lateral scapular rotation in abduction.

	Pr Re FW	UpDo FW	Tilt FW	PrRe BW	UpDo BW	Tilt BW
30 degrees	0.0003	0.00001	NS	0.0387	NS	NS
60 degrees	0.0002	0.000006	0.0335	0.0376	NS	NS
90 degrees	0.0001	0.00003	0.0211	0.0077	0.0478	NS
120 degrees	NS	0.0249	NS	0.0479	NS	NS

Table 2. Comparison between the LDTT, the contralateral side and the healthy population in forward shoulder flexion at 30°, 60°, 90°, and 120°. P-values emerging from statistical analysis were reported for 30°, 60°, 90° and 120° of humerus elevation for each scapula rotations. PrRe FW scapulothoracic protraction in forward humeral movement; PrRe BW, scapulothoracic protraction in backward humeral movement; UpDo FW, scapulothoracic lateral rotation in forward humeral movement; UpDo BW, scapulothoracic lateral rotation in backward humeral movement; Tilt FW, scapulothoracic posterior tilt in forward humeral movement; Tilt BW, scapulothoracic posterior tilt in backward humeral movement. NS, not significant.

	Pr Re FW	UpDo FW	Tilt FW		PrRe BW	UpDo BW	Tilt BW
30°	0.0001	NS	NS		0.0114	NS	NS
60°	0.0003	0.0047	NS		0.0008	NS	NS
90°	NS	0.0024	NS	0.01363	NS		NS
120°	NS	0.0107	NS	NS	0.0395		NS

Table 3. Comparison between the LDTT, the contralateral side and the healthy population during abduction at 30°, 60°, 90°, and 120°. P-values emerging from statistical analysis were reported for 30°, 60°, 90° and 120° of humerus elevation for each scapula rotations. PrRe FW means scapulothoracic protraction in forward humeral movement; PrRe BW, scapulothoracic protraction in backward humeral movement; UpDo FW, scapulothoracic lateral rotation in forward humeral movement; UpDo BW, scapulothoracic lateral rotation in backward humeral movement; Tilt FW, scapulothoracic posterior tilt in forward humeral movement; Tilt BW, scapulothoracic posterior tilt in backward humeral movement; NS, not significant.

sEMG

The envelope of LD muscle activation during dynamic abduction-adduction movement is shown in Figure 3.
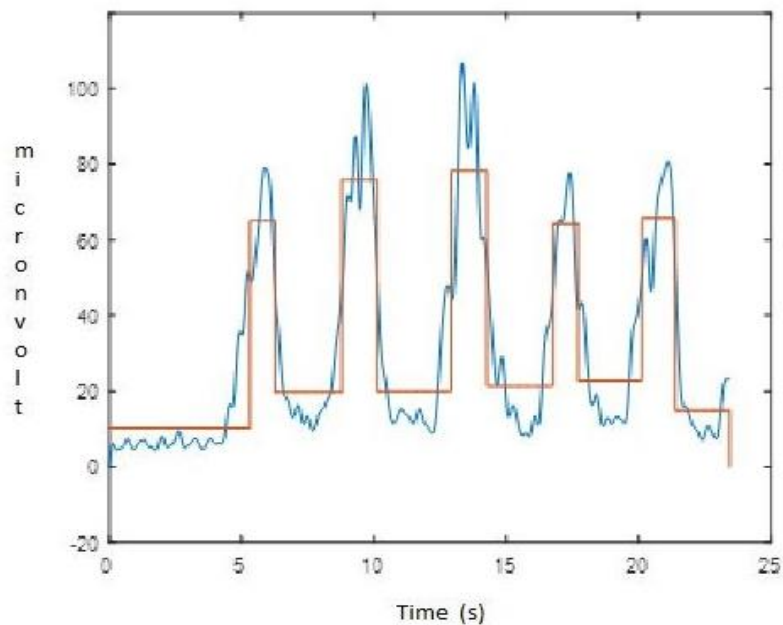
Figure 3. Amplitude analysis. The EMG envelope and the automatic recognition of activation are reported in blue and red, respectively.

No statistically significant differences were noted between the EMG activity of transferred LD and the LD of the contralateral side in flexion or in abduction. While performing external rotation in P1, a greater percentage of the EMG peak value (p=0.047) and a higher LD-IR/ER ratio (p=0.004) were noted for the transferred LD in comparison to the contralateral sides. No significant differences were found in P2 or P3.

4. Discussion

The aim of the present study was to evaluate the shoulder kinematics and LD activation after arthroscopic-assisted LDTT for irreparable rotator cuff tears, acquiring synchronously superficial EMG and kinematic data from MIMU. Various studies have assessed the shoulder function after LDTT using functional scores, but these methods do not represent objective or direct measures of the complex shoulder biomechanics, and there is still no agreement as to the true LD muscle activation during humeral external rotation after tendon transfer. Motion analysis has been applied to study shoulder motion in various shoulder pathologic conditions, such as frozen shoulder, subacromial pain and rotator cuff tears [33-35]. However, little is known about shoulder kinematics after LDTT [18] and the relationship between the shoulder movements and the LD muscle function [11]. Moreover, there is lack of data for the scapulohumeral rhythm after LDTT, although it represents an important clinical indicator [24].

In the proposed study, the patients were examined postoperatively using the SHoW Motion 3D kinematic tracking system, which combines motion tracking and superficial EMG analysis. The simultaneous acquisition of superficial EMG and MIMUs allowed the authors to synchronize and analyze which muscles were involved in each specific movement performed by the patients.

The ISEO protocol was implemented in SHoW Motion for the functional evaluation of upper limb kinematics [24]. This protocol was previously evaluated for intraprotocol repeatability and interprotocol agreement [25], and

a maximum error of 4 degrees was noted between the kinematic output acquired by different operators on the same subject.

In the proposed study, the exercises performed by the patients included dynamic movements and isometric contractions; this allowed the authors to analyze i) the kinematics during movement (ROM and SHR) ii) the related LD activations of LD and iii) the LD activation in different isometric contractions.

The ROM in flexion and abduction of the shoulder after LDTT measured 135° and 148°, respectively. These findings are in line with those of Namdari at al [36] and Henseler et al [18], considering that the ROM obtained from kinematic analysis may differ from one study to another due to the different measurement protocols and the different technology used.

No significant ROM differences were noted among the operated shoulder, the contralateral shoulder and the shoulders of healthy individuals, confirming full recovery after the LDTT.

Greater scapulothoracic joint movements was found after LDTT in comparison to the contralateral side or the shoulders of healthy controls during both flexion and abduction tasks, as reported in Figure 2. In detail, the scapular up-down rotation was the movement that more often differed compared to the contralateral shoulder of patients, and higher scapulothoracic lateral rotation implies lower glenohumeral motion [34], as evident in Figure 2.

Higher scapular lateral rotation facilitates an improved moment arm for deltoid tensioning; thus, the deltoid may compensate for lost rotator cuff function, enabling the patient to maintain a functional ROM [34]. Indeed, scapular lateral rotation has been increased in patients with a rotator cuff tear

[34], and Kolk et al. noted a normalization of scapular movements toward the scapular motion of the contralateral asymptomatic shoulder after rotator cuff repair [38]. In comparison with patients with rotator cuff tears, Paletta et al. reported more glenohumeral motion in healthy volunteers, contributing to overall arm elevation [39]. This study demonstrated that after arthroscopic-assisted LDTT, there was still a reliance on the scapular contribution to overall shoulder motion. Therefore, the transferred LDTT was not able to normalize the scapulothoracic movement, even though biomechanical [40] and clinical studies [18] have shown that the LD transfer has a moment arm about the scapulothoracic as well as the glenohumeral rotation center. After LDTT, the vector force orientation is more vertical than the force vector of the posterior rotator cuff muscles, and this effect could explain the differences in shoulder kinematics between operated and healthy shoulders, with a compensatory scapula movement after LDTT.

The results obtained in the electromyographic analysis suggest that the transferred LD acts as an active external rotator only when the arm is abducted at 0°, the elbow flexed at 90° and the forearm in the sagittal plane, corresponding to the ER1 position [41]. Muscular activity has been recorded in several EMG studies following transfer procedures [1,9,11-18]. However, the results on active performance of transferred LD muscle are contradictory, and some of these studies have been focused on few cases and small sample sizes, so it was not possible to execute a statistical analysis. Weak activity in the transferred muscle was reported in some of these studies [11].

The differences found in the outcome of previous studies depend on different factors: preoperative muscle activity of LD, orientation of the transfer and the

effect of tendon insertion site during transfer. The posterosuperior area of the grater tuberosity at the level of insertion of the infraspinatus has been reported as the best attachment site for a transfer of LD based on the consequences for moment arms, muscle forces and lengths [40,42]. Bargoin et al. [43] demonstrated that the point of fixation of the LD on the humeral head had an influence on the elbow-to-body external rotation and with 90° abduction: the fixation point for a maximum external rotation with the elbow to the body was the anterolateral position, whereas the fixation point for a maximum external rotation at 90° abduction was the position centered on the infraspinatus footprint. The fixation point used in the current study was centered on the anterolateral position: this could explain the activity of the transferred LD noted only when the shoulder is abducted at 0° and the elbow flexed at 90°.

We acknowledge some methodological weaknesses in the present study. Similar to previous studies, we did not perform preoperative assessments [12,14,15], which make it difficult to understand how LD muscle activity changed over time relative to its initial condition. Moreover, although the contralateral shoulders were asymptomatic, these shoulders might have been affected by asymptomatic rotator cuff pathology [45]. We presume that satisfactory ROM after arthroscopic LDTT has to be mainly attributed to the activity of the transferred muscle, but the effect of LDTT on reducing pain has to be considered. Pain has an impact on scapular motion through different mechanisms, such as muscle activity or inhibition, decreases in proprioception and kinesthetic awareness and alterations in neuromuscular control [46]. In the current study, the value of the comparison between the patients and the healthy population can be limited by the age differences of the groups. Indeed,

age could be a confounder as the control group age range was 27 to 48 years compared to 47 to 71 years of age for the LDTT group. It has been reported that shoulder ROM decreases with age for active and passive forward elevation, extension, abduction, external rotation at 0° and 90° of abduction with the exception of internal rotation, which increases with age [47].

In summary, the use of EMG and magnetic and inertial motion analysis system allowed a simultaneous evaluation of muscular activation of the latissimus dorsi and scapula-humeral kinematics demonstrating that, after arthroscopic-assisted LDTT, the transferred muscle acts as a true external rotator when the shoulder is abducted at 0° and the elbow is flexed at 90°. Patients with irreparable MRCT have ROM comparable to their asymptomatic contralateral shoulders and to the shoulders of healthy individuals. Nevertheless, shoulder kinematics after LDTT perform differently than the nonsurgical side or than healthy individuals due to greater scapular contribution to overall humeral movement. These findings together support the hypothesis that both active muscle contraction and tenodesis effect contribute to shoulder ROM after LDTT with a variable prevalence of these mechanisms of action according to the different arm position. Further characterization of scapular biomechanics after LDTT could explain the differences in functional outcomes, identify better candidates for this surgical approach and improve the results to be expected after this procedure.

References

1. Gerber C, Vinh TS, Hertel R, Hess CW. 1988. Latissimus dorsi transfer for the treatment of massive tears of the rotator cuff. A preliminary report. Clin. Orthop. Relat. Res. (232):51–61.

2. Omid R, Lee B. 2013. Tendon transfers for irreparable rotator cuff tears. J Am Acad Orthop Surg 21(8):492–501.

3. Grimberg J, Kany J. 2014. Latissimus dorsi tendon transfer for irreparable postero-superior cuff tears: current concepts, indications, and recent advances. Curr Rev Musculoskelet Med 7(1):22–32.

4. Castricini R, De Benedetto M, Orlando N, et al. 2014. Irreparable rotator cuff tears: a novel classification system. Musculoskelet Surg 98 Suppl 1:49–53.

5. Warner JJ, Parsons IM. 2001. Latissimus dorsi tendon transfer: a comparative analysis of primary and salvage reconstruction of massive, irreparable rotator cuff tears. J Shoulder Elbow Surg 10(6):514–521.

6. Kurokawa D, Sano H, Nagamoto H, et al. 2014. Muscle activity pattern of the shoulder external rotators differs in adduction and abduction: an analysis using positron emission tomography. J Shoulder Elbow Surg 23(5):658–664.

7. Weening AA, Willems WJ. 2010. Latissimus dorsi transfer for treatment of irreparable rotator cuff tears. Int Orthop 34(8):1239–1244.

8. Gervasi E, Causero A, Parodi PC, et al. 2007. Arthroscopic latissimus dorsi transfer. Arthroscopy 23(11):1243.e1–4.

9. De Casas R, Lois M, Cidoncha M, Valadron M. 2014. Clinic and electromyographic results of latissimus dorsi transfer for irreparable posterosuperior rotator cuff tears. J Orthop Surg Res 9:83.

10. Oh JH, Park MS, Rhee SM. 2018. Treatment Strategy for Irreparable Rotator Cuff Tears. Clin Orthop Surg 10(2):119–134.

11. Ippolito G, Serrao M, Napoli F, et al. 2016. Three-dimensional analysis of the shoulder motion in patients with massive irreparable cuff tears after latissimus dorsi tendon transfer (LDT). Arch Orthop Trauma Surg 136(10):1363–1370.

12. Iannotti JP, Hennigan S, Herzog R, et al. 2006. Latissimus dorsi tendon transfer for irreparable posterosuperior rotator cuff tears. Factors affecting outcome. J Bone Joint Surg Am 88(2):342–348.

13. Aoki M, Okamura K, Fukushima S, et al. 1996. Transfer of latissimus dorsi for irreparable rotator-cuff tears. J Bone Joint Surg Br 78(5):761–766.

14. Irlenbusch U, Bernsdorf M, Born S, et al. 2008. Electromyographic analysis of muscle function after latissimus dorsi tendon transfer. J Shoulder Elbow Surg 17(3):492–499.

15. Habermeyer P, Magosch P, Rudolph T, et al. 2006. Transfer of the tendon of latissimus dorsi for the treatment of massive tears of the rotator cuff: a new single-incision technique. J Bone Joint Surg Br 88(2):208–212.

16. Plath JE, Seiberl W, Beitzel K, et al. 2014. Electromyographic activity after latissimus dorsi transfer: testing of coactivation as a simple tool to assess latissimus dorsi motor learning. J Shoulder Elbow Surg 23(8):1162–1170.

17. Gerhardt C, Lehmann L, Lichtenberg S, et al. 2010. Modified L'Episcopo tendon transfers for irreparable rotator cuff tears: 5-year follow-up. Clin. Orthop. Relat. Res. 468(6):1572–1577.

18. Henseler JF, Nagels J, Nelissen RGHH, de Groot JH. 2014. Does the latissimus dorsi tendon transfer for massive rotator cuff tears remain active postoperatively and restore active external rotation? J Shoulder Elbow Surg 23(4):553–560.

19. Brochard S, Lempereur M, Rémy-Néris O. 2011. Double calibration: an accurate, reliable and easy-to-use method for 3D scapular motion analysis. J Biomech 44(4):751–754.

20. Sabatini AM. 2011. Estimating three-dimensional orientation of human body parts by inertial/magnetic sensing. Sensors (Basel) 11(2):1489–1525.

21. Muraccini M, Mangia AL, Lannocca M, Cappello A. 2019. Magnetometer Calibration and Field Mapping through Thin Plate Splines. Sensors (Basel) 19(2).

22. Curtis AS, Burbank KM, Tierney JJ, et al. 2006. The insertional footprint of the rotator cuff: an anatomic study. Arthroscopy 22(6):609.e1.

23. Castricini R, De Benedetto M, Familiari F, et al. 2016. Functional status and failed rotator cuff repair predict outcomes after arthroscopic-assisted latissimus dorsi transfer for irreparable massive rotator cuff tears. J Shoulder Elbow Surg 25(4):658–665.

24. Cutti AG, Giovanardi A, Rocchi L, et al. 2008. Ambulatory measurement of shoulder and elbow kinematics through inertial and magnetic sensors. Med Biol Eng Comput 46(2):169–178.

25. Parel I, Cutti AG, Kraszewski A, et al. 2014. Intra-protocol repeatability and inter-protocol agreement for the analysis of scapulo-humeral coordination. Med Biol Eng Comput 52(3):271–282.

26. Cutti AG, Parel I, Raggi M, et al. 2014. Prediction bands and intervals for the scapulo-humeral coordination based on the Bootstrap and two Gaussian methods. J Biomech 47(5):1035–1044.

27. Parel I, Cutti AG, Fiumana G, et al. 2012. Ambulatory measurement of the scapulohumeral rhythm: intra- and inter-operator agreement of a protocol based on inertial and magnetic sensors. Gait Posture 35(4):636–640.

28. Ebaugh DD, McClure PW, Karduna AR. 2005. Three-dimensional scapulothoracic motion during active and passive arm elevation. Clin Biomech (Bristol, Avon) 20(7):700–709.

29. McClure PW, Michener LA, Sennett BJ, Karduna AR. 2001. Direct 3-dimensional measurement of scapular kinematics during dynamic movements in vivo. J Shoulder Elbow Surg 10(3):269–277.

30. Konrad P. 2006. A Practical Introduction to Kinesiological Electromyography, Version 1.4. Noraxon U.S.A Inc.:Scottsdale, Arizona; 61p.

31. Hermens HJ, Freriks B, Disselhorst-Klug C, Rau G. 2000. Development of recommendations for SEMG sensors and sensor placement procedures. J Electromyogr Kinesiol 10(5):361–374.

32. Drake JDM, Callaghan JP. 2006. Elimination of electrocardiogram contamination from electromyogram signals: An evaluation of currently used removal techniques. J Electromyogr Kinesiol 16(2):175–187.

33. Ludewig PM, Cook TM. 2000. Alterations in shoulder kinematics and associated muscle activity in people with symptoms of shoulder impingement. Phys Ther 80(3):276–291.

34. Mell AG, LaScalza S, Guffey P, et al. 2005. Effect of rotator cuff pathology on shoulder rhythm. J Shoulder Elbow Surg 14(1 Suppl S):58S-64S.

35. Vermeulen HM, Stokdijk M, Eilers PHC, et al. 2002. Measurement of three dimensional shoulder movement patterns with an electromagnetic tracking device in patients with a frozen shoulder. Ann. Rheum. Dis. 61(2):115–120.

36. Namdari S, Voleti P, Baldwin K, et al. 2012. Latissimus dorsi tendon transfer for irreparable rotator cuff tears: a systematic review. J Bone Joint Surg Am 94(10):891–898.

37. Henseler JF, Kolk A, Zondag B, et al. 2017. Three-dimensional shoulder motion after teres major or latissimus dorsi tendon transfer for posterosuperior rotator cuff tears. J Shoulder Elbow Surg 26(11):1955–1963.

38. Kolk A, de Witte PB, Henseler JF, et al. 2016. Three-dimensional shoulder kinematics normalize after rotator cuff repair. J Shoulder Elbow Surg 25(6):881–889.

39. Paletta GA, Warner JJ, Warren RF, et al. 1997. Shoulder kinematics with two-plane x-ray evaluation in patients with anterior instability or rotator cuff tearing. J Shoulder Elbow Surg 6(6):516–527.

40. Magermans DJ, Chadwick EKJ, Veeger HEJ, et al. 2004. Biomechanical analysis of tendon transfers for massive rotator cuff tears. Clin Biomech (Bristol, Avon) 19(4):350–357.

41. Tennent TD, Beach WR, Meyers JF. 2003. A review of the special tests associated with shoulder examination. Part II: laxity, instability, and superior labral anterior and posterior (SLAP) lesions. Am J Sports Med 31(2):301–307.

42. Ling HY, Angeles JG, Horodyski MB. 2009. Biomechanics of latissimus dorsi transfer for irreparable posterosuperior rotator cuff tears. Clin Biomech (Bristol, Avon) 24(3):261–266.

43. Bargoin K, Boissard M, Kany J, Grimberg J. 2016. Influence of fixation point of latissimus dorsi tendon transfer for irreparable rotator cuff tear on glenohumeral external rotation: A cadaver study. Orthop Traumatol Surg Res 102(8):971–975.

44. Gerber C, Maquieira G, Espinosa N. 2006. Latissimus dorsi transfer for the treatment of irreparable rotator cuff tears. J Bone Joint Surg Am 88(1):113–120.

45. Yamaguchi K, Tetro AM, Blam O, et al. 2001. Natural history of asymptomatic rotator cuff tears: a longitudinal analysis of asymptomatic tears detected sonographically. J Shoulder Elbow Surg 10(3):199–203.

46. Scibek JS, Mell AG, Downie BK, et al. 2008. Shoulder kinematics in patients with full-thickness rotator cuff tears after a subacromial injection. J Shoulder Elbow Surg 17(1):172–181.

47. Barnes CJ, Van Steyn SJ, Fischer RA J. The effects of age, sex, and shoulder dominance on range of motion of the shoulder. Shoulder Elbow Surg. 2001 May-Jun;10(3):242-6

Conclusion:

NCS Lab and the University of Bologna started three years ago an important research project aimed to develop a wireless biomechanical platform for analysing both kinematics and electromyography of the human body. Thanks to this strong collaboration, and with the aim of providing both to the clinicians and the patients a simple but accurate tool for the objective tracking of the patients during the phases of their rehabilitation process, this PhD was born.

The first two years of the PhD were fully dedicated to the hardware and software development of a platform for human biomechanical analysis using wireless magnetic and inertial measurement units. Novel sensor-fusion and calibration algorithms were developed and implemented on board, allowing a real time data acquisition of the kinematics of the whole body. The work done in the first two years resulted in two papers, reported in this thesis in chapter 2 and 3. In both, innovative algorithms were proposed and tested, showing excellent results, as reported in the respective sections. After that, given that the technology developed seemed to offer good results, in the last year my research activities were focused on its clinical validation.

The first clinical study aimed to evaluate the intra and interobserver reproducibility for evaluating three-dimensional humero-scapulo-thoracic kinematics in an outpatient setting. Twenty-five subjects were analysed bilaterally four times by two different operators while performing flexion-extension and abduction-adduction movements. The graphs related to the scapula-humeral rhythm were calculated for each analysis performed by the subjects and the similarity of the related curves was assessed through Root

Mean Square Error and Coefficient of Multiple Correlation. The results were comparable to that obtained with other validated methods, proving the robustness of the technology developed.

A second study aimed to evaluate the effect of Latissimus Dorsi Tendon Transfer on shoulder kinematics and Latissimus Dorsi activation in humerus intra - extra rotations. The results of the analysis on 25 patients (one year after the surgery) showed a complete Range of Motion in humerus elevation, but a larger scapula compensation in the latissimus dorsi transferred side, compared with the healthy side. Moreover, the results showed that the patients have difficult in learning how to properly activate the LD after the transfer.

Both the clinical studies presented have demonstrated the ability of the developed platform to enter into daily clinical practice, providing useful information for patients' rehabilitation.

The two clinical studies reported represents only the starting point: the interest in the technology developed has been extended to many important clinics around the world. Loyola University (Chicago), UCONN (Hartford), University of Colorado (Denver), Charitè (Berlin), Ospedale di Baggiovara (Modena), COT clinic (Messina) and ICOT clinics (Latina) are some of the end users of the product. Finally, Dr. Kibler, considered as the most expert in shoulder kinematics in the world, was fascinated by the technology; he and his team are using the developed platform to objectify what they have so far only been able to see by their eyes. Such important collaborations can only make us proud of what has been done.

Looking to the future, the developed technology could be surely improved. Future research will be focused on different aspects, both clinical and methodological. Many attentions will be focused on a possible novel implementation of the sensor-fusion algorithm for the improvement of the accuracy provided by the sensors. At the same time will be fundamental to develop and to include in the platform advanced algorithm for soft tissue artefact compensation. Finally, an extension of the clinical studies to other joints will be the natural continuum of the work done on the shoulder.

Acknowledgments

First, I would like to thank my supervisor Prof. Angelo Cappello for the support he gave me during this journey, but, most importantly, for the trust he showed by choosing me for this project. It is thanks to him that I have begun, and now completed, this exciting journey. The skills and wisdom that he has passed on to me are priceless gifts.

I also want to express my gratitude to all the NCS team, obviously starting from Matteo Mantovani and Alessandro Varini; they allowed me to work into a cutting-edge research project. Most importantly, they gave me the opportunity to try, to make mistakes, to understand where the error was, and to learn from the mistake to improve myself, as it is rare to see in companies.

I would not be here without Matteo Mantovani open-mindedness about new ideas and enthusiasm about innovative projects. In general, working at NCS has been a joy, thanks also to all my colleagues.

Staying alive while pursuing your dreams is also important. In this my family, my friends and Paola have played a fundamental role and I want to thank them.

The greatest thank go to me for having fought to reach this amazing goal. I'm proud of that.